THE UNIVERSITY OF MICHIGAN
COLLEGE OF ENGINEERING
High Altitude Engineering Laboratory
Departments of
Aerospace Engineering
Meteorology and Oceanography

Technical Report

THE DISTRIBUTION OF TROPOSPHERIC INFRARED RADIATIVE FLUXES AND ASSOCIATED HEATING AND COOLING RATES IN THE SOUTHERN HEMISPHERE

ORA Project 031640

under contract with:
NATIONAL SCIENCE FOUNDATION
GRANT NO. GA-10884
WASHINGTON, D. C.

administered through
OFFICE OF RESEARCH ADMINISTRATION ANN ARBOR

March 1972

ACKNOWLEDGEMENTS

To the evening operators at the computing center, to WABX, to Ginny, Jeanne, and Judy, to the thesis itself for keeping me company, to Bill and a few others for happening along and helping, to the other people such as Karen, whom I like, and finally to myself.

To the members of my committee and my Department, to Mrs. Deakin, to the National Science Foundation who sponsored this research, and to the National Center for Atmospheric Research, at whose facilities much of the computing was carried out, and from whom much of the data used in this study was received.

TABLE OF CONTENTS

TABLE OF CONTENTS (continued)

TABLE OF CONTENTS (continued)

LIST OF TABLES

LIST OF TABLES (continued)

LIST OF TABLES (continued)

LIST OF FIGURES

LIST OF FIGURES (continued)

LIST OF FIGURES (continued)

LIST OF FIGURES (continued)

ABSTRACT

Little consideration has been given to the radiative budget of the Southern Hemisphere. Yet such information is needed if the general circulation and energy budget of the hemisphere is to be understood. This study presents the results of infrared flux calculations carried out for the hemisphere for climatological conditions for January and July. The results are given in terms of the resultant heating and cooling rates, the fluxes at the top of the atmosphere, and the net flux divergences for the entire atmospheric column. The 6.3 and 80 micron water vapor, the 15 micron carbon dioxide, and the 9.6 micron ozone bands are considered and transmission functions determined from the quasi-random band model, with the exception of the ozone band, for which Walshaw's empirical formula is used. The calculated transmissivities are compared to experimental values and fall within their experimental uncertainties.

Clouds represent one of the most critical and poorly dealt with factors in the radiative transfer problem. A survey of the cloud cover data is summarized. Individual cloud covers are corrected for overlap following Telegadas and London's technique. In the flux calculation, overlapping is dealt with by assuming the clouds are randomly distributed.

The annual mean zonally averaged outgoing flux at the top of the atmosphere as determined from this study is slightly smaller (less than 7%) than the satellite observations of Vonder Haar and Suomi (1971) and the calculations of Sasamori et al. (1971) to latitudes of 65^{o}S. Near the pole, the present calculations give results larger than either of these two studies, there being as much as a 10% difference with Sasamori et al's values and 26% with Vonder Haar and Suomi's results. The shapes

and seasonal distributions are quite similar showing an overall decrease from equator to pole with greater values in July from the equator to subtropics and greater values in January further toward the pole.

When the fluxes calculated in this study are introduced into the meridional heat transport calculations of Vonder Haar and Suomi and Sasamori et al they suggest at best only a slight increase in their values.

Mean annual zonal values of the net flux divergence are compared with the values of Sasamori et al. and found to be within 14%. The present smaller values are the result of the larger cirrus covers. Our values are also smaller than those of London (1957) for the Northern Hemisphere but this is to be expected given the smaller cloud amounts and greater water vapor amounts in that hemisphere. When the seasonal distributions from this study are examined they reverse themselves with respect to each other three times from equator to pole. This is due to the varying importance of cirrus cover and water vapor amounts.

Zonally averaged meridional cooling rate cross sections are nearly identical to the cross sections calculated from zonally averaged atmospheric parameters. The cross sections show a zone of warming extending from equator to pole just below the cirrus deck. Maximum warming ($2.8^{o}C\ day^{-1}$) is located over the polar front. Cooling is found above the cirrus clouds and in the layers from beneath the region of warming to the surface. Maximum values ($4^{o}C\ day^{-1}$) are found over the tropics and polar front, the polar maximum being at lower levels.

Near the surface below the lowest clouds the cooling rates do not exceed $1^{o}C\ day^{-1}$.

Meridional cooling rate cross sections are presented for longitudes representing both maritime and continental situations. While their general appearances are like those of the zonally averaged cross sections, rates are seen to double from one longitude to another. In all these cross sections the rates are highly dependent on the heights and amounts of the cloud types.

CHAPTER I

INTRODUCTION

Various studies dealing either totally or in part with the infrared portion of the radiation budget have been carried out for the troposphere. London (1957) has calculated the cooling rates and boundary fluxes and Davis (1961, 1963) just the cooling rates for each season using zonally averaged atmospheric parameters for the northern hemisphere. Sasamori et al. (1971) made calculations for the southern hemisphere giving their results in terms of the fluxes at the top and bottom of the atmosphere and the net cooling rates for the entire atmospheric column. Dopplick (1970) determined cooling rates for both hemispheres using zonally averaged parameters. The only study of either hemisphere which considers longitudinal variations in the infrared cooling rates and fluxes has been done by Katayama (1966, 1967a, 1967b) for the northern hemisphere.

London's results for the upward infrared flux at the tropopause for conditions of average cloudiness show a maximum at 15^{o}N (~525 ly day^{-1}) in the winter and at 25^{o}N (~510 ly day^{-1}) in the summer. Poleward of 20^{o}N the summer values are greater than those in the winter while the opposite is true within 20^{o} of the equator. Minimum values are found in the arctic for both seasons with the lowest value (~280 ly day^{-1}) occurring in the winter. At the surface the maximum net (upward[1]) infrared flux, referred to by London as the nocturnal radiation, is found at 15^{o}N (~165 ly day^{-1}) in the winter and at 35^{o}N (~155 ly day^{-1}) in the summer. The minimum value of 85 ly day^{-1} remains unchanged from summer to winter but shifts its location from 75 to 65^{o}S. The mean meridional

[1] "upward" indicates that the direction of the net radiation is upward.

infrared cooling rate cross sections with clouds present are similar for all seasons, having values of 0.4 to 0.8°C per day near the surface. A maximum of about 2.5°C per day is reached in the mid-troposphere just above the middle cloud layer. At the tropopause the values have again dropped to about 0.4°C per day. The height of maximum cooling increases slightly from the equator to about 20°N and decreases thereafter to the pole except in the winter when it is highest over the equator. The average annual infrared cooling over the column from surface to tropopause with clouds present varies from 1.6°C per day south of about 25°N to about 1°C per day at the pole.

Davis's cooling rate calculations cover the region from 20 to 70°N and are, for the most part, qualitatively similar to London's although Davis's maximum cooling rates are about 0.5 to 1.0°C per day lower. Near the surface between 60 and 70°N, both show a rate of about 0.4°C per day. However, while London's surface values remain constant as latitude decreases, Davis's cooling rates increase to 1.5°C per day at 20°N. Davis found that his results, averaged over all latitudes and seasons, are 13 percent lower than those of London.

The upward infrared flux at the top of the atmosphere in the southern hemisphere as calculated by Sasamori et al. (1971) shows maxima at approximately 25°S (518 ly day^{-1}) in the summer (January) and at 15°S (525 ly day^{-1}) in the winter (July). Poleward of 20°S, largest values occur in the summer, while equatorward of 20°S they are found in the winter. Minimum values are found near the pole for both seasons (300 ly day^{-1}) and are lower in the winter. The maximum net (upward)

infrared flux at the surface occurs in January at 25°S (131 ly day^{-1}) and in July at 15°S (136 ly day^{-1}). The seasonal minima both occur at 65°S (77 ly day^{-1} in January and 71 ly day^{-1} in July).

If Sasamori et al.'s results for the southern hemisphere are compared with London's for the Northern Hemisphere the agreement is qualitatively quite good. Quantitatively however Sasamori et al.'s net surface fluxes are 10 to 15 percent lower than London's. This is because of the greater cloud cover in the southern hemisphere. If Sasamori et al.'s upward fluxes at the top of the atmosphere are compared with London's values (adjusted to include a stratospheric water vapor contribution) they are approximately the same.

Dopplick's northern hemisphere cooling rates show similar patterns to those of London and Davis. He finds the horizontal gradient near the surface which appeared in Davis's results although Dopplick's rates are from 0.5 to 1.0°C per day greater. The maximum values aloft near the equator are mid-way between Davis's and London's and much closer to Davis's lower values toward the pole. These comments are appropriate regardless of which seasons are compared. Dopplick's cooling rates for both hemispheres show considerable symmetry, especially between 40°N and 40°S; the axis of symmetry extends from 10°N at the surface to 10°S at 400 mb. These results are true regardless of season. Poleward of 40°N and 40°S, the cooling rate patterns are still qualitatively similar, but the southern hemisphere cooling rates are as much as 0.5°C per day smaller. Dopplick's cross sections are shown in Figure IV-13.

From his hemispheric values Katayama has calculated zonal averages

of the net infrared fluxes at the surface and 200 mb for January and July for the northern hemisphere. The net flux at 200 mb is maximum at 10^{o}N (508 ly day^{-1}) in January and at 30^{o}N (485 ly day^{-1}) in July. The values for January are larger than those for July south of 25^{o}N while the July values are larger north of that latitude. Minimum values (284 ly day^{-1} in January and 344 ly day^{-1} in July) are found near the pole. At the surface the maximum net (upward) infrared flux occurs near 20^{o}N (164 ly day^{-1}) in January and 30^{o}N (152 ly day^{-1}) in July. The minimum values are at 70^{o}N (78 ly day^{-1}) in January and 80^{o}N (73 ly day^{-1}) in July (no values are given for the pole itself). These results agree qualitatively with those of London and Sasamori et al. Quantitatively Katayama's results are not in any better agreement with London's Northern Hemisphere values than are Sasamori et al.'s Southern Hemisphere values.

Katayama's hemispheric distributions of the net (upward) infrared flux at the surface yield maxima situated between 15 and 20^{o}N in January and 20 and 30^{o}N in July, the shift following the motion of the subtropical high. The arid area of northern Africa appears as a region of relatively high values while the monsoon areas of India and the north-western north Pacific have relatively low values. These results are correlated with the amount of water vapor and cloud cover present. Transitions from land to water are also evident. In January at the surface in mid and high latitudes the net flux increases from land to water while the reverse is true in July. In January the smaller cloud cover and lower surface temperatures over land oppose each other with the temperature effect predominating. In July the smaller cover and higher temperatures over land complement each other.

Katayama's hemispheric distribution of net infrared flux at 200 mb for January follows his 500 mb temperature distribution rather well. Minimum net fluxes are found over Siberia and arctic Canada with values increasing in a concentric symmetry around the pole thereafter to about 10^{o}N. This latitude of low cloud cover and high temperatures produces the largest net fluxes. In July the meridional variation of temperature is not as great as in January and variations in cloud cover are more influential. The largest and smallest net fluxes at 200 mb are found at latitude 25^{o}N. The largest values of 0.42 calories $cm^{-2}min^{-1}$ are associated with the low cloud cover over the region from North Africa to Afganistan and the smallest values of 0.24 calories cm^{-2} min^{-1} with the large cloud covers over India and also the Arctic. Since North Africa and India lie at approximately the same latitude, the zonal gradient is very strong there.

Katayama also presents hemispheric distributions of the average cooling over the atmospheric column extending from the surface to the tropopause. The figure for January is quite similar to that for the 500 mb temperature distribution and thus the qualitative comments made about the 200 mb net flux distribution for January are also appropriate here. In July large cooling rates are found along the subtropical highs while minimum cooling rates are located over regions of low surface pressure such as Greenland and the Rocky Mountains.

Zonal cross sections of the cooling rates for January and July at 20, 40, and 60^{o} N are also included. In the vertical there are three layers of local maximum cooling resulting from the vertical distribution of cloud cover into three layers. The highest layer is associated with the cirrus deck which is treated as only partially black and thus sometimes is not very noticeable. Over water the maximum cooling is found in the mid-troposphere

while over land it is found close to the surface. The longitudinal variations in cooling rates are most evident near the surface. This layer of cooling near the surface over land can in fact be divided into two categories. In regions of low cloud cover with arid climates the level of maximum cooling will be quite close to the ground. In regions where the low clouds are relatively dense and the middle clouds relatively light the low level maximum rates are found about 100 mb above the surface. The seasonal variations for these zonal cross sections in general parallel those found by the other studies.

Such infra-red studies are of considerable relevance to investigators of the general circulation and the earth's heat budget. However, except for Katayama's study of the northern hemisphere, there remains the question as to how useful they can be in that they fail to consider longitudinal variations of the radiation budget. The longitudinal variations of the atmospheric parameters used in the flux and cooling rate calculations may be substantial and in such cases much information will be lost if only zonal means of these parameters are used. In particular, changes across land water interfaces will be smoothed out. Also since the solution of the transfer equation is nonlinear in temperature, pressure and relative humidity, the flux divergence as computed for a set of longitudinally averaged climatological parameters will not necessarily equal the longitudinal mean of the flux divergences. Rodgers and Walshaw (1966) have considered this problem as it relates to the errors introduced when climatologically averaged values for the temperature and absorber concentrations are used. They conclude that the error introduced as far as temperature is concerned is minor and although the error related to the water vapor mixing ratio is

larger than that for temperature, it is still unimportant. Their conclusions are however limited in that they are based on an examination of only one case.

In this study climatologically but not zonally averaged atmospheric parameters are used. With the availability of high speed computers and increasing amounts of data such a study is now feasible. Fluxes and cooling rates are calculated for January and July at selected geographical grid points and a vertical resolution of approximately 65 mb. These values are then zonally averaged and compared to the fluxes and cooling rates gotten from zonally averaged values of the climatological atmospheric parameters.

One of the major difficulties in tropospheric radiation studies is the incorporation of clouds in the atmospheric model. An atmosphere which contains more than one cloud layer presents two distinct problems to the radiative calculations. First the presence of lower clouds makes it impossible for the observer at the surface to determine with complete confidence the extent of the cloud cover aloft. An approach developed by Telegadas and London (1954)- and discussed in the next chapter-has been used by London, Davis, and Sasamori et al. to correct this underestimation of the upper and mid level cloud amounts. Sasamori et al. also reduced the amount of each cloud type by forcing the sum of the individual cloud amounts to equal the total cloud cover, thereby implicitly assuming that there is no overlap. Katayama also states that because of a "lack of information," overlapping is assumed not to occur.

The second problem relates to the calculation of the fluxes. If

the flux is needed at some level and more than one cloud layer lies below that level then the expression for the upward flux will be somewhat complex. In addition to the contributions to the flux from the ground and cloudless parts of the sky each cloud layer also will contribute (assuming the upper one does not completely obscure the lower one). The extent of each of these contributions will depend, among other things, on the amount of each of the two cloud layers, the ground, and the clear sky which are visible looking downward from the level at which the flux is to be calculated. In order to determine these amounts it is necessary to know how much the clouds overlap.

London simplified the cloud problem by assuming that no overlapping of clouds occurs. The cooling rates were calculated for clear skies and for each cloud type occurring alone under conditions of complete overcast. These rates were then combined by weighting them according to the percent of sky covered by each cloud. Davis, in a somewhat similar approach, divided the clouds into six types and only permitted the overlapping of cirrus, altostratus, or nimbostratus. This limits the number of possible sky conditions to nine. The cooling rates for each of the sky conditions were calculated and weighted according to their frequency of occurrence. Unfortunately, it is not clear what assumptions Davis made to arrive at frequencies of occurrence for the two sky conditions in which overlapping was permitted. Katayama, and Sasamori et al. approched the problem in essentially the same way as London did, except the fluxes for clear and cloudy skies were weighted rather than the cooling rates and the final cooling rates were then calculated from the mean fluxes.

It is not obvious how Dopplick treated the overlapping of clouds,

regarding not only the correction for the observed amounts, but also the method used for the flux and cooling rate calculations.

In order to estimate the error which results from this non-overlapping assumption, Katayama calculated the cooling rates for two situations, both possessing two cloud layers and the same total cloud cover. In one, the clouds were treated as overlapping entirely and in the other as not overlapping at all. For the case he examined he found for overlap the cooling rate of the whole tropospheric column and the outgoing long wave radiation at the top of the atmosphere decreases by 10 to 20 percent compared to the case in which no overlap occurs.

In carrying out the calculations particular concern is paid to developing as realistic a picture of the cloud cover as is possible. A survey of the available data is presented. Such a survey has not been made before for the southern hemisphere and should be of use to those conducting climatological studies. Also since the radiation calculations are extremely dependent on cloud cover, such a study is crucial to the success of the calculations.

In this study a multilevel cloud model (five cloud types with variable thicknesses and heights) is used which takes into account overlapping. The flux divergence for a given level is calculated as the weighted mean of the fluxes for the various possible sky conditions. The model is discussed in Chapter III. In addition, fluxes and cooling rates are calculated for clear skies, which facilitates isolating the influence of the clouds from those of the temperature and absorber concentrations.

Various band parameters and absorption models have been employed in the above mentioned studies. London used the radiation chart, developed

by Elsasser (1960) and based on the periodic band model, to determine the radiative fluxes. Davis utilized both laboratory and published theoretical values for the transmission functions. Sasamori, et al. based their calculations on the approach developed for Yamamoto's radiation chart but replaced the table with empirical formulas. Katayama, in his hemispheric calculations for the northern hemisphere, took the same approach as that used by Yamamoto in the construction of his radiative flux chart except that the solutions were carried out numerically. It might be noted that Goody (1964) has compared cooling rates arrived at using Elsasser's and Yamamoto's approaches and found a minimum difference in the cooling rates of $0.5^{o}C$ per day which is substantial since the rates themselves rarely exceed $4.0^{o}C$ per day.

Goody's random band model was adopted by Dopplick for the calculation of the water vapor transmissions. An empirical fit to the measured equivalent width of the whole 15 micron band developed by Rodgers and Walshaw was used for the carbon dioxide calculation and the random band model of Malkmus (1967) fitted by Rodgers (1968) to Walshaw's (1957) laboratory measurements was employed for the ozone calculation.

Recent advances in molecular physics have provided additional information about the molecular parameters for the gases which are of importance to radiation studies in the earth's troposphere. This permits the transmissivities to be calculated rather than empirically determined as previous studies have had to do. Rodgers and Walshaw (1966) have concluded that the empirical transmissivities appear to be valid for the lower and mid troposphere. However for the upper troposphere the mass paths are small and an extrapolation of the empirical formulae to these low

pressures and mass paths is sometimes invalid. In the present calculations, the quasi random band model is used. The primary bands are the 6.3 and 80 micron water vapor bands, the 15 micron carbon dioxide band, and the 9.6 micron ozone band, although all the water vapor lines up to 2450 cm^{-1} are included.

This study has two primary objectives: to improve on previous models both by utilizing better and more extensive climatological data, and by using improved transmissivities; and to provide a physically more realistic and useful model of the infrared portion of the heat budget for the Southern Hemisphere by including zonal as well as meridional variations. Climatological data from the Global Atmospheric Research Program can, when it becomes available, be used to supplement the present data coverage along with the developing body of satellite data. The calculations should prove useful for a global energy balance study as well as providing a model for use in general circulation studies for which approximations to the infrared radiative heating and cooling can be compared.

CHAPTER II

THE ATMOSPHERIC MODEL (Data Sources and Treatment)

II-1 TEMPERATURE AND PRESSURE

Taljaard, Van Loon, Crutcher and Jenne (1969) have prepared an atlas (Climate of the Upper Air, Part I -- Southern Hemisphere, 1969) covering selected climatic elements for the Southern Hemisphere. Their temperatures and pressures are given at the surface and tropopause and where possible temperatures at 850, 700, 500, 300, 200 and 100 mb for January and July over a square grid of 5^{o}.

Temperatures are needed at levels other than those given in the atlas and it is therefore necessary to fit the observed temperatures to some function of pressure. Problems arise however when the atmospheric column, which in effect extends to the 137. 5 mb level, reaches above the tropopause, the increased curvature of the temperature profile making it difficult to achieve a representative fit with a low order polynomial. In these cases if the observed profile is accurately fitted above the tropopause, unrealistic temperatures result near the surface. The orders of the polynomial were finally chosen so as to minimize the error below the tropopause and thereby insure that the cirrus cloud temperatues, on which the flux calculations aloft are highly dependent, are given as accurately as possible. Above the cirrus layer the temperature is not as critical to the flux calculations. Least squares polynomials of the fourth order were used when seven or eight observed points were available and of the third order when six observed

points were available. Below the tropopause the resulting errors are generally less than 1^{o} C. Fig. (II-1) is representative of the observed profiles and their least-squares fits. Zonally averaged temperature and pressure data are given in appendix A.

II-2 ATMOSPHERIC COMPOSITION

II-2.1 Water Vapor

The atlas of Taljaard et al(1969) also provides dew point temperatures at the surface, 850, 700 and 500 mb. In our calculations water vapor is in units of gm/cm^2. To convert the dew point data into these units a relationship developed by Tetens (1930) is used,

$$e = 6.11 \times 10^{7.5\, T_d/(237.3 + T_d)} \qquad \text{(II-1)}$$

where e is the vapor pressure in mb and T_d the dew point temperature in ^{o}C. The expression for the water vapor mass path, UM, over a vertical path Δp mb is,

$$UM = (\bar{q}/g)\Delta p \qquad \text{(II-2)}$$

where $\bar{q}$ is the mean specific humidity equal to $.622\bar{e}/\bar{p}$, $\bar{e}$ is the mean vapor pressure in mb, $\bar{p}$ the mean pressure in mb over the path, and $g = 980$ cm/sec^2.

Water vapor measurements above the 500 mb level are not abundant. Mastenbrook (1967) reports on a series of stratospheric and high tropospheric soundings made with balloon-borne frost point hygrometers taken mainly over Trinidad, West Indies and Washington, D. C. These observations agree well with those taken by Williamson and Houghton (1965) over England and also are consistent with the values calculated by Calfee and Gates (1966) from aircraft spectrographic

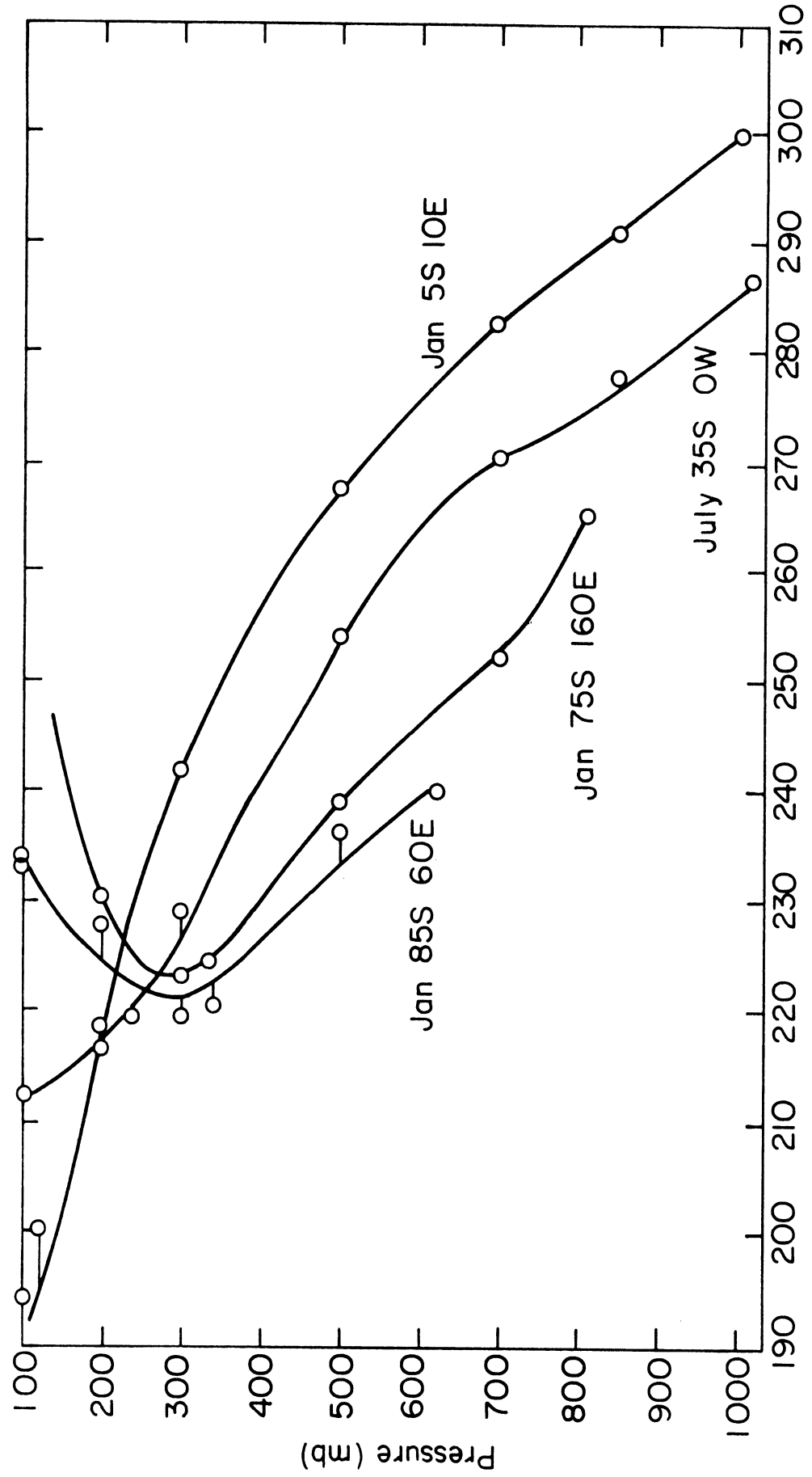

Figure II-1 Comparisons of temperature data to polynomial approximations

measurements over Florida. No systematic latitudinal variation can be seen in the frost point observations and it was decided therefore to use a single value for each season to represent the frost point at 100 mb. From the work of Mastenbrook (1967) we have chosen values of -83°C (January) and -80°C (July).

Depending on the value of the surface pressure there are five, four, or three dew point (frost point) temperatures available per surface grid point. A least squares fit was applied to provide the required water vapor concentrations, a third order polynomial being used when five values were available and a quadratic otherwise. The fits which resulted are quite good. This is to be expected since the observed data, to the extent that it is available, indicates that the observed dew point profiles are rather smooth. Fig. (II-2) shows typical observed profiles and fits. Zonally averaged values of water vapor content are given in appendix A.

II-2. 2 Carbon Dioxide

Observations indicate that carbon dioxide is quite well mixed throughout the troposphere. A value of 4.56×10^{-4} gm/gm has been used for the mass mixing ratio.

II-2. 3 Ozone

Very little ozone data are available for the southern hemisphere. Dopplick (1970) has taken observations from the North America Ozone Network and seasonally transposed them to provide zonally averaged vertical ozone profiles for the southern hemisphere. He notes however, that there is considerable asymmetry in the global distribution of total

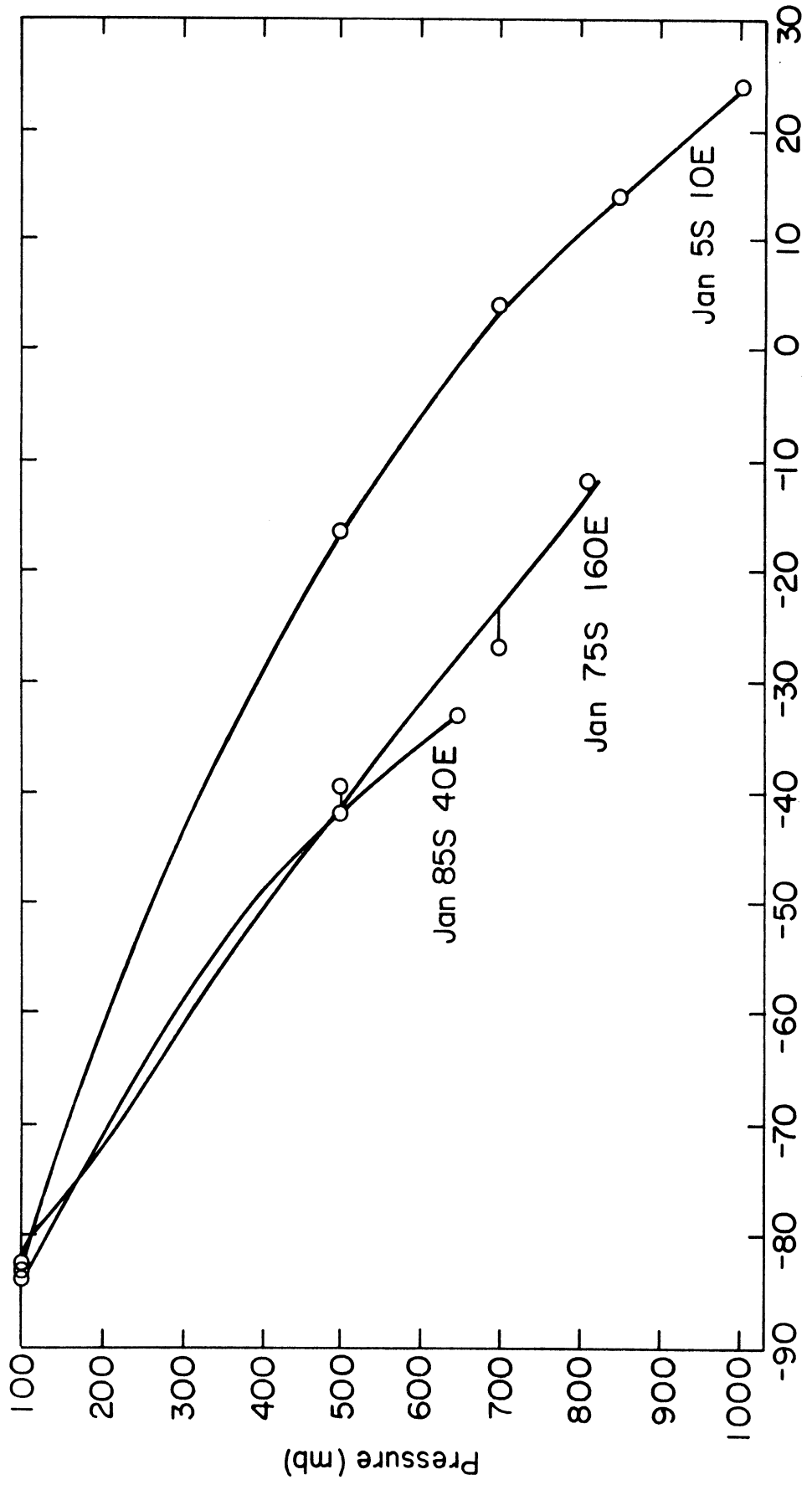

Figure II-2 Comparisons of dew point data to polynomial approximations

ozone between the hemispheres for the same season and therefore introduces a correction for this by adjusting the vertical ozone profiles by a multiplicative factor equal to the ratio of the total ozone amounts for equivalent latitudes of the reflected months.

II-3 CLOUDS

II-3.1 Introduction

The accuracy with which the infrared heating and cooling rates can be determined is, in part, dependent on how accurately the cloudiness of the atmosphere can be represented. This involves the total cloud cover and cloud cover by type, the height and thickness of each cloud type, and the radiating temperatures of the cloud surfaces. In addition the problems of dealing with a multilevel cloud structure and whether the radiating surfaces of the various cloud types can be treated as black bodies must be considered.

II-3.2 Total Cloud Cover

The discussion that follows is summarized in tabular form in Table (II-1) at the end of this section. Unless otherwise indicated the studies are climatological.

The earliest extensive summary of total cloud cover was prepared by C. E. P. Brooks (1927). His results are given as a function of latitude from pole to pole separately for ocean and land surfaces and also as a mean value for each latitude belt. Shaw (1936) developed a set of maps of both hemispheres for the means for each month and also for the year. These are based on work done by Brooks in 1919 and revised in 1921. The only other major study in the first half of the twentieth century was carried out by McDonald (1938). Those results,

based on observations made around 1200 GMT, are presented as seasonally averaged maps over all the oceans of the world, except near the poles. These values have been used in this study.

Haurwitz and Austin (1944) give global maps for January and July excluding the polar regions. In the Handbook of Meteorology Landsberg (1945) presents the mean cloudiness for the world for every second month beginning with January. All the above mentioned sources provide their information in fractional tenths or tenths of percent of cloud cover.

The United States Navy has prepared a series of Marine Climatic Atlases for the oceans of the world. In conjunction with the United States Weather Bureau they have also compiled a second series of oceanic atlases. Unfortunately the data are in such a form (isolines of the percentage frequency of occurrence of total cover greater than or equal to six tenths and less than or equal to two tenths with the cutoff values changing from atlas to atlas) that they are not of use to this study.

Telegadas and London (1954) have examined the total cloud cover for the northern hemisphere for the summer and winter. Seide (1954), in a related study, has provided the same values for the spring and fall. Their values are presented in tenths and percents respectively.

With the development of satellite technology in the 1960's there has been a considerable increase in the amount of cloud data available. In addition to providing meteorology with a new tool with which to observe the clouds it has also restimulated an interest in the large number of surface observations made in the past. This has resulted from a

need to have another source of cloud data to which the satellite observations could be compared.

Satellites have provided a convenient means of observing large areas of the earth. Although the full capabilities of this observational technique have not been realized a considerable body of data has been collected for total cloud cover. Allison et al. (1969), using TIROS VII data for the period from 19 June 1963 to 31 December 1964, have prepared quasi-global maps of monthly mean equivalent blackbody temperatures in the 8 to 12 micron window and compared the cloud cover suggested by these observations to that from surface observations. These surface observations have been collected and prepared for the northern hemisphere between 10^{o} and 70^{o} and mean monthly maps for the period from June 1963 to December 1964 are available.

In a related study Godshall et al. (1969) have compiled a tropical cloudiness atlas using daily TIROS and ESSA television nephanalysis. Monthly averages for January, April, August and October for each year from August 1962 to August 1968 are given from 100^{o}W to 130^{o}E and 30^{o}N to 25^{o}S. Since these are television observations, they only represent daytime cloud cover. There is a considerable variability from year to year in these results and therefore a noticeable difference between these observations and those of such climatological atlases as those of the United States Navy. Godshall (1968) has also prepared mean cloud cover maps based upon TIROS data for approximately the same area for January and August. These averages are based on the data from 1963 to 1965.

Allison and Warnecke (1967) have examined TIROS VII television

observations for January 1964 and analyzed the mean daytime cover for the eastern Pacific Ocean (25°N-20°S, 85°W-160°W). Using TIROS nephanalysis Clapp (1964) has produced average daytime cloud cover maps for March 1962 through February 1963, each map representing three months of observations. The area between 60°N and 60°S is covered. He only uses three cloud coverage catagories, 100 to 75%, 75% to 50%, and less than 50%. He (1968) has also prepared daytime maps for the Northern Hemisphere for the late fall for 1962, 1963, and 1964 as well as for the three year average.

Sadler (1968), as part of the International Indian Ocean Expedition, has assembled cloud cover data for each month from February 1965 to January 1967 based on satellite observations. The area covered lies between 30°N and 30°S. Also given are monthly averages for the two years combined. He (1969) has prepared but not published maps for the period from February 1967 to January 1968. More recent data are presently being compiled. Also, under the auspices of the International Indian Ocean Expedition TIROS observations over the Indian Ocean have been analyzed and mean monthly maps drawn for both 1963 and 1964 by Ramage et al. (1969).

Glaser et al. (1968) have collected satellite observations for part of the region 130°W-100°E, 37°N-37°S for May 15 - August 31, 1966 and 9 October 1966- 28 February 1967. Their results, although not extensive, are interesting because they pay particular attention to coast lines where substantial changes in cloud cover should be anticipated.

A study by Sherr et al. (1968) has divided the globe into

twenty nine quasi-homogeneous cloud climatic regions. Five cloud cover catagories are used and amounts are given in terms of the probabilities (equivalent to the frequency of occurrence) of occurrence of each of these classes. Averages are calculated for each month at eight equally spaced hours of the day. Both surface and satellite observations are used. Depending on the degree to which the twenty nine areas accurately represent areas of homogeneous cloud cover this study could substantially reduce the number of data points required for the transfer calculations, at least as far as cloud cover is concerned. However with respect to the homogeniety of the areas selected this represents an initial study and there still is some question as to the correctness of the choices made.

The Environmental Technical Applications Center of the United States Air Force has prepared a cloud cover summary for the Northern Hemisphere. The data covers the period from September 1963 to August 1968. Mean cloud amounts for each month are given in eighths for 0000 and 1200 GMT. Maps developed from this data for fifteen day periods from 16 May 1966 to 31 July 1966 are presented by Raschke (1968).

As yet unavailable but anticipated soon is a seasonal global cloud cover atlas covering the period from July 1962 to December 1964. This is being prepared by Arking of NASA.

Quite a few local cloud cover studies are also available. Sellers (1958) has prepared monthly means for the period from 1949 to 1958 for various hours of the day for six cities in Arizona. de Bary and Moller (1963) have calculated summer and winter morning and

afternoon means for the period from 1936 to 1940 for different atmospheric layers over Germany. Elliott (1960) has presented mean monthly maps and Schloss (1962) me an seasonal maps for summer and winter for the U. S. S. R. Elliott has also calculated averaged monthly cloud covers for a series of individual U. S. S. R. stations.

The United States Air Force has compiled cloud cover data for various stations. These can be found in the Air Force Summaries of Surface Weather Observation (A-B Summaries), the Revised Uniform Summary of Surface Weather Observations, and the Air Weather Service N Summary #17. The manner of reporting cloud cover varies. ESSA, in its publication Climatological Data, National Summary, provides, on an ongoing basis, monthly means of sky cover of selected stations. These are given in tenths of cover for sunrise to sunset. ESSA's Northern Hemisphere Data Tabulations give cloud cover amounts for each day.

Sherr et al. (1968) give percentage frequencies of occurrence for their cloud cover classes for individual stations averaged for summer and winter as compiled from various sources. These are given as a function of the hour of the day. Each station represents at least ten years of data.

Some consideration should be given as to the accuracy of satellite cloud observations and how they compare to surface observations. Glaser et al. (1968) have carried out a comparison of cloud amounts as reported for the same locations and times by satellite and surface observations. Systematic differences are observed to exist, with the satellite observations showing smaller cloud cover

values. Various reasons are suggested for the discrepancy. Generally the satellite is looking at a considerably larger portion of the sky than the ground observer is. Also the limited resolving power of the satellite means that small amounts of cloud cover may simply not be observed. In addition there is a tendency for ground observers to overestimate the cloud cover because they are looking at the cloud sides as well as the bases. McCabe (1965) notes that half of the sky dome over which the ground observer visually integrates to get the cloud cover is less than 30^{o} above the horizon and thus it is possible that a substantial part of the sky is blocked to the observer's view by the cloud sides. Barnes (1966) feels that this is the primary reason for the discrepancy. Clapp (1964) has also noticed that the satellite cloud cover amounts are consistently less than those observed from the ground. He concurs with Glaser et al. as to the reasons for these differences.

Barnes and Chang (1968) have carried out an extensive analysis of the two types of cloud cover observations. Contrary to the previous results they found no significant differences in cloud amounts when viewed from the surface and from space as long as the sizes of the viewing areas were approximately equal. Only with cirrus clouds do the satellite observations fall below the ground amounts. They suggest that the conclusions of the earlier studies might have resulted from the use of nephanalyses in which cloudiness was integrated over larger areas, from differences in the time at which the satellite and ground observations were made, and from using satellite photographs of poorer quality than those used in their study. Their conclusions

are qualified by pointing out that the geographic area over which their study was made is rather limited.

It would seem then that there is still some question as to the quality of the satellite nephanalyses being carried out. Therefore, in comparing the cooling rates carried out using surface observations to those obtained using satellite observations it will be helpful to keep in mind the biases which may be entering as the result of errors in the cloud cover amount.

London (1957) and Davis (1961, 1963), in their examinations of the atmospheric heat balance, used the northern hemisphere total cloud cover amounts determined by Telegadas and London (1954) for the summer and winter and by Seide (1954) for the spring and fall. Katayama (1966) adopted Shaw's total cloud cover values while criticizing them, quite legitimately, as being rather outdated. Sasamori et al. (1971) in their Southern Hemisphere radiation budget study used the values given by van Loon (1971). Since this represents the most complete compilation of total cloud cover for the Southern Hemisphere, it has also been used in this study.

Dopplick's (1970) global study is the only one which employs satellite observations to determine the total cloud cover. The E. T. A. C. results for 1964 which were discussed earlier were used for the Southern Hemisphere Except for high latitudes Dopplick doesn't indicate the source of his southern hemisphere values. For the high latitudes, zonal mean amounts given by Gabites were used. Unfortunately, Gabites's results were not available for this work.

TABLE (II-1) TOTAL CLOUD COVER SUMMARY

Author or Title	Area Covered	Form of Data	Remarks
C. E. P. Brooks (1927)	globe	ann. climat. lat. means in % cloud cover given sep. for land, ocean, and mean	tables
N. Shaw (1936)	globe	ann. and mo. climat. means in 1/10 cloud cover	maps prepared by Brooks 1921
W. F. McDonald (1938)	oceans	seasonal climat. means in 1/10 cloud cover	maps
B. Haurwitz and J. Austin (1944)	globe	Jan. and July climat. means in 1/10 cloud cover	maps
H. Landsberg (1945)	globe	Jan., Mar., May, July, Sept., Nov. climat. means in 1/10 cloud cover	maps in Handbook of Meteorology
R. N. Seide (1954)	N. Hemi.	spring and fall climat. lat. means in % cloud cover	graphs
K. Telegadas and J. London (1954)	N. Hemi.	summer and winter climat. means in 1/10 cloud cover	maps
W. D. Sellers (1958)	6 Ariz. cities	mo. means (1948-58) for var. hrs. of the day in 1/10 cloud cover and in freq. distr. for each 1/10 cloud cover	tables
F. E. Elliott (1960)	U. S. S. R.	mo. climat. means in 1/10 cloud cover	maps
M. Schloss (1962)	U. S. S. R.	summer and winter climat. means in % cloud cover	maps
E. de Bary and F. Moller (1963)	Germany	summer and winter morning and afternoon means (1936-40) in % cloud cover for diff. layers of the atm.	tables and graphs

P. F. Clapp (1964)	60°N-60°S around the globe	daytime means for Mar. - May 62, June-Aug. 62, Sept. - Nov. 62, and Dec. 62 - Feb. 63 in % cloud cover separately for sfc. and satellite obs.	maps; sfc. obs. from Landsberg
L. J. Allison and G. Warnecke (1967)	85°W-160°W 25°N-20°S	mo. daytime means for Jan. 1964 in 1/10 cloud cover-satellite obs.	maps
P. F. Clapp (1968)	N. Hemi.	late fall daytime means for each of the years 1962, 63, and 64 in % cloud cover	maps
A. H. Glaser et. al. (1968)	100°E-130°W 37°N-37°S	means for 15 May-31 Aug. 66 and 9 Oct. 66-28 Feb. 67 in % cloud cover-satellite obs.	maps mainly along coastal areas
F. A. Godshall (1968)	30°N-30°S 90°W-120°E	mo. means (1961-1965) for Jan. and Aug. in 1/10 cloud cover-satellite obs.	maps
E. Raschke (1968)	N. Hemi.	means for 16-31 May 66, 1-15 June 66, 16-30 June 66, 1-15 July 66, 16-31 July 66 in 1/10 cloud cover.	maps from E. T. A. C.
J. Sadler (1968)	30°N-30°S around the globe	daily means for each day from Feb. 65 to Jan. 68 in 1/8 cloud cover, mo. means for each mo. from Feb. 65 to Jan. 68 in 1/8 cloud cover-satellite obs.	daily means on tape, mo. means on maps
P. Sherr et al. (1968)	globe and selected stations	mo. (for globe) and summer and winter (for stations) climat. means for var. hrs. of the day in freq. distr. of fractions of cloud cover-satellite and sfc. obs.	globe divided into to 29 geog. areas each having homogeneous cloud cover; globe-tables; stations-graphs
L. J. Allison et al. (1969)	70°N-10°N around the globe	mo. means for each mo. from June 63 to Dec. 64 in 1/10 cloud cover	maps
Environmental Technical Applications Center (1969)	N. Hemi.	mo. means (Sept. 63-Aug. 68) for 0000 and 1200 Z in 1/8 cloud cover and in freq. distr. for each 1/8 cloud cover	computer output

F. A. Godshall et al. (1969)	$30^{o}N-25^{o}S$ $100^{o}W-130^{o}E$	mo. means for each Jan., Apr., Aug., and Oct. from Aug. 62 to Jan. 69 in 1/10 cloud cover-satellite obs.	maps
van Loon (1971)	globe	Jan. and July climat. means in % cloud cover	tables; no inf. as to whether satellite or sfc. obs. or both used
Climatic and Oceanographic Atlases for Mariners	oceans of world	mo. climat. means in freq. distr. of cover $\leq$2/10 cloud cover and 8/10 cloud cover	maps mostly adapted from U. S. Navy Marine Climatic Atlases of the World
U. S. Navy Marine Climatic Atlases of the World	oceans of world and selected stations	mo. climat. means in freq. distr. of var. amt. of cloud cover	maps and histograms; add. inf. given for low clouds
Air Force Summaries of Surface Weather Observations, Parts A and B	selected stations around globe	mo. means in 1/10 cloud cover and in freq. distr. for groups of 1/10 cloud cover based on various periods of time	tables
Air Weather Service N Summary #17	selected stations around globe	mo. means in 1/8 cloud cover and in freq. distr. for groups of 1/8 cloud cover based on various periods of time	tables
Climatological Data National Summary	selected stations around globe	ann. and mo. daytime means in 1/10 cloud cover for each mo. of each yr. available	tables being continuously compiled
Revised Uniform Summary of Surface Weather Obs. Part D	selected stations around globe	ann. and mo. means (for various hrs.) in 1/10 cloud cover and in freq. distr. for groups of 1/10 cloud cover based on various periods of time	tables; no obs. prior to 1945

A. Arking	globe	seasonal means for each season from July 62 to Dec. 64	work incomplete
C. S. Ramage et al.	Indian Ocean	mo. means for each mo. from 1963 to 1964	work incomplete

II-3.3 Cloud Cover by Type

Although some work has been done by Fritz and Winston (1962), Rao and Winston (1963), Bristor et al. (1966), and Barnes and Chang (1968) in distinquishing between high, middle, and low clouds using satellite observations of black body equivalent temperatures, no usable direct measurements of cloud cover for different cloud types are presently available. Therefore, it has been necessary to infer these cloud cover amounts from other observations more readily available.

Katayama (1966), in his radiation budget study, has estimated the amount of cloud cover for each cloud type using the expression

$$C_j = Cm_j N_j / \Sigma_j (m_j N_j) \qquad \text{(II-3)}$$

where C_j is the cover for cloud type j, m_j the mean cloud amount per occurrence of type j, N_j the frequency of occurrence of type j, and C the total cloud cover. Since relatively little is known about the seasonal and geographical variation of m_j, Katayama has assumed that a single set of values holds for all his calculations. London (1957) has used a simpler expression of the form

$$C_j = CN_j \qquad \text{(II-4)}$$

Given the lack of information as to the values of m_j, there is little point in using Katayama's more involved procedure and therefore (II-4) is used in our calculations.

On a global scale the only values of N_j available are those given in McDonald's (1938) climatic atlas of the oceans in which he divides

the different cloud types into the following groups

(1) cirrus, cirrostratus, cirrocumulus; designated Ci

(2) altocumulus, altostratus; designated As

(3) cumulus; designated Cu

(4) stratus, stratocumulus; designated St

(5) cumulonimbus; designated Cb

(6) nimbostratus; designated Ns

We have adopted both his classification scheme and his frequency values except that Cu and Ns have been combined to form a new "low" cloud category. It is assumed that Cu and Ns do not occur simultaneously and therefore the low cloud frequency equals the sum of the Cu and Ns frequencies.

In his introduction McDonald states that since his results are all derived from surface observations, the values for As and Ci will be underestimated when lower clouds are present. Also even though information about the different cloud types was not collected in more than two thirds of the observations, the frequencies were based on the total number of observations made. Finally, he comments that since only observations made around Greenwich noon were used, there was some trouble in seeing cirriform clouds over the Pacific Ocean where Greenwich noon falls during the night hours. This also presents another problem since by collecting the observations at different local times, they cannot really be regarded as being entirely comparable. Variations in amount that appear to be due to changes in latitude or longitude may in fact be due in part to the differing conditions at different local times of day.

In order to correct for the underestimation of As and Ci we have utilized a procedure suggested by Telegadas and London (1954) which assumes that the ratio of the observed cloud cover of As or Ci to the total observed sky is equal to the same ratio for the entire sky. A correction has also been applied to the cirroform clouds over the Pacific, the frequency of occurrence having been increased approximately 20 to 25% in that region to compensate for the difficulty in observing cirroform clouds during the night. This increase brings the frequencies over the Pacific into better agreement with those over the Atlantic and Indian Oceans.

McDonald's frequency values generally do not extend poleward of 50°S and there is little other data directly available for this region. In order to provide the necessary data it has been assumed that the Southern Hemisphere in this area has a cloud cover which can be approximated by that in the Northern Hemisphere for similar seasons and regions. Sherr et al. (1968) have examined this assumption and found that the globe can be divided into twenty nine homogeneous cloud climatic regions and that some of these regions can be paired as seasonal reversals. In order to examine the validity of seasonal pairing for the data we have available two regions which are paired by Sherr et al. and for which McDonald has data. The similarities are great enough to justify using this approach especially in the absence of more substantial cloud cover information. In the polar regions, for which McDonald has no values in either the Southern or northern hemisphere, pairings have been carried out with the zonally averaged frequencies supplied

by Telegadas and London (1954) for the Arctic. Where this procedure has been used it has been impossible to introduce much longitudinal variation in the frequencies but then it is also true that there probably is very little such variation in these polar latitudes given the uniform zonal distribution of ocean surface. The zonal variations that do appear are the result of forcing the polar frequencies to blend smoothly with McDonald's values north of 50^{o}S.

Since McDonald's atlas only provides frequencies of occurrence by type for the oceans, it has been necessary to find other sources of data for the three continental areas of the southern hemisphere. This has not been difficult for Australia. A substantial part of that land mass can be characterized as having a desert climate while the surrounding waters have rainy climates. Also if we look at the total cloud cover based on van Loon's data for both the summer and winter, there is a distinct local minimum of cover over Australia, the total cover being substantially lower in the winter season (July). Furthermore, Shaw's (1936) rainfall maps for January and July show local minimum values over the continent with smaller amounts in July than in January. This latter information is relevant primarily to Ns cover.

Thus in general we can conclude that for Australia cloudiness will decrease from water to land and from summer to winter. Fortunately we do have more extensive information for some of the cloud categories. Sellers (1958) has studied the frequency by type over Arizona and on the basis of similarities in the two climates his data can be used for Australia. Sherr et al. (1968) reach the same

conclusion in their study of cloud regimes. No quantitative attempt has been made to fit the Arizona data to Australia because that data is based on observations from six cities and shows considerable variability. Qualitatively however, it is quite helpful in identifying how the frequencies vary as a function of season.

Using the above information, McDonald's oceanic data have been extrapolated over the continent. This extrapolation has been done rather subjectively but represents a reasonable approximation to the continental frequency distributions. Over Arizona Ac, Cb, and Cu show local maxima in frequency in the summer, St a local maximum in the winter, and Ci doesn't exhibit any distinct seasonal variation. Since Ns coverage isn't examined by Sellers, Shaw's (1936) precipitation maps are used to determine that Ns occurs more frequently in the summer season.

For Cb, in addition to Sellers' work, Haurwitz and Austin (1944) present plates of the thunderstorm activity for each half year. For the period from April through September there is a region of local minimum activity in the northern half of Australia, a minimum both with respect to the rest of Australia and the surrounding oceans. Along the western half of the southern shoreline there is a zone of local maximum activity. Between October and March the activity is more zonally distributed, as it is over the oceans, decreasing toward the pole. There is a small center of local maximum activity in the southeastern quarter of the country with a subsequent decrease eastward toward the Pacific. The greatest seasonal activity occurs from October to March.

Whereas Australia can be characterized rather simply climatically no such convenient approach is possible for South America or Africa. Nor do we have available the sort of data Sellers provides for Arizona. For Cb the thunderstorm plates of Haurwitz and Austin are again used. These plates indicate greater thunderstorm activity for the summer season and therefore greater Cb frequencies. For Ns Shaw's precipitation maps are employed. In July over South America and Africa rainfall decreases inland quite rapidly. In January the precipitation has local maxima over western Brazil and Rhodesia and is somewhat larger than in July.

For the remaining four cloud types little can be done other than to assume that the frequencies decrease inland, and extrapolate McDonald's oceanic values onto the land areas. In order to improve this approach, Koppen's scheme of climatic classification is used to identify land regions which possess climatic characteristics similar to ocean regions where cloud frequencies are known.

It has been assumed that the seasonal variations in frequency of occurrence for the different cloud types over Africa and South America parallel those of the total cloud cover. This means that frequencies will be greater during the summer season. It should be pointed out that when the continental frequencies are fitted to the surrounding oceanic values the seasonal variations of Cu and St are negligible over South America.

Three other sources of information for the frequencies of occurrence of different cloud types exist but proved not to be useful in this study. Changnon and Huff (1957) have carried out a study at various stations in Illinois, and Clodman (1957) studied

cirrus cover over Canada. In addition, the data summaries compiled by the United States Air Force and ESSA, mentioned earlier in the discussion of total cloud cover, provide frequency reports, distinguishing however only between high and low clouds.

McDonald's frequencies of occurrence for each cloud type were used by London, Davis, Katayama, and Sasamori et al. The latter two studies also employed various local sets of observations, all but one of which was available to this study. Only minor variations in his grouping into types were adopted.

Dopplick, as he did for the total cloud cover, used satellite observations to determine cover by type, utilizing a procedure developed at the University of Wisconsin. Because of the lack of vertical resolution in the satellite data the clouds were only divided into three types.

II.3.4 Clouds as Black Bodies

The question arises as to whether or not, for the purposes of this work, clouds can be treated as black bodies. McDonald (1960) considered this problem for liquid water clouds and found that for a cloud having the rather low liquid water content of 0.25 grams per m^3 ninety percent of the incident infrared radiation is absorbed within the first 100 meters of the cloud. For a more typical value of 1.0 grams per m^3 ninety percent abosrption occurs within 26 meters.

Havard (1960), in a theoretical study of this problem, demonstrated that for a cloud composed of 6 micron droplets with a liquid water content of 0.1 grams per m^3, a thickness of 60 meters is

required before the cloud can be considered an effective black body. Widger et al. (1966) arrived at similar conclusions for clouds of "reasonable thickness," excluding cirroform clouds.

Since cloud thickness generally exceeds the depths studied by McDonald, Havard, and Widger et al., it is reasonable to treat all but the cirrus clouds as black bodies.

Fritz and Winston (1962), in their satellite measurements observed situations which suggested that cirrus are not black bodies. For thin cirrostratus overlying an altostratus layer they found an equivalent temperature for the 10 micron water vapor window corresponding more closely to the height of the altostratus than the cirrus. Of course as the cirrus deck becomes thicker the equivalent temperature decreases, but for many cirrus clouds it would appear that the black body assumption is not tenable. On the basis of such observations Katayama (1966) chose to treat cirrus clouds as gray bodies by reducing the cirrus cloud cover amounts by 50%. Manabe and Strickler (1966) adopted the same approach, while London (1957), Davis (1961, 1963), Rodgers and Walshaw (1966) and Dopplick (1970) treated cirrus as black bodies.

However, Fritz and Rao (1967) examined the transmission through cirrus clouds for radiation at 6 and 10 microns. At a temperature of 225^{o}K, the approximate mean annual hemispheric temperature for the cirrus clouds, they computed a transmissivity of about .02 at 6 microns and .66 at 10 microns. This was done for a cloud 5 km thick whereas the cirrus used in this study range in thickness from 1.1 to 1.8 km. Kuhn and Weickmann (1969) calculated

the cirrus transmissivities as a function of cloud thickness for the region from 8 to 13 microns based on aircraft measurements. For a thickness of 1.5 km they found a transmissivity of about .85.

Rather than attempting to characterize the cirrus transmissivity uniquely over the entire infrared spectrum, we divided the spectrum into two regions, one to be characterized by Fritz and Rao's relatively opaque 6 micron region and the other by their relatively transparent 10 micron region. Since Fritz and Rao's results were based on a cirrus thickness which is considerably greater than that used here, Kuhn and Weickmann's calculations, which also considered cloud thickness, were incorporated. For the portions of the infrared spectrum which are relatively opaque, a transmissivity of 0.05 is used and for those which are relatively transparent a transmissivity of 0.80 is used. For these considerations the 80 micron band from 0 to 500 cm^{-1} and the 6.3 micron band from 1250 to 2450 cm^{-1} are viewed as being nearly opaque while the remaining wave numbers are viewed as being nearly transparent.

II-3.5 Cloud Temperatures

Given the net cooling that generally occurs at the upper surface of a cloud it is reasonable to assume that the air temperature in the vicinity of the upper cloud surface will be somewhat warmer than the cloud surface itself. James (1959) has observed this to be the case above stratocumulus clouds. However, since data as to cloud temperatures are unavailable, the radiating temperature of the cloud will be assumed to be equal to the air temperature at the

cloud's boundaries.

It should be mentioned that some work has been done to determine cloud temperatures using satellites. In wavelength regions where atmospheric absorption of infrared radiation is low it is possible to calculate the temperature of a black body in order for it to emit the radiation observed by the satellite. Then if information is available as to the type and height of the cloud present, the black body temperature represents an approximation to the cloud's temperature.

II-3.6 Cloud Heights

Hann and Suring, in various editions of the Lehrbuch der Meteorologie, and Shaw (1936) give cloud heights for different cloud types for a series of land stations located primarily in Europe and along the eastern coast of the United States. Latitudinal variations in height for different cloud types were investigated by Ishimaru (1952). From a number of aircraft reports over Canada, Clodman (1957) observed a tendency for the base of cirrus clouds to be at the level having a temperature of $-40^{\circ}C$. The most extensive surveys are those of Telegadas and London (1954) and Seide (1954). They compiled all the available data and calculated longitudinally averaged heights for each season for each of McDonald's six cloud types.

Satellite observations of radiation are also being used in an attempt to identify cloud heights. This can be done if the temperature structure of the atmosphere is known at the time of the

observation. At this moment these programs are still in an experimental stage. It is entirely reasonable, however, to anticipate that there will be a substantial contribution to the data in this area within the next few years.

Katayama (1966), following the work of Ishimaru (1952) and Clodman (1957), developed expressions for the heights of the different cloud types as functions of pressure. From the observed surface pressure and the pressure at -40°C (which he assumes to be at the height of the cirrus base) he derived expressions for the heights of the various cloud types. Using London's (1957) climatological values of pressure and temperature we calculated cloud heights on the basis of Katayama's scheme and compared them to those given by Telegadas and London (1954). The comparison is not particularly good. The average difference for Ns is 0.3 km and for St, Cu and Cb about 0.5 km. However for Ci the average difference is 0.9 km with individual differences of up to 2.1 km and for As it reaches 2.4 km with individual differences of over 3 km. Because of these inconsistencies, Katayama's procedure has not been used in this study.

In the absence of additional information, we used Telegadas and London's (1954) longitudinally averaged heights for the northern hemisphere. Such a procedure can be criticized but there appears no other better alternative. It should be noted that their results are based primarily on observations made over land. Since it is reasonable to assume that the latitudinal variations which occur in observations made exclusively over land and water are similar in shape and differ primarily by a scaling factor, the use of these

heights for the Southern Hemisphere, which is covered primarily by ocean surface, will only introduce errors in the absolute magnitudes of the heights and not in their relative latitudinal variations.

Telegadas and London's (1954) cloud heights for McDonald's six cloud types are given for ten degree latitude belts. For each belt the bases of the low (Cu and Ns), Cb, and St clouds are forced to lie at the same level, their common base being formed from the weighted mean of the bases of the four original cloud types. The tops of the low clouds are similarly calculated from the Cu and Ns tops. In addition, the cloud heights are further adjusted by requiring their tops and bases to coincide with the nearest interface between atmospheric layers, an approximation to make the cooling rate calculations tractable.

Tops and bases are presented by Telegadas and London (1954) for all but St and Ci for which only bases are given. Thicknesses equal to that of one atmospheric layer (65 mb) are assumed for these two cloud types. This requires that St thicknesses range from about .5 to .75 kilometers while Ci thicknesses range from about 1.1 to 1.8 kilometers. These thicknesses agree well with those reported by Tverskoi (1965).

Due to a lack of quantitative information, no attempt was made to incorporate a scaling factor to account for the differences between heights over land and water. In a few cases the constraints placed on the cloud model produce results which are obviously incorrect in terms of latitudinal variations. In such instances the heights and thicknesses are altered so as to produce more realistic

cloud distributions. Fig. (II. 3) presents the various cloud configurations which are used in this study.

In conclusion, it is appropriate to quote from Walshaw (1966), viz., "There is no satisfying way of dealing with these tiresome objects."

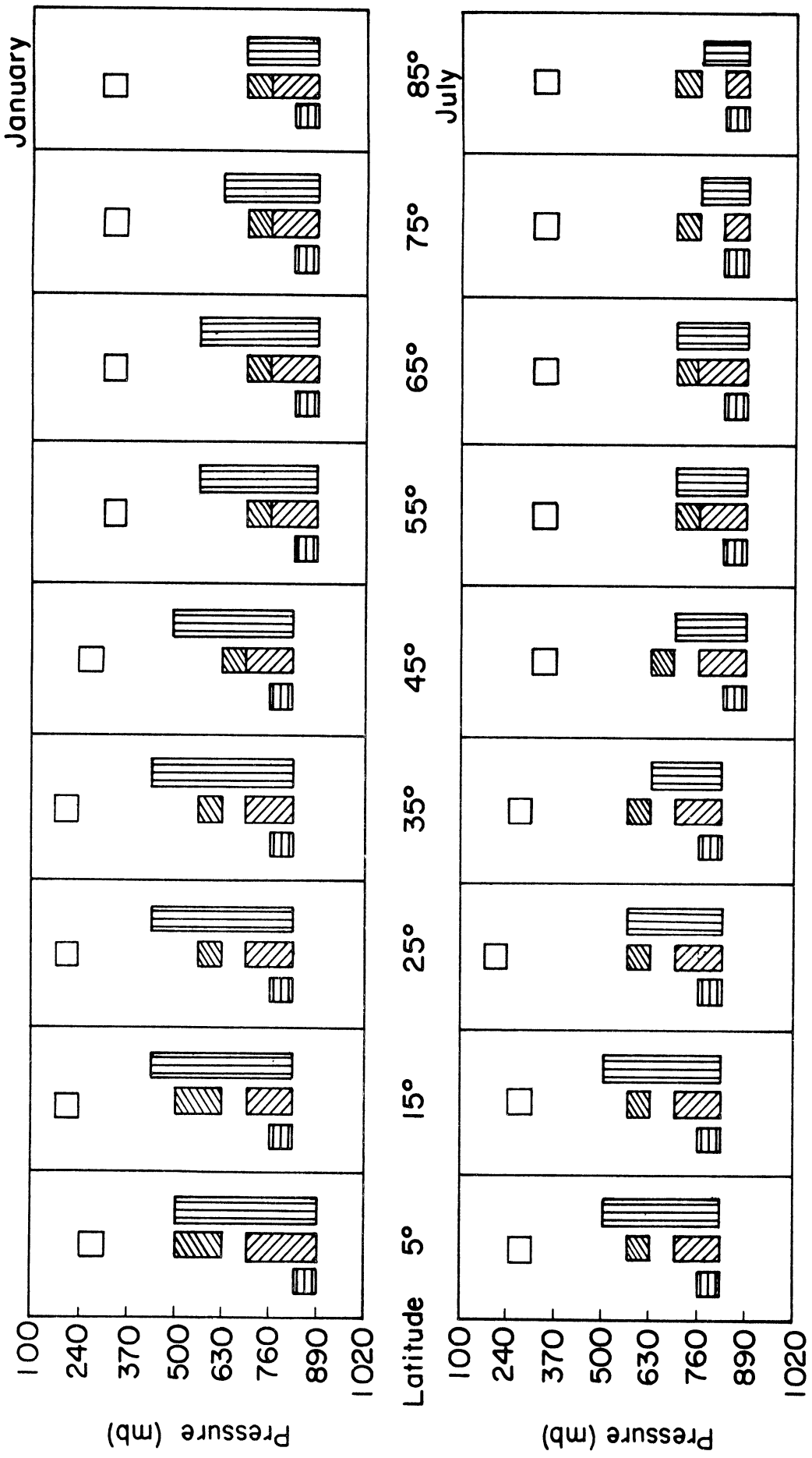

Figure II-3 Latitudinal distributions of cloud heights; this figure should not be viewed as indicating the degree of cloud overlap

CHAPTER III

METHODOLOGY FOR THE CALCULATION OF RADIATIVE HEATING AND COOLING RATES

III-1 THE TRANSFER EQUATION

The rate of temperature change resulting from the divergence of radiative flux can be expressed as follows,

$$\left(\frac{\partial T}{\partial t}\right)_{x, y, z} = -\frac{1}{\rho_a c_p}\left(\frac{\partial \mathcal{F}}{\partial z}\right)_{x, y, t} \qquad \text{(III-1)}$$

where

$\left(\frac{\partial T}{\partial t}\right)_{x, y, z}$ = local rate of change of temperature

ρ_a = mass density of air

c_p = specific heat of air (at constant pressure)

$\left(\frac{\partial \mathcal{F}}{\partial z}\right)_{x, y, t}$ = vertical radiative flux divergence

By introducting the hydrostatic equation (III-1) can also be written,

$$\left(\frac{\partial T}{\partial t}\right)_{x, y, z} = \frac{g}{c_p}\left(\frac{\partial \mathcal{F}}{\partial p}\right)_{x, y, t} \qquad \text{(III-2)}$$

Thus, if it is possible to calculate the radiative flux as a function of pressure, we can immediately evaluate the radiative component of the temperature change. This can be done by introducing the radiative transfer equation for a plane parallel atmosphere (Kourganoff, 1962), which relates the attenuation of the radiation at a given wavelength to

the amount of absorbing medium being traversed and the resulting absorption and emission. Molecular scattering is neglected since we are concerned with the infrared portion of the spectrum, and at these wavelengths, scattering, which is inversely proportional to the fourth power of the wavelength is negligible. The radiative transfer equation can then be written as follows,

$$\frac{dI_\omega(\theta)}{dz} = -k_\omega \rho_g [I_\omega(\theta) - S_\omega(\theta)] \sec\theta \qquad \text{(III-3)}$$

I_ω = specific intensity of radiation at wave number ω

k_ω = monochromatic mass absorption coefficient

ρ_g = mass density of the gaseous medium

S_ω = source function, the ratio of the emission to the absorption coefficient

θ = angle made by the specific intensity and the outwardly drawn normal to the surface

It is convenient to define a quantity, the mass path, as,

$$du = \rho_g dz \qquad \text{(III-4)}$$

where du is a measure of the amount of absorbing gas in a vertical column having height dz and is measured so as to increase upward. The units of u are generally either gm per cm^2 column or atm cm of absorbing gas. The transfer equation can also be given for both upward and downward radiation beams where the specific intensity is positive in the direction of propagation of each beam:

$$\frac{dI^{\uparrow}_\omega(\theta)}{du} = -k_\omega [I_\omega(\theta) - S_\omega(\theta)] \sec\theta \qquad \text{(III-5)}$$

$$\frac{dI^{\downarrow}_\omega(\theta)}{du} = k_\omega [I_\omega(\theta) - S_\omega(\theta)] \sec\theta \qquad \text{(III-6)}$$

If the radiation emitted by the earth's surface, $B_\omega(0)$, is isotropic, and the surface radiates as a blackbody, then integrating (III-5) between the surface (u=0) and some level ($u=u_o$) at which the radiative flux is desired yields,

$$I^{\uparrow}_{\omega}(u_o, \theta)=B_{\omega}(0)e^{-k_\omega \sec\theta u_o}+\int_{o}^{u_o} e^{-k_\omega (u_o-u)\sec\theta} k_\omega S_\omega(u, \theta)\sec\theta du \qquad \text{(III-7)}$$

For the downward radiation, if we assume that the specific intensity is zero at the top of the atmosphere ($u=u_\infty$), and integrate from u_∞ to u_o,

$$I^{\downarrow}_{\omega}(u_o, \theta)=\int_{u_o}^{u_\infty} e^{-k_\omega (u-u_o)\sec\theta} k_\omega S_\omega(u, \theta)\sec\theta du \qquad \text{(III-8)}$$

In both equations the limits of integration are such that the powers of the exponential term are always negative. Thus the following term,

$$\tau_\omega(u_o, u, \theta)=e^{-k_\omega \sec\theta \,|u-u_o|} \qquad \text{(III-9)}$$

can be introduced and the equations become,

$$I^{\uparrow}_{\omega}(u_o, \theta)=B_{\omega}(0)\,\tau_\omega(u_o, 0, \theta)+\int_{o}^{u_o} \tau_\omega(u_o, u, \theta) k_\omega S_\omega(u, \theta)\sec\theta du \qquad \text{(III-10)}$$

and

$$I^{\downarrow}_{\omega}(u_o, u, \theta)=\int_{u_o}^{u_\infty} \tau_\omega(u_o, u, \theta) k_\omega \sec\theta S_\omega(u, \theta) du \qquad \text{(III-11)}$$

The term, τ_ω, the monochromatic transmission function, is considered in a later section.

Because of the large number of absorption lines and their irregular shapes, an integration of (III-10) and (III-11) would be so time consuming as to be impractical. Instead, averages are formed over subintervals of the absorption band from $\omega_o-\delta/2$ to $\omega_o+\delta/2$. These take the form,

$$I^{\uparrow\downarrow}_{\delta}(u_o, \theta) = \frac{1}{\delta}\int_{\delta} I^{\uparrow\downarrow}_{\omega}(u_o, \theta) d\omega \qquad \text{(III-12)}$$

If we assume that the source function and blackbody surface radiation are constant over the subinterval, then,

$$\bar{I}^{\uparrow}_{\delta}(u_o\theta) = B_{\omega_o}(0)\,\frac{1}{\delta}\int_{\delta}\tau_{\omega}(u_o, 0, \theta)\,d\omega + \int_{o}^{u_c} S_{\omega_o}(u, \theta)\,\frac{1}{\delta}\int_{\delta}\tau_{\omega}(u_o, u, \theta)\,k_{\omega}\sec\theta\,d\omega\,du \qquad \text{(III-13)}$$

and

$$\bar{I}^{\downarrow}_{\delta}(u_o, \theta) = \int_{u_o}^{u_\infty} S_{\omega_o}(u, \theta)\,\frac{1}{\delta}\int_{\delta}\tau_{\omega}(u_o, u, \theta)\,k_{\omega}\sec\theta\,d\omega\,du \qquad \text{(III-14)}$$

In (III-12) a mean expression for I_{ω} was formed; in a similar way, one can define a mean transmission function over a δ interval,

$$\tau_{\delta}(u_o, u, \theta) = \frac{1}{\delta}\int_{\delta}\tau_{\omega}(u_o, u, \theta)\,d\omega \qquad \text{(III-15)}$$

Then

$$\frac{d\tau_{\delta}}{du}(u_o, u, \theta) = \pm\,\frac{1}{\delta}\int_{\delta} k_{\omega}\sec\theta\,\tau_{\omega}(u_o, u, \theta)\,d\omega \qquad \text{(III-16)}$$

and (III-13) and (III-14) become

$$\bar{I}^{\uparrow}_{\delta}(u_o, \theta) = B_{\omega_o}(0)\,\tau_{\delta}(u_o, 0, \theta) + \int_{o}^{u_o} S_{\omega_o}(u)\,\frac{d\tau_{\delta}}{du}(u_o, u, \theta)\,du \qquad \text{(III-17)}$$

and

$$\bar{I}^{\downarrow}_{\delta}(u_o, \theta) = -\int_{u_o}^{u_\infty} S_{\omega_o}(u)\,\frac{d\tau_{\delta}}{du}(u_o, u, \theta)\,du \qquad \text{(III-18)}$$

Summing over the subintervals which span the band, we obtain the integrated intensity, per unit area, per unit time, per unit solid angle,

$$\mathcal{I}^{\uparrow}(u_o, \theta) = \sum_i \delta_i\,\bar{I}^{\uparrow}_{\delta_i}(u_o, \theta) \qquad \text{(III-19)}$$

or,

$$\mathcal{I}^{\uparrow}(u_o, \theta) = \sum_i \delta_i \left\{ B^{i}_{\omega_o}(0)\,\tau_{\delta_i}(u_o, \theta) + \int_{o}^{u_o} S^{i}_{\omega_o}(u)\,\frac{d\tau_{\delta_i}}{du}(u_o, u, \theta)\,du \right\} \qquad \text{(III-20)}$$

$$\mathcal{I}^{\downarrow}(u_o, \theta) = \sum_i \delta_i \int_{u_\infty}^{u_o} S^{i}_{\omega_o}(u)\,\frac{d\tau_{\delta_i}}{du}(u_o, u, \theta)\,du \qquad \text{(III-21)}$$

To express the equations in terms of energy flux, an integration over the hemisphere is required;

$$\mathcal{F}^{\uparrow\downarrow}(u_o) \int_0^{2\pi} \int_0^{\pi/2} \mathcal{I}^{\uparrow\downarrow}(u_o, 0) \sin\theta \cos\theta \, d\theta \, d\phi \qquad \text{(III-22)}$$

It is convenient to expand the definition of the transmission function to include an expression referred to as the flux transmission:

$$\tau_{f_{\delta i}}(u_o, u) = 2 \int_0^{\pi/2} \tau_{\delta_i}(u_o, u, \theta) \cos\theta \sin\theta \, d\theta \qquad \text{(III-23)}$$

The integrated fluxes can then be written,

$$\mathcal{F}^{\uparrow}(u_o) = \sum_i \delta_i \pi \left\{ B^i_{\omega_o}(0) \tau_{f_{\delta_i}}(u_o, u=0) + \int_0^{u_o} S^i_{\omega_o}(u) \frac{d\tau_{f\delta i}}{du}(u_o, u) \, du \right\} \qquad \text{(III-24)}$$

and

$$\mathcal{F}^{\downarrow}(u_o) = \sum_i \delta_i \pi \int_{u_\infty}^{u_o} S^i_{\omega_o}(u) \frac{d\tau_{f\delta i}}{du}(u_o, u) \, du \qquad \text{(III-25)}$$

III-2 THE TRANSMISSION FUNCTION

In developing the transfer equation we introduced the following expression for the monochromatic transmission function,

$$\tau_\omega(u_o, u, \theta) = e^{-k_\omega \sec\theta \, |u-u_o|}$$

where $\tau_\omega(u_o, u, \theta)$ is a measure of the depletion that I_ω suffers as it traverses a mass path of length $|u-u_o|$. Also, to incorporate the angular dependence, the flux transmission function was defined as in (III-23). To simplify this integration the angular dependence can be removed by approximating the angular integration by a "mean path", for which $\sec\theta = 1.667$, i.e., $\tau_{\delta_i}(u_o, u, \theta)$ is replaced by $\tau_{\delta_i}(u_o, u' = 1.667u)$ and,

$$\tau_{f_{\delta_i}}(u_o, u) = 2\tau_{\delta_i}(u_o, u') \int_0^{\pi/2} \cos\theta \sin\theta d\theta$$

$$= \tau_{\delta_i}(u_o, u') = \frac{1}{\delta} \int_{\delta}^{o} e^{-k_\omega 1.667 |u-u_o|} d\omega \quad \text{(III-26)}$$

By using this approximation the true mass path is replaced by an effective or slab mass path 1.667 times longer. This multiplicative factor is generally referred to as the diffusivity factor and has been approximated differently by various investigators. Elsasser(1942) used a value of 1.66 while Plass (1956b) allowed it to vary as a function of the transmission. Recently, Armstrong (1968) has extensively investigated the significance of this approximation. This value, 1.667, represents a reasonable compromise between the larger values which hold for regions of weak absorption or small mass path and the smaller values which hold for regions of strong absorption or large mass path.

III-3THE ABSORPTION COEFFICIENT

III-3.1 Lorentz Broadening

For an isolated and stationary molecule the half widths of the absorption and emission lines correspond to the finite widths of the energy levels. These natural line widths are only about 10^{-11} cm^{-1} (Goody, 1964) and are negligible for atmospheric calculations. However atmospheric molecules are neither stationary nor isolated and therefore the line widths undergo substantial broadening due to collisions (Lorentz or collision broadening) and the effect of their own velocities (Doppler broadening). In the troposphere where collisions between molecules are frequent, Doppler broadening is considerably smaller than Lorentz broadening and therefore can be neglected in these calculations.

The absorption coefficient at wave number ω due to a line centered at ω_o, under the effect of Lorentz broadening is,

$$k_\omega = \frac{S}{\pi} \frac{\alpha}{(\omega - \omega_o)^2 + \alpha^2} \qquad \text{(III-27)}$$

where S is the line intensity, α the half width, and $\int_{-\infty}^{\infty} k_\omega d\omega = S$

III-3.2 Broadening as a Function of Temperature and Pressure

The broadening as expressed in the half width is a function of temperature and pressure. If the half width is related to some standard temperature and pressure (T_o, p_o) the following correction is appropriate,

$$\frac{\alpha}{\alpha_o} = \frac{p}{p_o} \sqrt{\frac{T_o}{T}} \qquad \text{(III-28)}$$

For the range of temperatures found in the troposphere the square root portion of the correction can be disregarded; thus,

$$\alpha = \alpha_o \left(\frac{p}{p_o} \right) \qquad \text{(III-29)}$$

It should be noted that α_o is not constant for different lines within the same band. Mean values have been calculated for each band and are discussed in later sections of this chapter.

III-3.3 Non-Homogeneous Path Approximation

An additional correction must be applied to the half width to take into account the variations in pressure over the transmission path. Curtis (1952) and Godson (1955) independently developed such a correction. They approximated α by,

$$\alpha = \frac{\int \alpha \, du}{\int du} \qquad \text{(III-30)}$$

Then substituting (III-29) into (III-30)

$$\alpha = \frac{\alpha_o}{p_o} \frac{\int p\,du}{\int du} \qquad \text{(III-31)}$$

The correction factor, the Curtis-Godson pressure,

$$P_{cg} = \frac{\int p\,du}{\int du} \qquad \text{(III-32)}$$

and can be thought of as a mean or homogeneous pressure representative of the actual pressure which varies over the mass path.

Rodgers and Walshaw (1963, 1966) investigated the error introduced by using the Curtis-Godson pressure. They calculated both the cooling rates and the "cooling to space" term with and without the Curtis-Godson pressure. They conclude that this approximation to the non-homogeneous pressure is "sufficiently accurate" everywhere except in the 9.6 micron ozone band in the stratosphere which is outside the scope of interest of our calculations and in the water vapor continuum region. Since the continuum component has the effect of reducing the resulting error, it will only be significant near the ground and they therefore state that the Curtis-Godson approximation will be assumed to be adequate under all circumstances.

III-3.4 Line Intensity and Temperature Dependence

The line intensity which enters the calculations in the expression for the Lorentz broadening is dependent on the population densities of the energy states and is therefore a function of temperature. For each water vapor and carbon dioxide line, an intensity has been calculated at 25°K intervals from 150 to 300°K. As discussed in III-4.2 the lines in each subinterval in the quasi random model were divided into intensity decades and the median line intensity per decade determined. This was done for each of the eight temperatures. For each decade and subinterval, both the median line intensity and the number of lines were fitted as functions

of temperature to regression equations. The regression coefficients for the nine water vapor and six carbon dioxide subintervals for each of the five decades are given in appendix B.

Since, as with the pressure, the temperature is not homogeneous over the mass path, a mean temperature is defined as,

$$\overline{T} = \frac{\int T du}{\int du} , \qquad \text{(III-33)}$$

and used to generate the line intensities and numbers of lines from the regression equations.

III-4 ATMOSPHERIC TRANSMISSION BAND MODELS

III-4.1 Introduction

In order to solve the transfer equation exactly it is necessary to know, among other things, the complete line structure within each of the bands under consideration. Yet even if that information is known the computational procedures are still so extensive as to preclude carrying them out. To reduce the number of computations involved various investigators have created models for the line structure by grouping the lines in such ways as to simplify their representation.

Elsasser (1942) developed the periodic model for which there are an infinite number of equally spaced Lorentz lines with uniform intensity and half width. Goody (1952) developed a model again having an infinite number of lines but with random spacing In addition, the line intensities are assumed to be specified by some probability distribution. For reasons which are obvious this model is called the Goody or statistical model.

Both models have been used for various parts of the infrared spectrum. The periodic model suffices for the rather regularly spaced lines associated with the linear molecules such as carbon dioxide, but is too simple a representation to be used for the more irregular lines of the water vapor and ozone bands whose molecules are non linear; the structure of these bands is better represented by the statistical model. Various other models have been developed, although for the most part they are derived from the statistical or periodic band models.

III-4.2 Quasi-Random Band Model

For the vibration-rotation band the most useful model is probably that developed by Wyatt et al. (1962a). This model, the quasi-random model, differs from the others in that it does not assume that the lines are distributed over an infinite interval. Instead the band is divided into a set of finite subintervals each containing a finite number of lines. Within each of these subintervals the finite number of lines are treated as being randomly distributed. It is for this reason that the model is called quasi-random. Within each subinterval the lines are sorted into intensity decades, each decade being represented by a mean line intensity and the number of lines within that decade. The average flux transmission function for a given subinterval and decade due to the lines in that subinterval and decade is then

$$\tau_{\delta}(u_o, u) = \left\{ \frac{1}{\delta} \int_{\delta} e^{-k_{\omega_i}} 1.667 \left| u-u_o \right| d\omega \right\}^{n_i} \qquad \text{(III-34)}$$

where k_{ω_i} is a mean absorption coefficient and n_i the number of lines in the i^{th} decade of subinterval whose width is δ .

Stull et al. (1963) used five decades per subinterval in their transmissivity calculations for water vapor and carbon dioxide. For this study,

preliminary cooling rate calculations, to be discussed in a later section, also indicated that five decades are adequate. Thus the mean transmission over a subinterval is

$$\tau_{\delta}(u_o, u) = \prod_{i=1}^{5} \left\{ \frac{1}{\delta} \int_{\delta} e^{-k\omega_i 1.667 |u-u_o|} \, d\omega \right\}^{n_i} \qquad \text{(III-35)}$$

The contributions to the transmission over one subinterval from lines outside that subinterval whose wings extend into the given subinterval must also be considered. The average transmission is then

$$\tau_{\substack{\delta_1 \\ +\text{wings}}}(u_o, u) = \tau_{\delta_1}(u_o, u) \prod_{k=2}^{\infty} \tau_{\delta_k}(u_o, u) \qquad \text{(III-36)}$$

where δ_1 is the subinterval for which the transmission is being evaluated and δ_k the subintervals containing the lines contributing to the wing contribution.

III-4. 3 Formulation of the Quasi-Random Model for Lorentz Absorption Profiles

The average contribution to the flux transmission function over a subinterval extending from ω_L to $\omega_L + \delta$, due to lines in subinterval δ' becomes, assuming that broadening is only due to molecular interactions (Lorentz broadening),

$$\tau_{\delta}(u_o, u) = \prod_{i=1}^{5} \left\{ \frac{1}{\delta'} \int_{\omega'}^{\omega_L'+\delta'} \exp\left[-S_i \, 1.667 \, |u-u_o| \frac{\alpha_L}{\pi} \frac{1}{(\omega_L + \frac{\delta}{2} - \omega)^2 + \alpha_L^2} \right] d\omega \right\}^{n_i}$$

(III-37)

Although the transmission function is calculated at wavenumber $\omega_L + \frac{\delta}{2}$ (ω_L being the lower wavenumber boundary of the subinterval δ) it is assumed to represent the transmission over the entire subinterval. The integration variable, ω, varies over the subinterval, δ', within which the contributing lines have their centers. This subinterval can coincide with

δ or lie outside it. In the former case the direct contribution to the transmission is being calculated, and in the latter case a wing contribution.

In order to make the equation (III-37) more tractable the following substitutions developed by Wyatt et al. (1962a) are used:

$$z' = (\omega_L + \delta/2) - (\omega_L' + \delta'/2)$$

$$y = \omega - (\omega_L' + \delta'/2)$$

$$\rho = 2\alpha_L/\delta'$$

$$\eta = 2y/\delta'$$

$$\epsilon = 2z'/\delta'$$

$$\xi_i = S_i \, 1.667 |u - u_o| / (\pi \alpha_L)$$

z' represents the difference between the centers of the subintervals δ and δ'. y represents the difference between the center of the line being considered and the center of the subinterval in which the lines are located. (III-37) can then be written as,

$$\tau_\delta(u_o, u) = \prod_{i=1}^{5} \left\{ \frac{1}{2} \int_{-1}^{1} \exp\left[-\frac{\rho^2 \xi_i}{(\epsilon - \eta)^2 + \rho^2} \right] d\eta \right\}^{n_i} \qquad \text{(III-38)}$$

For the direct subinterval $z' = 0$ and the transmission contribution is

$$\tau_{\delta_{k=1}}(u_o, u) = \prod_{i=1}^{5} \left\{ \frac{1}{2} \int_{-1}^{1} \exp\left[-\frac{\rho^2 \xi_i}{\eta^2 + \rho^2} \right] d\eta \right\}^{n_i} \qquad \text{(III-39)}$$

For the wing contributions note that $(\epsilon - \eta)^2 >> \rho^2$. This is true as long as the subintervals are all large compared to the mean half width, which is the case in these calculations; then the transmission contribution for a wing subinterval is,

$$\tau_{\delta_{k \neq 1}}(u_o, u) = \prod_{i=1}^{5} \left\{ \frac{1}{2} \int_{1}^{1} \exp\left[-\frac{\rho^2 \xi_i}{(\epsilon - \eta)^2} \right] d\eta \right\}^{n_i} \qquad \text{(III-40)}$$

The actual significance of the wing contributions will be discussed in the next section.

III-5 NEGLECTING OF WING TRANSMISSION CONTRIBUTIONS

The selection of the wave number subintervals for the water vapor and carbon dioxide bands is discussed in succeeding sections of this chapter. The subinterval sizes were initially chosen to facilitate comparisons with the various experimental results available, and the final subintervals were chosen to minimize the differences between these experimental and our theoretical transmissivities.

From the expression for the wing contribution to the transmission as given by (III-40), one can see that the transmissivity approaches unity as the subinterval size increases. This is simply because, for large subintervals, the contribution within a subinterval due to lines centered in an adjacent but distant subinterval is quite small. In the quasi random band model used here the minimum subinterval size is 55 cm^{-1} (compared to a mean half width of about .06 cm^{-1} NTP) and therefore the contributions to the transmissivity from the wing subintervals are neglected.

III-6 NUMERICAL PROCEDURES USED TO CALCULATE THE TRANSMISSIVITIES

Since the expressions for the transmission functions, fluxes, and cooling rates do not conveniently lend themselves to analytic solutions, various numerical procedures have to be employed to carry out the calculations. (III-39), (III-24), (III-25), and (III-2) comprise the system of equations which is to be solved. The first step in their solution involves the numerical evaluation of the transmission function.

The integral appearing in (III-39) which is equal to the transmissivity due to a single line is divided into two parts as follows,

$$\int_0^1 \exp\left[-\frac{\rho^2 \xi_i}{\eta^2+\rho^2}\right] d\eta = \int_0^{1/2} \exp\left[-\frac{\rho^2 \xi_i}{\eta^2+\rho^2}\right] d\eta + \int_{1/2}^1 \exp\left[-\frac{\rho^2 \xi_i}{\eta^2+\rho^2}\right] d\eta \qquad \text{(III-41)}$$

and each half is evaluated using Simpson's rule,

$$\int_a^b f(x)dx = \frac{b-a}{2}\left\{\frac{1}{3}\left[f(a)+4f(c)+f(b)\right]\right\}$$

where,

$$c = (b+a)/2$$

Each half is again divided and the resulting integrals evaluated as above. This is continued until the sum of the two new integrals differs by less than 10^{-6} from the value of the preceding integral. Such a level of accuracy is required to insure that the final values of the transmissivities are correct to four figures.

Unfortunately, the above technique is a rather lengthy one and therefore costly in terms of computer time. To reduce the time involved the range of values of ξ_i and ρ encountered in the hemispheric calculations of the carbon dioxide and water vapor transmissivities were determined. The transmission integral was then solved for a limited number of values of ξ_i and ρ within the determined ranges. These values were in turn used to form an interpolation table. The interpolation scheme which is used was developed by Wyatt et al. (1962b).

A trial and error process was required to ascertain the sizes of the increments for ξ_i and ρ. Values of the transmissivity were calculated via the interpolation scheme and also directly via the quadrature evaluation of the integral in order to assess the accuracy of the interpolation process. An accuracy of four figures was possible in the interpolated values.

III-7 WATER VAPOR TRANSMISSION PARAMETERS

III-7.1 Introduction

Benedict and Calfee (1967) and Benedict and Kaplan (1964) determined theoretical values for the line centers, half widths, and intensities associated with the water vapor lines located between 0 and 2450 cm^{-1} and it is their results which are used in this work. This portion of the infrared spectrum includes two major water vapor bands; the 80 micron (125 cm^{-1}) pure rotation band and the 6.3 micron (1590 cm^{-1}) vibration-rotation band. The water vapor continuum, centered around 10 microns (1000 cm^{-1}), is also contained within this part of the infrared spectrum.

The spectrum was divided into 25 cm^{-1} intervals and within each of these intervals the line intensities were summed. Since the intensities are a function of temperature, this was done both for 200 and 300^{o}K. The results are presented in Figure (III-1). It is obvious that the temperature dependence will present no problems to the selection of the subintervals and that terminating the lines at 2450 cm^{-1} is quite reasonable.

The subintervals were selected on the basis of this figure with the constraint that they also be chosen in such a fashion as to facilitate comparisons with the available experimental results. The resulting water vapor subintervals are 0-220, 220-440, 440-800, 800-1250, 1250-1420, 1420-1590, 1590-1845, 1845-2100, and 2100-2450 cm^{-1}.

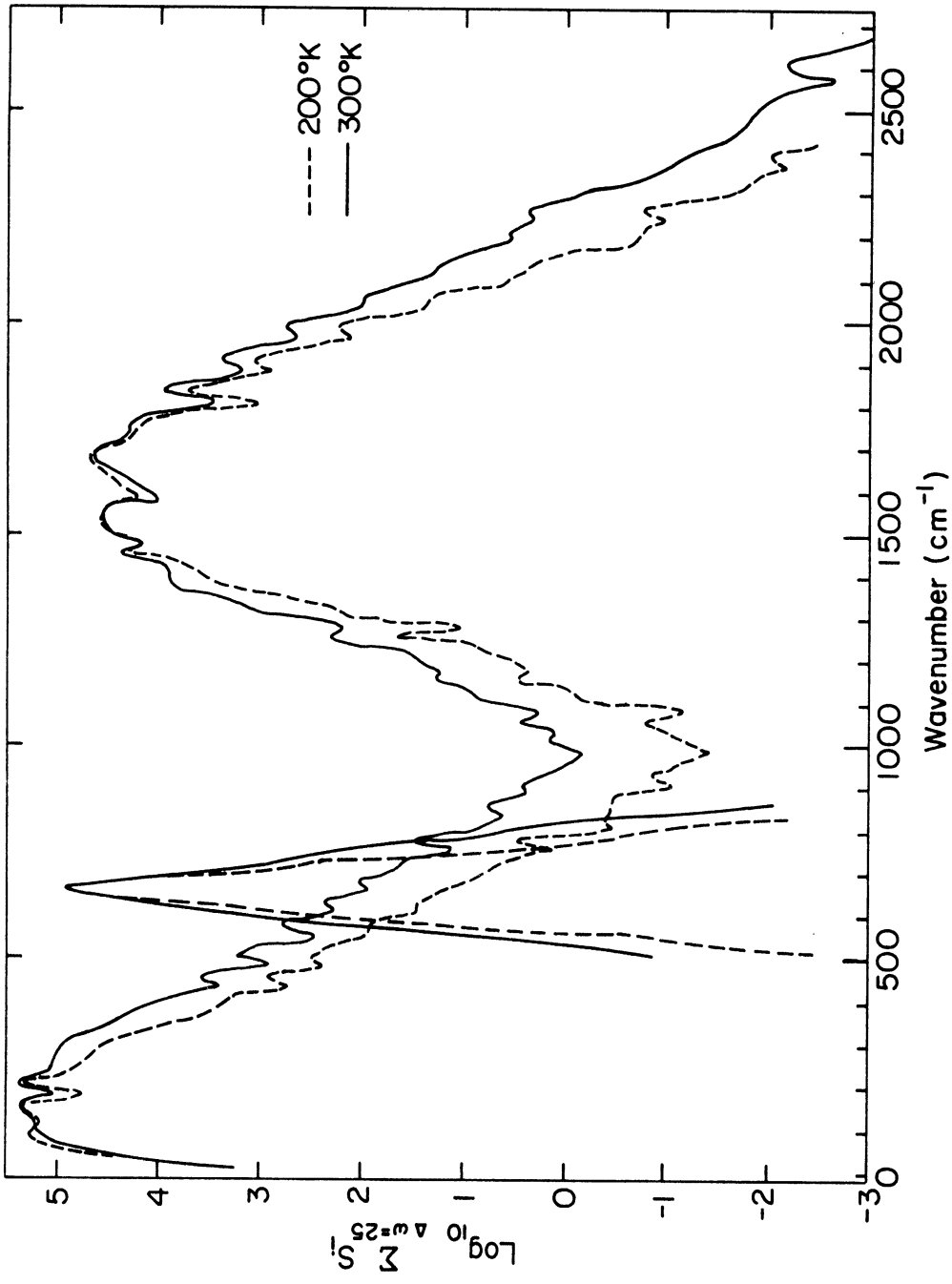

Figure III-1 Comparison of integrated line strengths (25 cm^{-1} intervals) for the infrared bands of carbon dioxide and water vapor at 200K and 300K

A mean half width of .0655 cm^{-1} was calculated from the individual half widths from 0 to 2733.22 cm^{-1}. This value enters into the calculations in the form of α_0 as given in (III-31). It is used both for the 6.3 and 80 micron bands.

III-7.2 6.3 Micron Vibration-Rotation Water Vapor Band

The transmissivities as calculated from the quasi-random band model were compared with the experimental results of Burch et al. (1962) for the total absorption, $A(\omega)d\omega$, where $A(\omega)$ is the observed fractional absorption at wavenumber ω. They estimate that their results have an uncertainty of about $\pm$ 6 to $\pm$ 8 percent for values of the total absorption greater than 50 cm^{-1} and a somewhat greater uncertainty for smaller values of total absorption.

The 6.3 micron band as considered by Burch et al. covers an interval from 1250 to 2100 cm^{-1}, divided into two parts at 1590 cm^{-1}. As calculated in this study the region is divided into four subintervals (1250-1420, 1420-1590, 1590-1845, and 1845-2100 cm^{-1}). Burch et al's experimental results were made for fixed temperatures and pressures. To reproduce the experimental conditions in the present calculations the line intensities were adjusted to agree with the experimental temperatures using the regression scheme discussed elsewhere. In addition the Curtis-Godson pressure was equated to the experimental pressure. With these adaptations of our model, the term $\sum_{i=1}^{4} (1 - \tau_{\delta_i})\delta_i$ was calculated for the four subintervals mentioned above where τ_{δ_i} was defined in (III-39) and δ_i is the width in cm^{-1} of the i^{th} subinterval. Table (III-1) gives the percentage differences between these theoretical results and Burch et al.'s experimental results.

TABLE (III-1)

Percentage differences between theoretical and experimental total absorptions for the 6.3 micron water vapor band relative to the experimental values. (a negative value indicates that the theoretical value is larger)

Mass Path (gm/cm^2) \ Curtis Godson Pressure (mb)	133	330	1013
.002	-30.8	-11.3	- 1.8
.004	- 5.8	1.3	7.2
.010	9.4	6.5	4.8
.020	8.2	7.3	0.0
.040	9.0	5.3	- 2.6
.100	1.1	- 6.6	- 6.5
.200	- 3.7	- 7.8	-10.5
.400	- 6.0	- 9.3	- 7.5
.800	- 4.0	- 5.7	- 8.4
.999	- 4.2	- 2.8	- 5.3

Although the theroetical values differ in some cases from the experimental values by more than the estimated experimental uncertainty, in general the agreement between the two sets of values is good. In that part of the table where the differences are greatest - for low pressures and mass paths - the total absorptions drop to their lowest values and Burch et al. anticipate their largest experimental uncertainty. There does not appear to be any identifiable trend in the way in which the two total absorptions differ.

Rodgers and Walshaw (1966) have developed an expression for the mean transmission based on Goody's random model. Using their line parameters and expression, we calculated values of the total absorption for the 6.3 micron water vapor band. It should be anticipated that these values will be somewhat larger than either those of Burch et al. or those in this study because the band, as viewed by Rodgers and Walshaw, extends from 1200 to 2200 cm^{-1}. Tables (III-2) and (III-3) compare Rodgers and Walshaw's, Burch et al.'s, and our total absorptions.

Except for the very small mass paths, as anticipated, Rodgers and Walshaw's total absorptions are somewhat larger than either ours or those of Burch et al.. For the mass paths and pressures for which the greatest differences arose in Table (III-1) there is not the same large disagreement in Table (III-2) between Rodgers and Walshaw's and our results. It should be noted that the differences between the results of Rodgers and Walshaw and Burch et al. are of the same magnitude as the differences between our results and those of either Burch et al. or Rodgers and Walshaw.

TABLE (III-2)

Percentage differences between the present calculations and Rodgers and Walshaw's total absorptions for the 6.3 micron water vapor band relative to Rodgers and Walshaw (a negative value indicates that our value is larger)

Mass Path (gm/cm^2) \ Curtis-Godson Pressure (mb)	133	330	1013
.002	- 6.2	0.0	- 5.6
.004	2.7	4.4	4.8
.010	8.3	9.3	6.0
.020	9.8	9.7	4.5
.040	8.9	6.5	4.8
.100	7.2	4.1	1.2
.200	4.9	2.3	0.2
.400	2.2	0.6	1.4
.800	1.3	0.7	2.3
1.0	1.1	0.8	2.6
1.5	0.7	1.4	3.8
2.0		1.9	4.8
2.5		2.5	5.7
3.0		2.9	6.6
3.5		3.2	7.1
4.0		3.6	7.7
4.5		4.1	8.0
5.0			8.4
5.5			8.8

TABLE (III-3)

Percentage differences between the total absorption of Burch et al. and Rodgers and Walshaw relative to the values of Burch et al. (a negative value indicates that Rodgers and Walshaw's value is larger)

Mass Path (gm/cm^2) \ Curtis-Godson Pressure (mb)	133	330	1013
.002	-23.1	-13.0	3.0
.004	- 8.7	- 3.2	2.6
.010	1.2	- 3.0	- 1.5
.020	- 1.8	- 2.7	- 4.8
.040	0.0	- 1.3	- 7.7
.100	- 6.6	-11.1	- 7.7
.200	- 8.6	-10.4	-11.1
.400	- 8.4	- 8.6	- 9.0
.800	- 5.3	- 6.5	-10.9
1.0	- 5.3	- 4.6	- 8.1

III-7.3 80 Micron Pure Rotation Water Vapor Band

Burch et al. have not included the 80 micron pure rotation water vapor band in their experimental study of infrared absorption. However Palmer (1960) has experimentally determined transmission values for a part of this region of the water vapor spectrum and his values were compared to our theoretical calculations.

The 80 micron band was divided into three subintervals (0-220, 220-440, and 440-800 cm^{-1}) for our quasi-random model. Palmer, on the other hand, examined the region from 200 to 500 cm^{-1}, forming averages from his measured values of the percentage of transmission for the intervals 250-300, 290-340, 320-370, and 360-410 cm^{-1}. These are expressed as functions of the logarithm of the product of the pressure (atmospheres) and the amount (gm/cm^{2}) of water vapor. Average values of the transmissivity were calculated for the subinterval from 220 to 440 cm^{-1}. Figs. (III-2) and (III-3) compare Palmer's curves for the intervals from 290 to 340 cm^{-1} and 320 to 370 cm^{-1} with our results. The agreement is excellent over the range of values used but our calculations were not made for as large a range of values of water vapor and pressure as were Palmer's. However in the comparison between experimental and theoretical values for the 6.3 micron band of water vapor it was found that the accuracy increases as the mass path and pressure increase and that the accuracy was lowest for the smaller values of these two parameters. Thus it is reasonable to assume that the accuracy indicated here for the larger negative values of the logarithm of the product of the mass path and pressure will hold, and probably improve, for smaller negative values.

III-7.4 Water Vapor Continuum

It has been concluded that for the subintervals used in this work it is not necessary to calculate the wing contributions to the water vapor and carbon dioxide transmissivities. It seems advisable however to re-examine this conclusion for that part of the water vapor spectrum known as the continuum. This is the region of the infrared spectrum which ranges from approximately 800 to 1250 cm^{-1}, excluding the 9.6 micron ozone

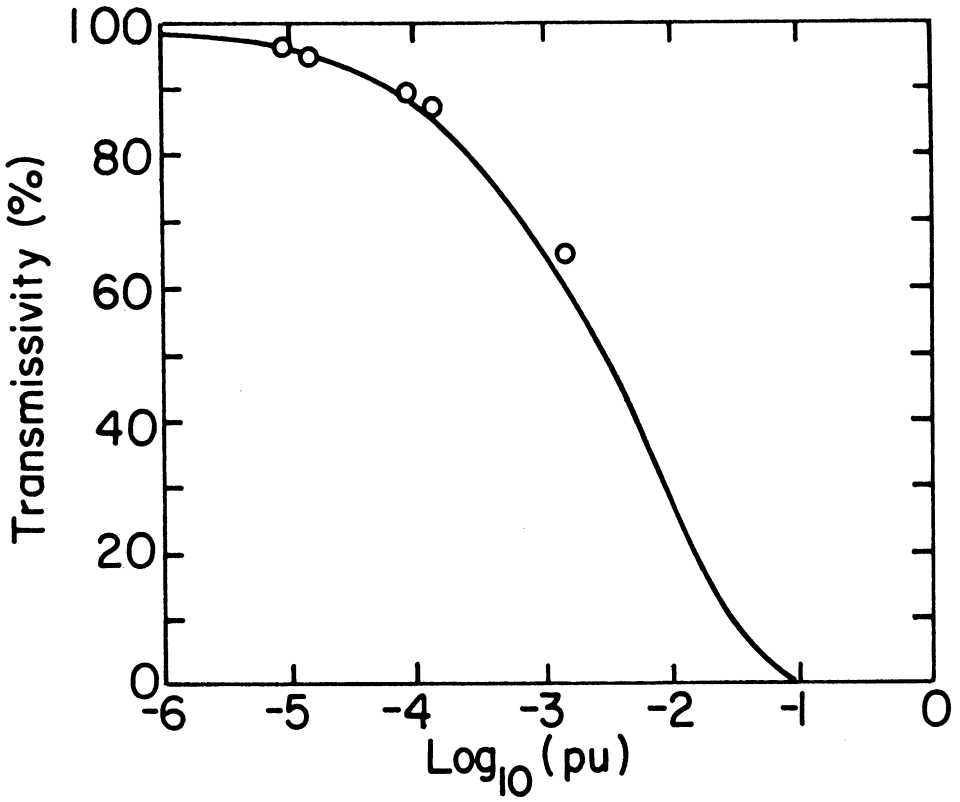

Figure III-2 A comparison of Palmer's (290 - 340 cm^{-1}) and the quasi-random transmissivities (220 - 440 cm^{-1}) for water vapor

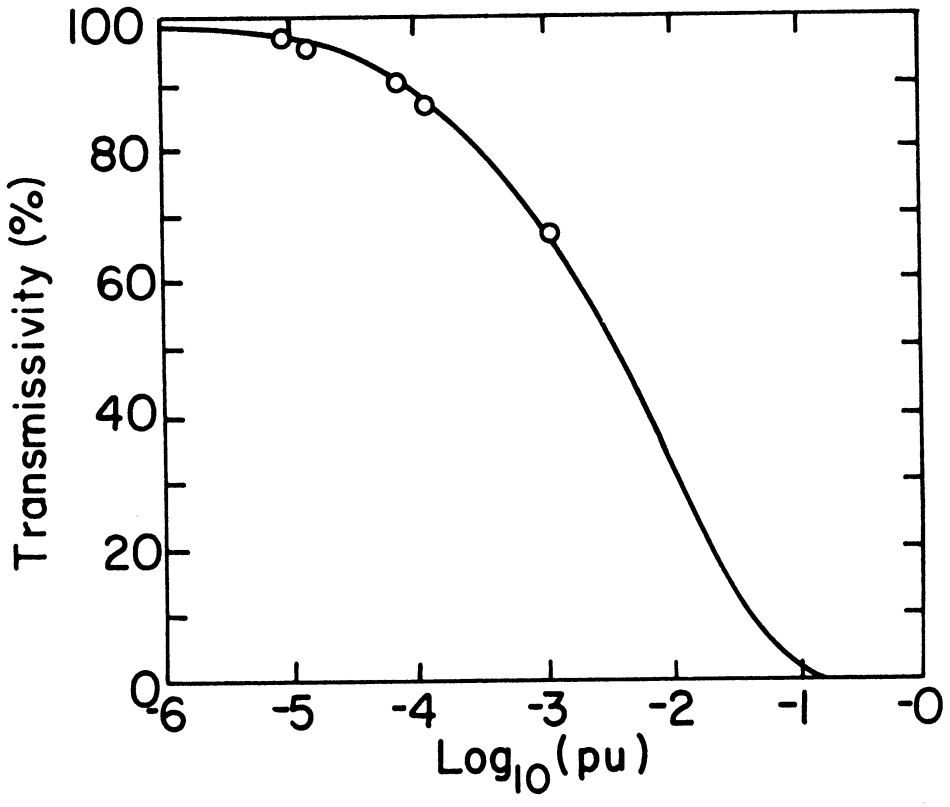

Figure III-3 A comparison of Palmer's (320 - 370 cm^{-1}) and the quasi-random transmissivities for water vapor

band in which the lines are quite weak. It is therefore possible that those lines whose centers lie outside this "window region" may still have appreciable intensities in those parts of their wings reaching into the continuum region, appreciable at least in comparison to the lines originating within the continuum. Also the energies available at these wave numbers for terrestrial temperatures are considerable; for instance at a radiating temperature of 250°K there are approximately 39 ergs/cm^2/cm^{-1}/solid angle/sec. (The peak energy at this temperature is about 89 ergs/cm^2/cm^{-1}/solid angle/sec.).

Transmissivities were computed for an atmospheric profile typical of climatological conditions at 35°N for April with no clouds present, atmospheric parameters being taken from London (1957). The wing contributions to the continuum region from all the subintervals between 0 and 2450 cm^{-1} were included. The radiative flux divergences, to the nearest erg cm^{-2} sec^{-1}, were all zero and therefore it is reasonable, even within the window region to neglect the wing contributions.

Fig. (III-4) gives the cooling rate profile generated by the lines within the continuum and also the profile produced when all the water vapor lines between 0 and 2450 cm^{-1} are considered. Both profiles show a maximum cooling level at 684 mb, the cooling from the window region comprising approximately 11% of the total cooling. These profiles and those resulting from the other subintervals are discussed further in Section III-10

III-8 CARBON DIOXIDE TRANSMISSION PARAMETERS

Line intensities and positions are available (Drayson, 1970) for the 15 micron carbon dioxide band from 503.71 cm^{-1} to 860.81 cm^{-1} with line intensities (cm^{-1}/atm cm) given every 25°K from 175°K to

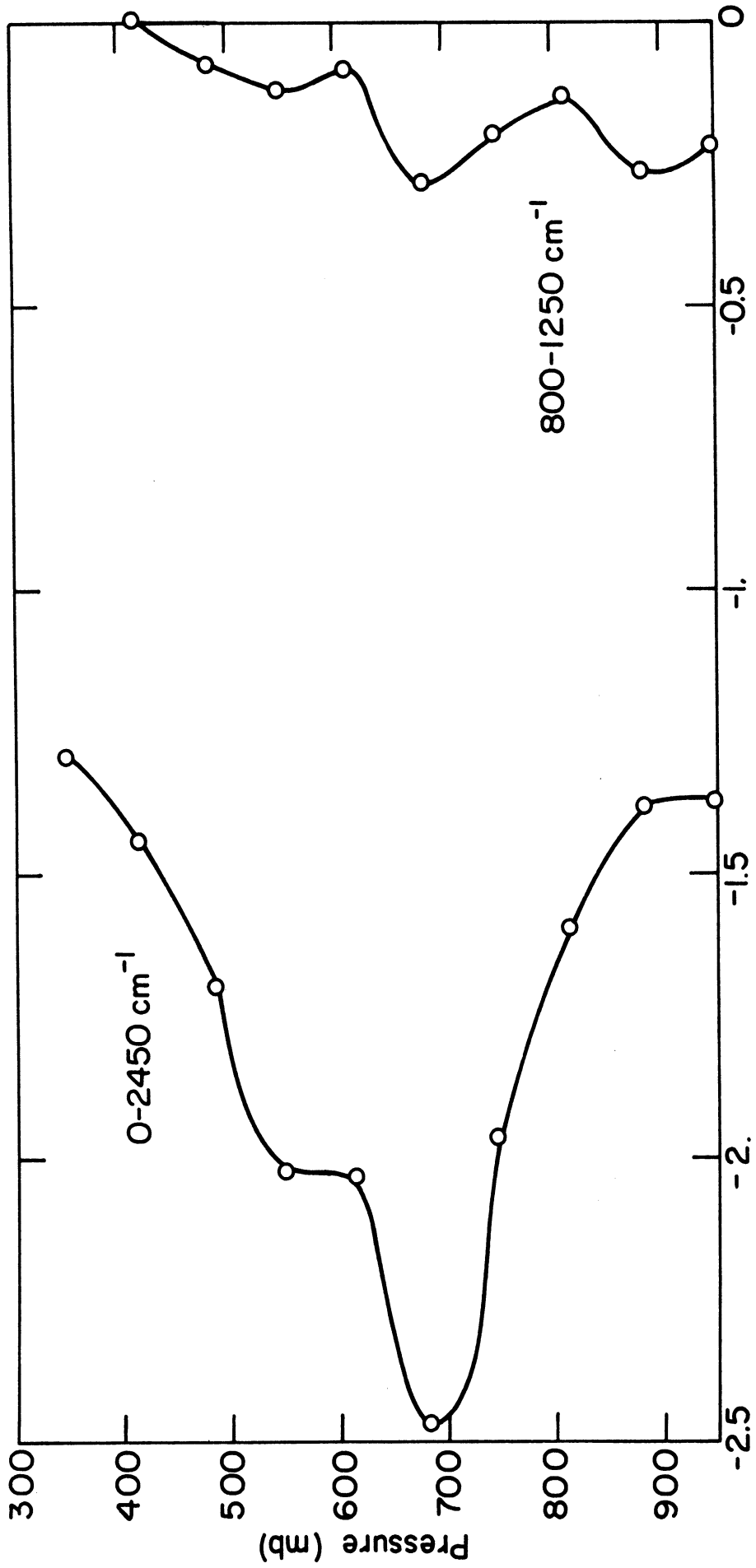

Figure III-4 Comparison of rates of temperature change due to water vapor over 0-2450 cm^{-1} interval. Profile for 35°N latitude, April, with no clouds present

300^{o}K. As was done for the water vapor bands, the carbon dioxide lines were divided into 25 cm^{-1} intervals and the line intensities summed within each interval. The results are pictured in Figure (III-1). The most noticeable characteristic of this band is its very sharp peak with the rapid decrease in intensity away from the center of the band. Although both of the water vapor bands have approximately the same peak values of summed intensities, the band strengths of both are greater than for the 15 micron band.

In order to determine into how many subintervals the band should be divided, and simultaneously to determine the accuracy of the calculation techniques, the experimental results provided by Burch et al. (1962) for fractional and total absorption in the 15 micron carbon dioxide band were utilized. Sample calculations for various pressures and carbon dioxide mass paths which are representative of the atmosphere and used by Burch et al. were carried out.

The band was subdivided into two, four and six subintervals. In addition, calculations were carried out both when the Q branch was isolated and treated spearately and when it was included within one of the subintervals. The division into six subintervals was required before the theoretical results agreed, within the limits of the experimental error, with those of Burch et al.. The isolation of the lines of the Q branch did improve the results slightly and therefore it was treated separately

Since the half widths were not given for the 15 micron carbon dioxide lines, the fractional and total absorption calculations were made for estimates of the half width equal to .06, .07, and .08 cm^{-1}. The best agreement with the absorption values of Burch et al. was for a value of .06 cm^{-1}.

Table (III-4) compares the fractional and total absorptions of Burch et al. with the values calculated here when the band was divided into the six subintervals and the Q branch. Since experimental values are not given for all of the subintervals used in this study, comparison could only be made for those from 545 to 617, 617 to 667, and 667 to 720 cm^{-1}. The estimated uncertainty for the experimentally determined total abosrptions is $\pm$ 5% for the values considered here. For the fractional absorption it is less than $\pm$ 5% for values greater than 0.10 and is as high as $\pm$ 20% for values less than 0.10. Most of the percentage differences fall within the range of experimental error. Those cases in which the range is exceeded all have relatively small mass paths and only occur infrequently in the actual calculations. The uncertainties in the fractional absorption are entirely acceptable in the two subintervals covering the wave number range from 617 to 720 cm^{-1}. For the subinterval from 545 to 617 cm^{-1} some of the smaller mass paths yield percentage differences in excess of 5%. However these results occur for values of the fractional absorption between .1 and .3 cm^{-1} and, as noted earlier, the experimental error will be relatively high in such cases.

TABLE (III-4)

Percentage differences between theoretical and experimental values of fractional and total absorptions for the 15 micron carbon dioxide band relative to the experimental values (a negative value indicates that the theoretical value is larger)

Mass Path gm/cm^2	Pressure mb	Total Absorption-Percentage Differences	Fractional Absorption-Percentage Differences $545\text{-}617cm^{-1}$	$617\text{-}667cm^{-1}$	$667\text{-}720cm^{-1}$
.046	1016	-7.1	13.9	1.0	-4.5
.091	405	-8.5	1.0	1.6	-3.9
.091	1019	-6.4	12.9	-2.5	-4.0
.190	411	-5.5	8.2	-1.0	-1.3
.190	1024	-4.7	0.7	-1.1	-0.1
.234	439	-5.8	3.0	-2.4	-1.2
.379	292	-2.7	0.3	0.0	-0.9
.379	3	-2.9	-1.1	-0.6	-1.0
.379	1007	-2.3	-2.4	0.0	0.0
.383	700	-3.3	4.3	-0.3	0.0

On the basis of these results the 15 micron carbon dioxide band was divided as indicated in Table (III-5).

TABLE (III-5)

Subinterval divisions used

for the 15 micron carbon dioxide band

Designation	Subinterval Limits (cm^{-1})
1st	500-555
2nd	555-610
3rd	610-667
Q	667-668
4th	668-720
5th	720-775
6th	775-862

(Appendix D contains the subintervals after the individual water vapor, carbon dioxide, and ozone intervals were combined for the flux calculations.)

The transmission functions for the Q branch could not be calculated from the interpolation scheme because of the small subinterval width but rather were calculated from the original equations (those used to generate the interpolation table). Sample calculations show that, because the Q branch contains such strong lines, the atmosphere is effectively opaque for wave numbers within this region. Since an opaque atmosphere yields no flux divergence, contributions to the cooling rates from the Q branch were not calculated for the hemispheric computations.

III-9 OZONE TRANSMISSION PARAMETERS

Walshaw (1957) has carried out laboratory measurements of the absorption in the 9.6 micron ozone band. These measurements were fitted to an empirical formula of the form,

$$A_r = \Delta\omega\left[1 - 10^{-\mu f(\phi)}\right] \qquad \text{(III-42)}$$

where A_r is the total absorption, $\Delta\omega$ the wave number range of the band (138 cm^{-1}), $\mu = m\zeta$, and $\phi = m\zeta^a/p$; a is equal to 2.11 and ζ (m) is a function of m, the amount of ozone present. The expression for the transmissivity averaged over the ozone band is then given by

$$\tau = 10^{-\mu f(\phi)} \qquad \text{(III-43)}$$

and was used in the present calculations. Values of the various parameters are given by Walshaw. As an estimate of the overall error resulting from the experimental errors and the fitting of the data to the total absorption formula, Walshaw gives a value of 2.4%.

III-10 WATER VAPOR COOLING RATES AS A FUNCTION OF SUBINTERVAL

Since water vapor is the primary contributor to radiative cooling in the troposphere, a sample calculation was made for clear skies for climatological conditions in April at 35° N as determined by London (1957). This calculation, which was made for the water vapor bands between 0 and 2450 cm^{-1}, serves two purposes. It allows us to ascertain how much each subinterval contributes to the overall water vapor cooling rate profile (since it is relatively time consuming to calculate the cooling rates for each subinterval in the hemispheric calculations, only the overall cooling rates were calculated), and also to determine into how many layers the atmosphere should be divided to optimize the calculations in terms of accuracy and computer time. This final consideration is discussed in Appendix E.

Table (III-6) gives the percentage contributions from each of the nine subintervals to the overall cooling rates for various atmospheric levels. These results indicate that insofar as the water vapor spectrum is concerned the largest contributions come from the 80 micron band. At tropospheric temperatures, the energy associated with the center of the 80 micron band is over six times greater than that at the center of the 6.3 micron band (for a temperature of 250^{o}K). Thus although there are fewer lines in the 80 micron band, the energy available is considerably greater in this part of the infrared spectrum and it is for this reason that the 80 micron band contributes as strongly as it does to the cooling rates. The same reasoning also holds for the relatively large contribution from the window region (800-1250 cm^{-1}).

It should be recognized that these results cannot be considered to hold for the entire infrared spectrum since neither the 9.6 micron ozone band nor the 15 micron carbon dioxide band has been included, the latter of which will reduce the contribution from the rotational band. Also note that although the water vapor lines as given by Benedict and Calfee (1967) extend beyond 2450 cm^{-1}, the contributions in the subinterval from 2100 to 2450 cm^{-1} are so small that there is no need to include additional subintervals beyond 2450 cm^{-1}.

TABLE (III-6)

Percentage contributions to the overall water vapor cooling rates from each of the nine subintervals

Pressure (mb) \ Subinterval (cm^{-1})	0-220	220-440	440-800	800-1250	1250-1420	1420-1590	1590-1845	1845-2100	2100-2450
950	0.0	0.0	77.0	15.1	4.9	0.2	0.2	2.5	0.2
884	0.0	0.0	74.7	19.0	4.6	0.0	0.1	1.5	0.1
817	0.0	0.2	82.5	8.3	6.8	0.1	0.2	1.6	0.1
750	0.0	0.2	79.4	10.3	8.2	0.1	0.3	1.5	0.1
684	0.0	1.5	74.4	11.4	9.5	0.8	1.1	1.3	0.5
617	0.0	12.1	71.0	4.0	8.9	1.7	1.6	0.8	0.0
550	0.3	23.8	55.0	6.0	8.1	3.2	2.8	0.6	0.0
484	2.7	44.7	37.2	4.5	4.3	3.9	2.5	0.3	0.0
417	7.2	56.1	29.3	0.7	2.5	3.3	2.1	0.0	0.0
350	13.2	66.0	15.9	2.9	0.4	1.5	0.1	0.1	0.0
284	22.6	62.5	9.9	1.9	1.1	1.4	0.6	0.0	0.0

Figure (III-5) presents the cooling rate profile summed over the nine water vapor subintervals for three, four, and five line strength decades. None of the profiles differ by more than $0.2^{o}C$ per day and the profiles for four and five decades are essentially the same, differing by less than $0.1^{o}C$ per day except near 900mb where the profiles for three and four decades have equal cooling rates and the five decade profile is about $0.2^{o}C$ per day lower. While a comparison of these three profiles does not completely confirm the adequacy of using five intensity decades, nevertheless this appears to be a reasonable conclusion.

III-11 MULTILEVEL CLOUD MODEL

It is evident that some cloud types occur simultaneously and overlap, while other types will not. When the physical conditions and mechanisms which control the development of the clouds are similar, the probability of overlapping is great. For instance, altostratus are frequently found overlying nimbostratus, both resulting from the widespread lifiting occuring along a warm front. On the other hand cumulonimbus clouds produced by strong convective activity are unlikely to occur and overlap with stratus clouds resulting from the large scale ascent over a frontal system. Unfortunately no studies as to the degree and frequency with which overlap occurs have yet been carried out. Nor have any models been developed to describe the overlapping, although every study has had to make some estimates as to cloud heights and thicknesses which specifically excludes overlap of various cloud types.

In this study no restrictions are imposed on the overlapping of the different cloud types aside from those imposed by their height distributions. Otherwise any two cloud types can overlap and in the absence of information as to how probable their overlapping is, we shall assume,

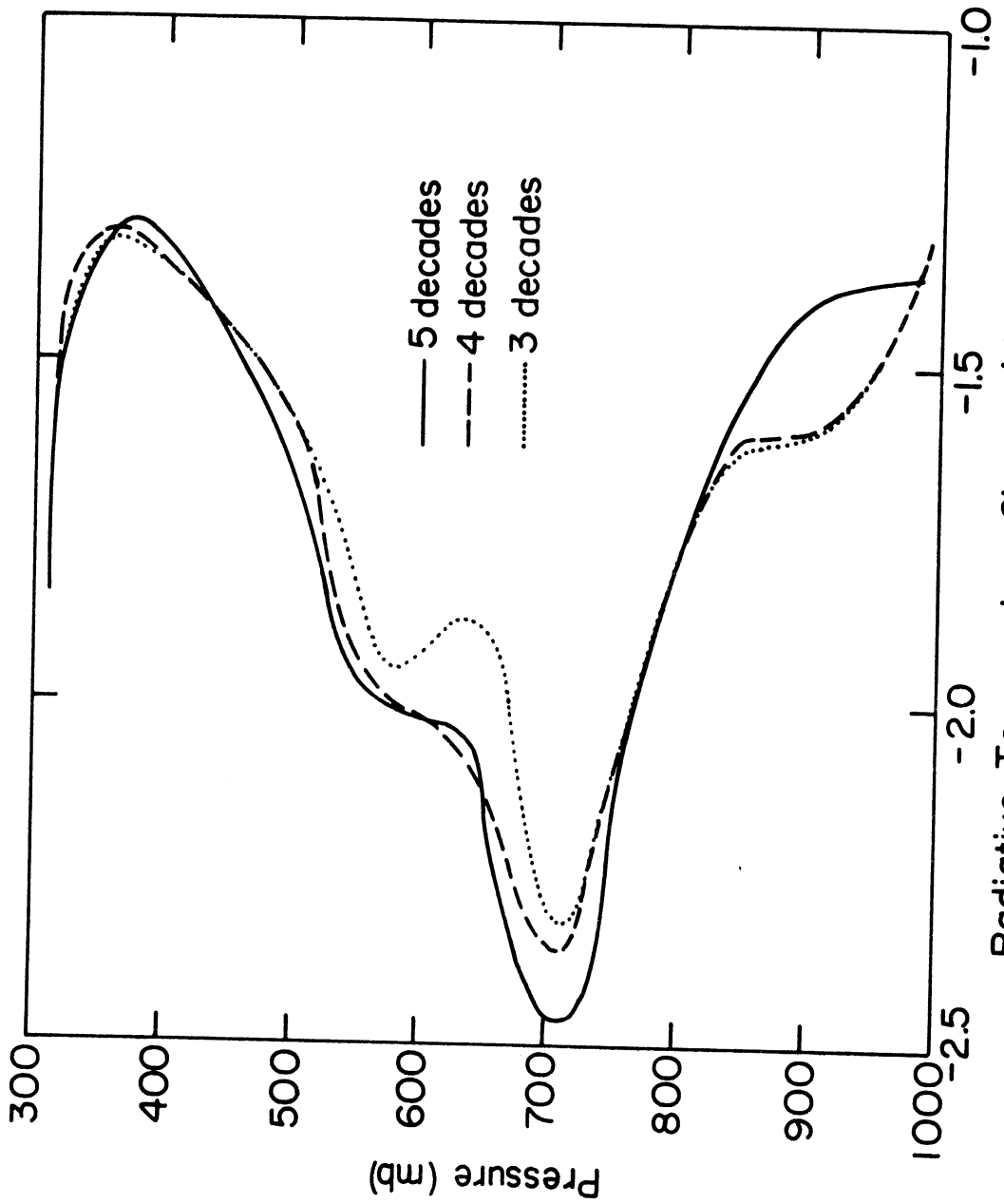

Figure III-5 Water vapor cooling rate profiles for 0-2450 cm^{-1} with 3, 4, and 5 line strength decades per subinterval

as did Manabe and Strickler (1964), that the fractional amount of sky covered by the overlapping clouds equals the product of the fractional covers of the individual types. Essentially we are assuming that the various cloud layers are randomly distributed in the horizontal.

Since there is no systematic information as to how the cloud heights vary longitudinally, it is only possible to characterize the sky conditions and calculate the fluxes for 18 sky situations (two seasons at nine latitudes). Fortunately many of these 18 situations do not significantly differ from each other. Within the calculation then the appropriate form of the expression weighting the flux contributions is selected on the basis of an examination, carried out by the computer, of the cloud cover representative of the given latitude, longitude, and season. The calculation itself assumes a random distribution of the clouds present except that clouds which occupy the same layer cannot overlap.

CHAPTER IV

THE CLIMATOLOGICAL DISTRIBUTIONS OF INFRARED RADIATIVE FLUXES AND HEATING AND COOLING RATES OVER THE SOUTHERN HEMISPHERE

IV-1 OUTGOING INFRARED FLUXES AT THE TOP OF THE ATMOSPHERE

Zonal averages[1] of the outgoing infrared flux at the top of the atmospheric model were determined by adding to the flux values from the present calculations (which extend to 137.5 mb), the stratospheric contributions as given by London (1957) (see Appendix F); these calculations were made for the Northern Hemisphere, but should be applicable to our Southern Hemisphere results since one would not expect much of a variation in stratospheric temperature and water vapor content between the two hemispheres. This annual mean meridional distribution of the outward flux is given in Figure (IV-1) along with the calculated values of Sasamori et al (1971) and Sellers (1966), and the satellite observations as summarized by VonderHaar and Suomi (1971).

Each curve except Sellers's shows a slight increase in the outgoing flux from the equator to about 15°S. Thereafter they all indicate that the flux decreases with increasing latitude as would be expected given the decrease in temperature which occurs toward the pole. Water vapor also decreases substantially poleward but this will tend to decrease the outgoing flux near the equator and increase it toward the pole.[2] The slight peak seen at 15°-25°S results from a decrease at this latitude of the total cloudiness and, in particular, the cirrus cover. Table IV-1 gives the meridional variation of cirrus cover.

---

[1] These averages are formed from a grid of values calculated at latitudinal intervals of 10° and longitudinal intervals of 10° from 5° to 55°, of 20° from 65° to 75°, and of 40° at 85° S.

[2] Longitudinally averaged values of the atmospheric parameters are given in Appendix A for January and July.

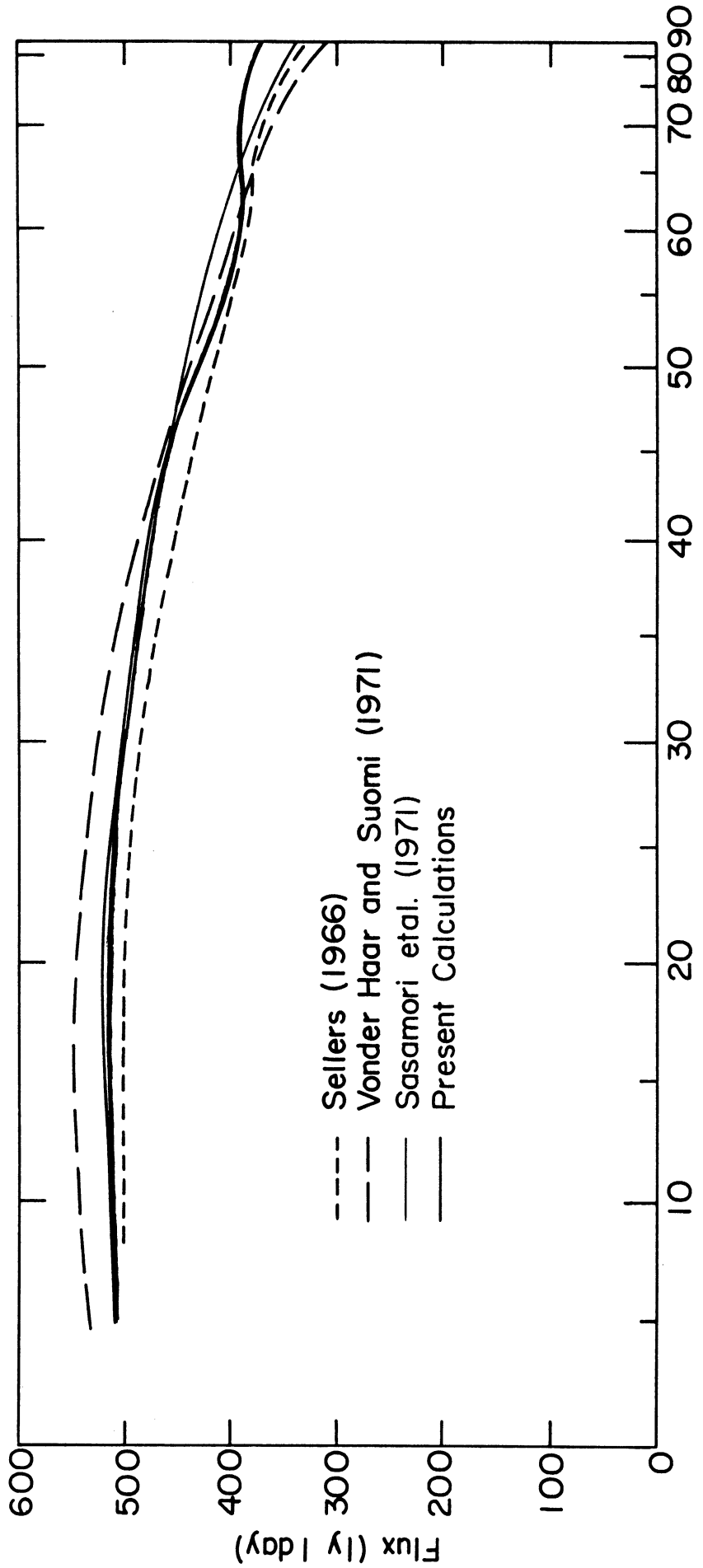

Figure IV-1 Comparisons of calculations and observations of outgoing infrared flux at the top of the atmosphere

TABLE (IV-1)

Cirrus cover (percent of total sky) zonally averaged

Month \ Latitude S	5°	15°	25°	35°	45°	55°	65°	75°	85°
January	25	23	21	24	31	50	48	24	17
July	20	17	18	23	29	41	37	13	8

In the region around 15° -25°S in which the cirrus cover is small the effective height at which the outgoing radiative flux is emitted will drop to warmer levels thereby increasing the flux escaping to space.

The present calculations and those of Sasamori et al. are in excellent agreement to latitudes of about 45°S; however, from 45 to 55°S, and 65 to 90°S, our values are somewhat lower and higher respectively. These differences result in part at least from differing treatments of the clouds. Both studies utilize Telegadas and London (1954) correction to take into account the underestimation of the middle and upper cloud covers. However, in addition, Sasamori et al. reduce the cloud amounts by a constant normalizing factor, forcing the sum of the corrected amounts to equal the total cover. This also has the effect of treating the flux calculations as if there is no overlapping of clouds. Thus radiation originating in one cloud layer is not intercepted by any other cloud layers. Both the reduced amounts of cloud cover and the absence of any overlapping will lower the effective level of origin of the outgoing flux at the top of the atmosphere and thereby increase its value.

In Table (IV-2) the cloud amounts as used in this study at 55 and 75°S are compared with those of Sasamori et al. and with those that would result from applying a normalizing factor of the sort used by Sasamori et al. to the present cloud amounts.

TABLE (IV 2)

Comparison of the cloud covers (percent of total sky) as used by the present study, Sasamori et al., and as would result using a normalizing factor on the present covers for 55 and 75°S

January

	55°S			75°S		
Type	Present Study	Normalized	Sasamori et al.	Present Study	Normalized	Sasamori et al.
Ci	50	33	18.5	24	20	15
As	17	11	8.5	11	9	17.5
Low	29	19	13/12.5*	20	16.5	4/8.5*
St	24	16	22.	18	15	16.5
Cb	4	2.6	4	1	0.8	1

July

	55°S			75°S		
Type	Present Study	Normalized	Sasamori et al.	Present Study	Normalized	Sasamori et al.
Ci	41	27.5	13.5	13	11.5	7
As	16	10.5	6	9	8	10
Low	32	20.5	13/18.5*	17	15	4/14.5*
St	23	15.5	20.5	13	11.5	12.5
Cb	3	2	5	0	0	3

*Sasamori et al. break type 3 clouds into two separate types, Cu and Ns.

It isn't possible to carry out any sort of reliable comparison for the low clouds since Sasamori et al. have divided them into two separate catagories. In any case as far as the outgoing flux at the top of the atmospheric model is concerned the highest clouds, Ci and As,

are most important. At 55°S our cirrus cover when normalized is still approximately twice as great as Sasamori et al.'s. The As cover is also greater but not to the same extent. These differences cause the effective height at which our outgoing radiative flux is emitted to be greater than that of Sasamori et al., accounting for much of the difference between the two calculations.

At 75°S our normalized cirrus covers are again larger but the differences are about a third of what they were at 55°S. For the As amounts however Sasamori et al.'s are larger than those of the present study in both January and July, being about 50% larger in January. This accounts for the fact that our flux value is now greater than that of Sasamori et al. These differences in the high cloud cover are even more pronounced at 85°S where our flux value is again the larger of the two.

The present calculations and those of Sellers show a dip from about 50 to 65°S. This region (polar front) coincides with the zone of maximum total cloudiness, as well as cirrus cover (see Table IV-1). This zone of greater cirrus cover increases the effective height at which the outgoing radiation is emitted, thereby reducing the value of the flux. These are also the latitudes at which the globe is entirely circled by water, a fact which is reflected in the sharp decrease in the zonally averaged water vapor content of the atmosphere poleward of 65°S. At 65°S there are 0.62 gm per cm^2 in January and 0.30 gm per cm^2 in July while at 75°S the values are 0.14 and 0.08 per cm^2. This factor alone would cause an increase in the outgoing flux from 65 to 75°S and it is quite probable that this influence is seen in the rather flat distribution around 70°S.

The disagreement with satellite measurements should not be attributed entirely to inaccuracies in the various theoretical flux models. Problems in satellite calibration contribute some uncertainty to those results. Also the satellite observations represent measurements made over 39 months while the theoretical calculations are based on atmospheric parameters averaged over much more extended periods. Nor do different satellite observations agree. Winston (1966) reports satellite measurements of outgoing infrared flux down to about 55°S which are twenty to forty ly day^{-1} lower and in closer agreement with the calculated fluxes than those reported by Vonder Haar and Suomi. Additional observations made by Tiros VII and reported by Rasool and Prabhakara (1966) for the same latitudes as above show greater agreement with Winston's than with Vonder Haar and Suomi's values.

Rasool and Prabhakara give the outgoing flux at the top of the atmosphere as a function of season as well as latitude. These values indicate that from the equator to 25°S the outgoing flux is greater in July but that thereafter the maximum value at each latitude occurs in January. Our calculations and those of Sasamori et al show a similar result. An examination of the cirrus cover would suggest that the outgoing flux should be greater at all latitudes in July although the differences should not be great from 25 to 45°S and should only become pronounced poleward of 45°S. The reason for the reversal can be seen if the zonally averaged temperatures are examined. Near the equator the vertical temperature profiles for January and July are within 2 to 3°C of each other. Beyond 20°S however the January profiles become significantly warmer and it is this change which is reflected in the flux reversal, the temperature effects becoming more important than the cloud cover.

The decrease in outgoing flux from equator to pole is, in general, greater in the winter (July) than in the summer (January). This is because the horizontal temperature gradient from equator to pole within the troposphere is at least 10^{o}C greater in the winter than in the summer. In January there is an increase in the outgoing flux from about 65^{o} to 75^{o} S. This increase is caused by the reversal of the horizontal temperature gradient in the upper levels of the atmosphere, the temperature increasing continuously from equator to pole in January at the 137.5 mb level. The same reversal of the gradient also occurs in July but does not extend poleward of 45^{o}S. It should be noted that near the pole the cirrus cover is smaller in July (8%) than in January (17%) which would, in itself, suggest that the outgoing flux should be larger in July. However since the cirrus cover is quite small in both months, the influence of the temperature variation outweighs the influence of the cloud cover.

Hemispheric maps of the calculated outgoing flux at the 137.5 mb level have been prepared for January and July and are presented in Figures (IV-2) and (IV-3). The patterns are primarily a function of the meridional variations of temperature and cloud cover already discussed and the longtitudinal distributions of land and water. As can be seen from Figures (IV-4) and (IV-5), which give the distributions of total cloudiness for the southern hemisphere for January and July, the cover in general decreases over land. The same pattern is evident in Figures (IV-2) and (IV-3) in which the outgoing flux generally increases over land. This is particularly true over Australia but can also be seen over South America and Africa. The narrow portion of South America reaching toward the pole and the Palmer Peninsula extending northward from Antarctica toward South America show clearly in the January flux map.

A rather regular zonal pattern is maintained from the polar regions to about 35^{o}S. North of this latitude, longitudinal variations begin to appear. This is mirrored in the total cloudiness maps. Africa, South America and Australia are evident on both the flux maps as regions of increased flux and on the cloud cover maps as regions of relatively clear skies. This is more noticeable in July when the decrease in cloudiness from water to land is more pronounced.

The normally observed zonal increase in the outgoing flux from water to land does not appear in January near the equator. Instead, over Indonesia and equatorial and tropical Africa and South America the outgoing flux is less than over the adjacent oceans. The reason for this becomes clear when the total cloud cover in January for the hemisphere

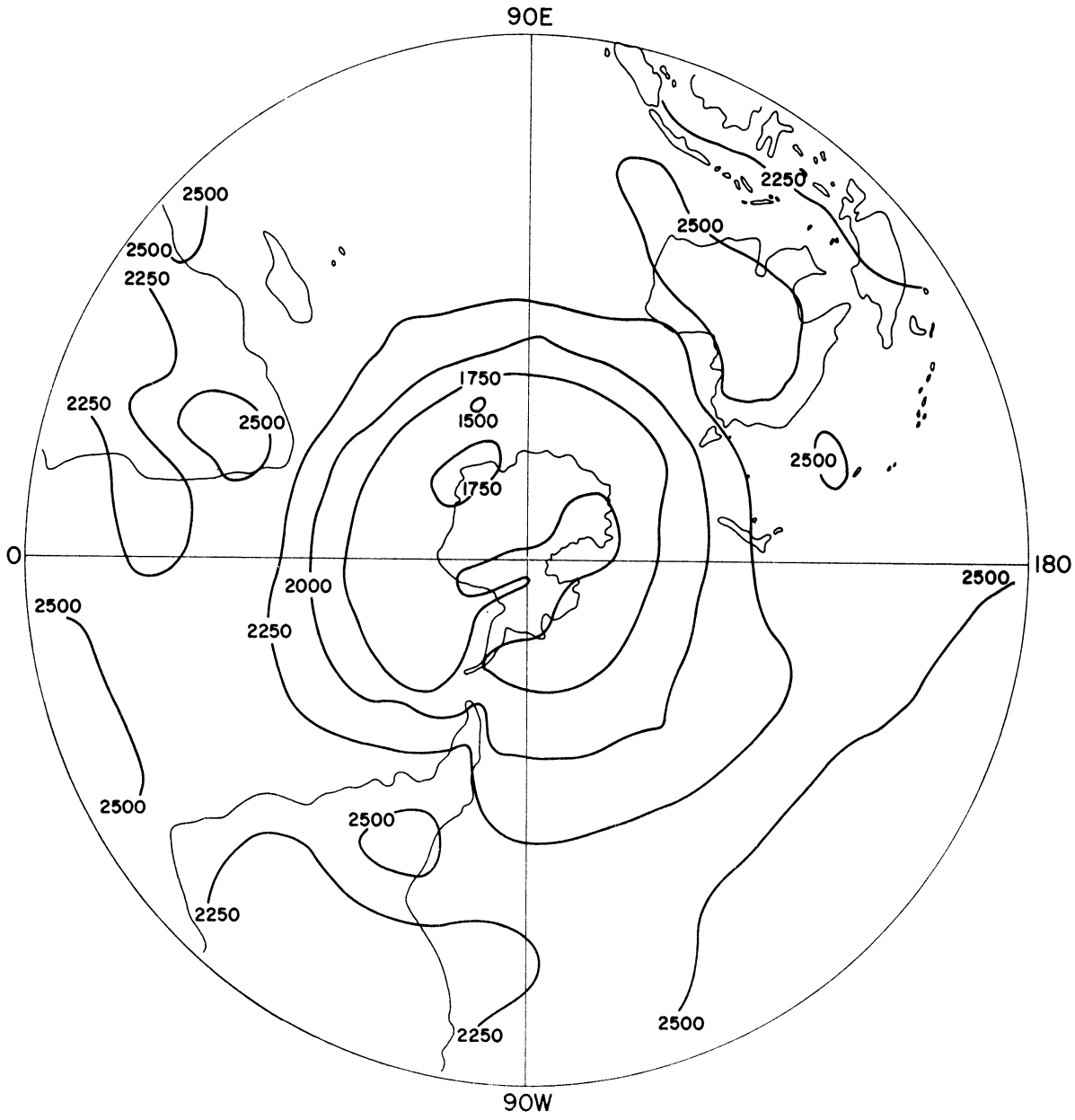

Figure IV-2 Distribution of the outgoing infrared flux (100 ergs/cm^2/sec) at the 137.5 mb level over the Southern Hemisphere in January

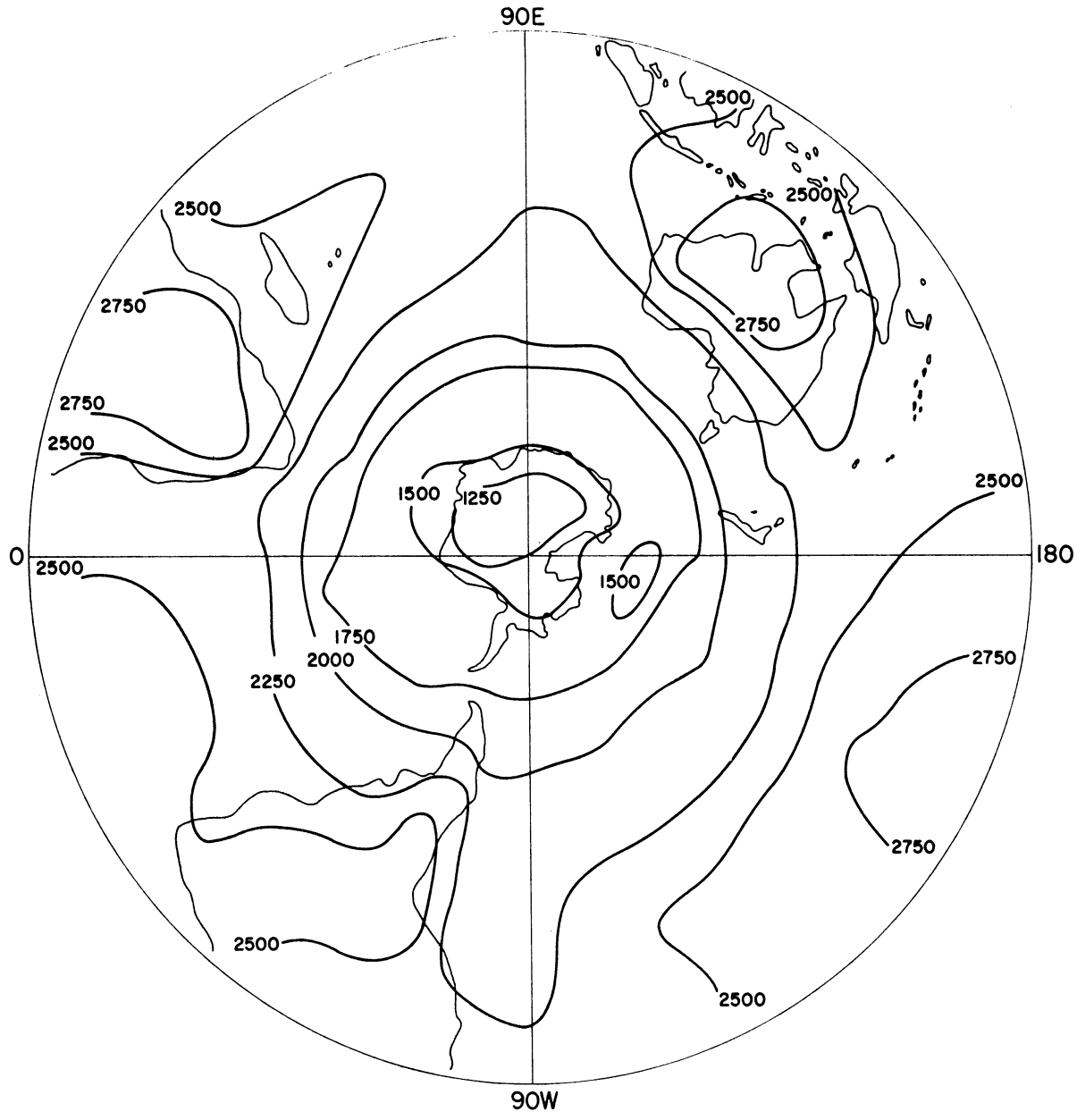

Figure IV-3 Distribution of the outgoing infrared flux (100 ergs/cm^2/sec) at the 137.5 mb level over the Southern Hemisphere in July

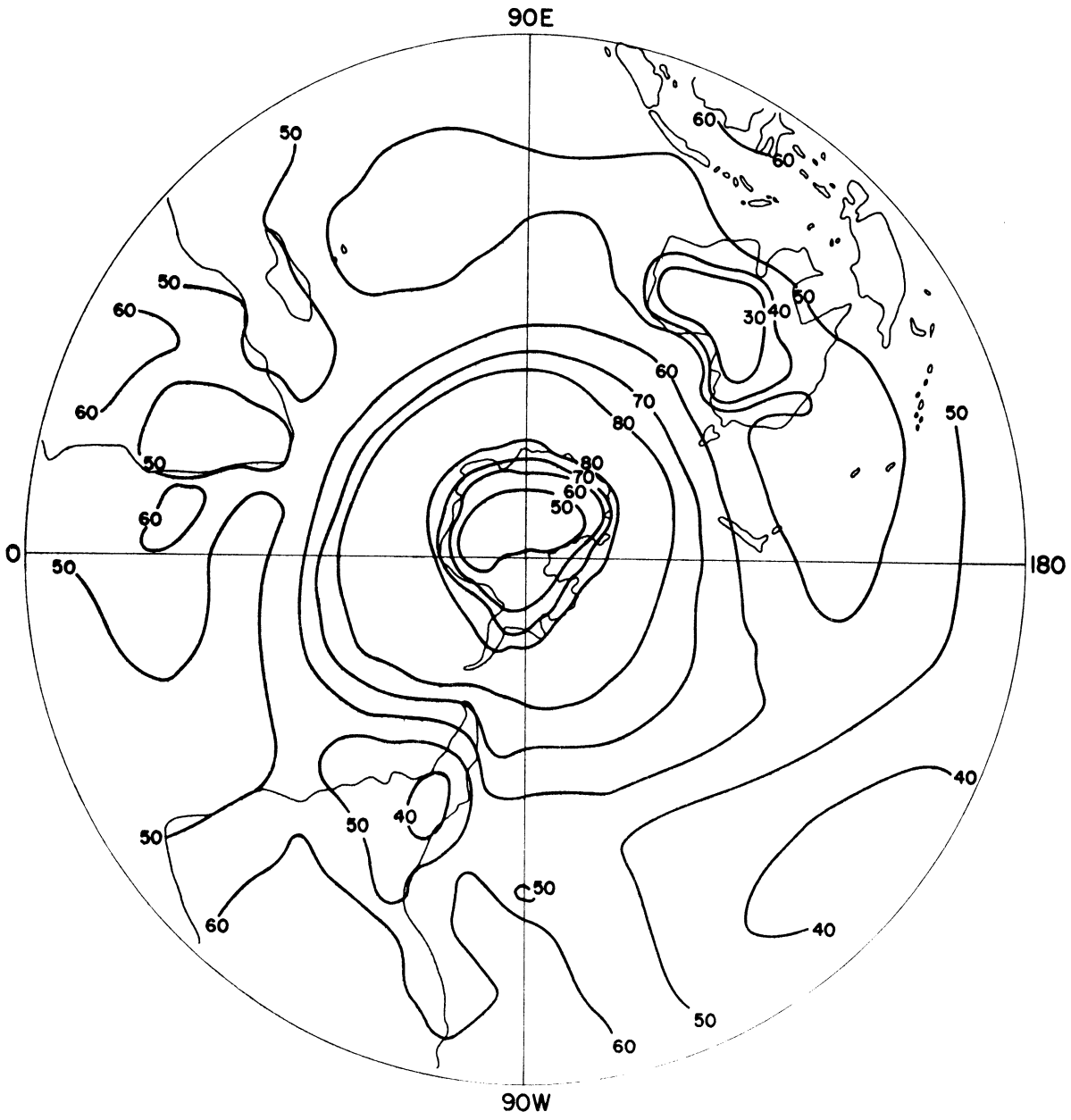

Figure IV-4 Distribution of total cloud cover (percent of sky covered) over the Southern Hemisphere in January

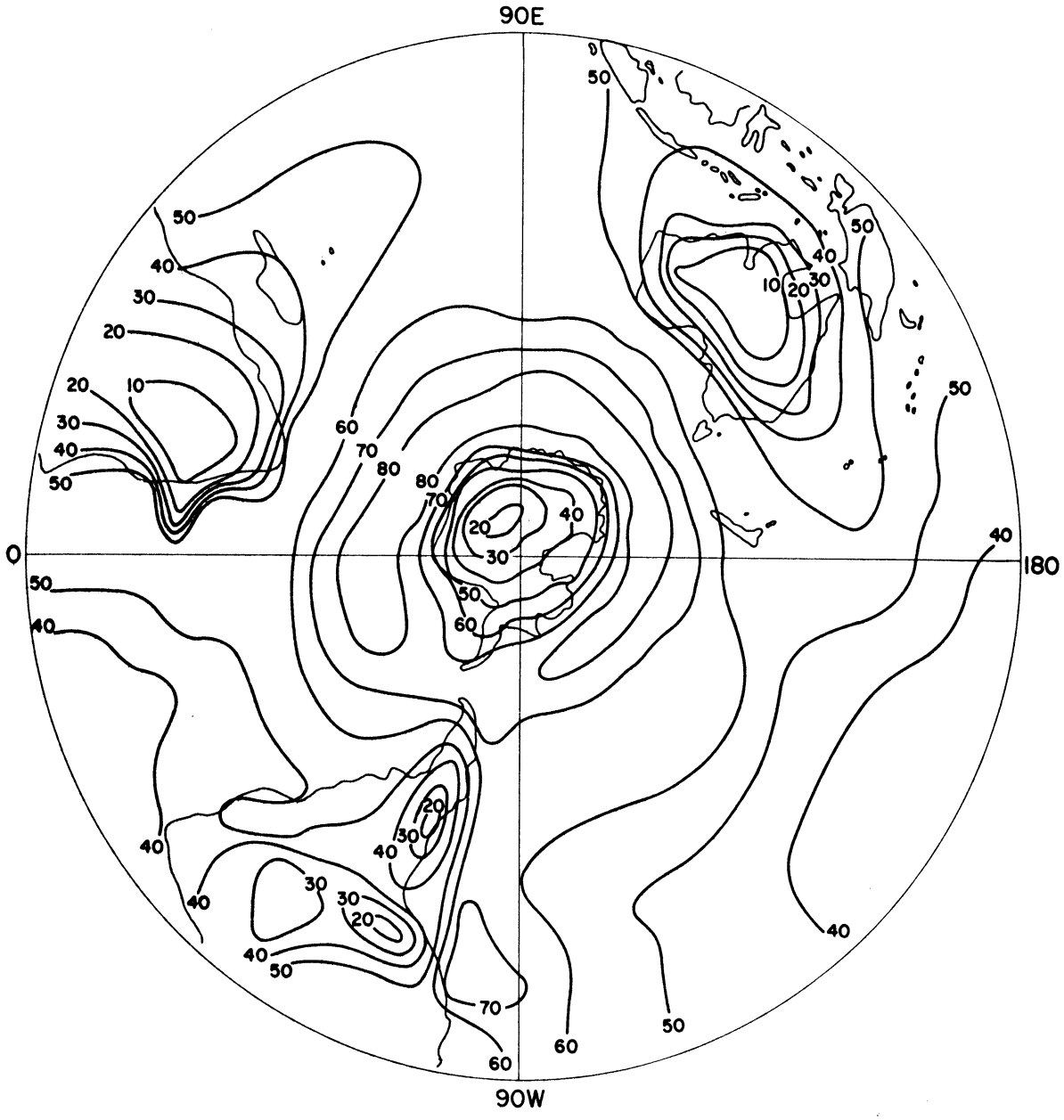

Figure IV-5 Distribution of total cloud cover (percent of sky covered) over the Southern Hemisphere in July

is considered. At 5^{o}S, because convective activity in the summer is substantially greater over land than over water, the cloud cover increases from water to land. As a result, there is a decrease in the outgoing flux as the effective emitting height of the flux increases. In July the zonal variations of tropical cloud cover show the same pattern as is seen at greater latitudes, that is, the cover is smaller over land, and the reversal in the variation of outgoing flux from land to water does not appear.

Vonder Haar and Suomi (1971) have also prepared a mean annual global map of the outgoing infrared flux using the satellite measurements mentioned earlier in this section. In order to compare their results to those of this work the flux values for January and July, from which Figures (IV-2) and (IV-3) were drawn, were averaged to form an annual distribution, given in Figure (IV-6). Vonder Haar and Suomi found the largest values of the outgoing infrared flux (around 264, 000 ergs $cm^{-2} sec^{-1}$) in the tropical latitudes with slightly greater values over water than land. Our results also indicate that the greatest values occur in the tropical latitudes. However we find greater (approximately 288, 000 ergs cm^{-2} sec^{-1}) values over the land areas. This agrees with the lower annual amounts of total cloud cover over land used in this study. Over equatorial Africa, Vonder Haar and Suomi show a local minimum in the outgoing flux while we find the opposite. However, if the flux distributions for January and July are examined, a local maximum is seen to occur in July and a local minimum in January with the maximum being somewhat stronger. These results are consistent with the assumed seasonal variations in the total cloud cover (Figures (IV-4) and (IV-5)).

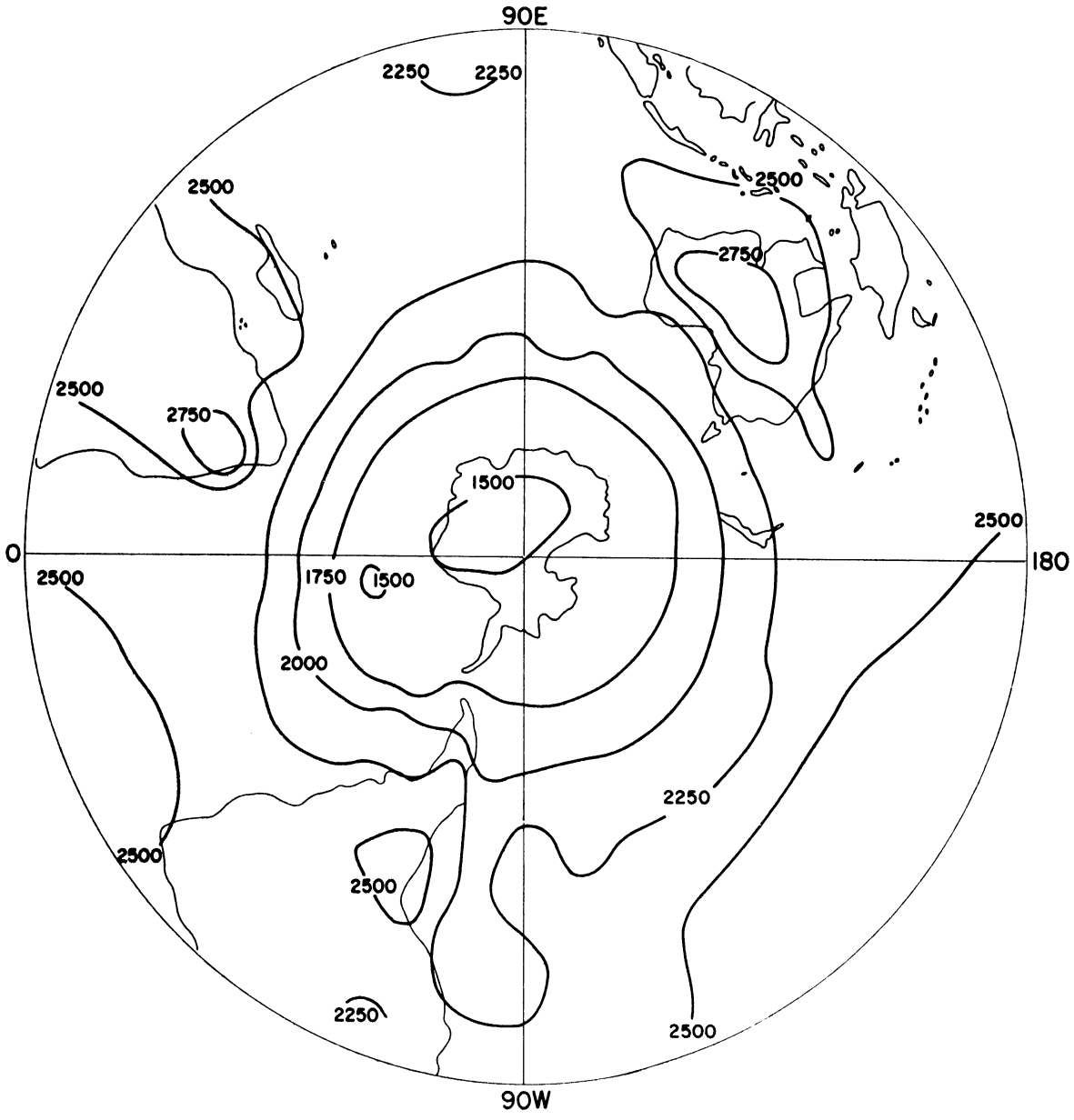

Figure IV-6 Annual mean distribution of the outgoing flux (100 ergs/cm/sec) at the 137.5 mb level over the Southern Hemisphere

Over Australia both annual distributions show local maxima of approximately the same magnitude, around 275, 000 ergs $cm^{-2}sec^{-1}$. Both sets of results have a tongue of smaller fluxes which extends toward the equator from about $35^{o}S$. Vonder Haar and Suomi find this over South America, while our results show it to occur just off the west coast of South America in association with the increased cloud cover in that region.

Both distributions also show a rather regular zonal pattern from the subtropics, extending to the pole. This is to be expected given the very small ratio of land to water in the southern hemisphere outside of the tropics. Minimum fluxes are found at the pole, with Vonder Haar and Suomi giving a value of about 125, 000 ergs $cm^{-2}sec^{-1}$ as opposed to our value of about 133, 000 ergs $cm^{-2}sec^{-1}$. Aside from the differences in the equatorial regions, the two distributions are quite similar.

In the first chapter, various extreme values of the zonally averaged infrared fluxes for the northern hemisphere as calculated by Katayama (1967 a) in terms of the net flux at 200 mb and by London (1957) in terms of the outgoing flux in the stratosphere were compared to Sasamori et al.'s comparable values at the top of the atmosphere for the southern hemisphere. Appendix F extends the comparison to the annual values.

Katayama's distribution is the most dissimilar of all. His values are lower than any of the others in either Table (IV-3) or Appendix F. The comparison however is not entirely valid since his values represent differences between the upward and downward fluxes while all the others only represent upward fluxes. At 200 mb, the level at which Katayama determines the net fluxes, the downward flux may be as much as one

sixth of the upward flux. If it is assumed that this is the case then the resulting values for Katayama's upward fluxes at 200 mb will somewhat excede the values of the present study and those of Sasamori et al. Thus Katayama's results may be in better agreement with the others than it first appears.

IV-2 NET INFRARED FLUX DIVERGENCE FOR THE ATMOSPHERIC COLUMN

Figure (IV-7) presents the zonally averaged meridional distributions for January and July of the net infrared flux divergence for the atmospheric column extending from the ground to 137.5 mb. Various factors effect these distributions, chief among them being cloud cover, temperature profile, and water vapor content. In order to sort out the different influences it will be helpful first to consider how each of these individually effects the total flux divergence.

As the amount of water vapor in an atmospheric column increases the downward flux at the bottom of the column increases and the upward flux at the top decreases. Thus it is not immediately possible to determine whether there will be a net gain or loss of infrared energy within the column. However, since in general the amount of water vapor in the upper troposphere is not great and its largest variability is found near the surface, it is only necessary to consider the flux variations at the surface. This being the case it is evident that, as the water vapor in an atmospheric column increases, the net flux divergence increases.

The amount of cloud cover, cloud thickness, and height are all important to the net flux divergence. At the top of the atmospheric column, as the cirrus cover increases, the upward flux, and therefore the net

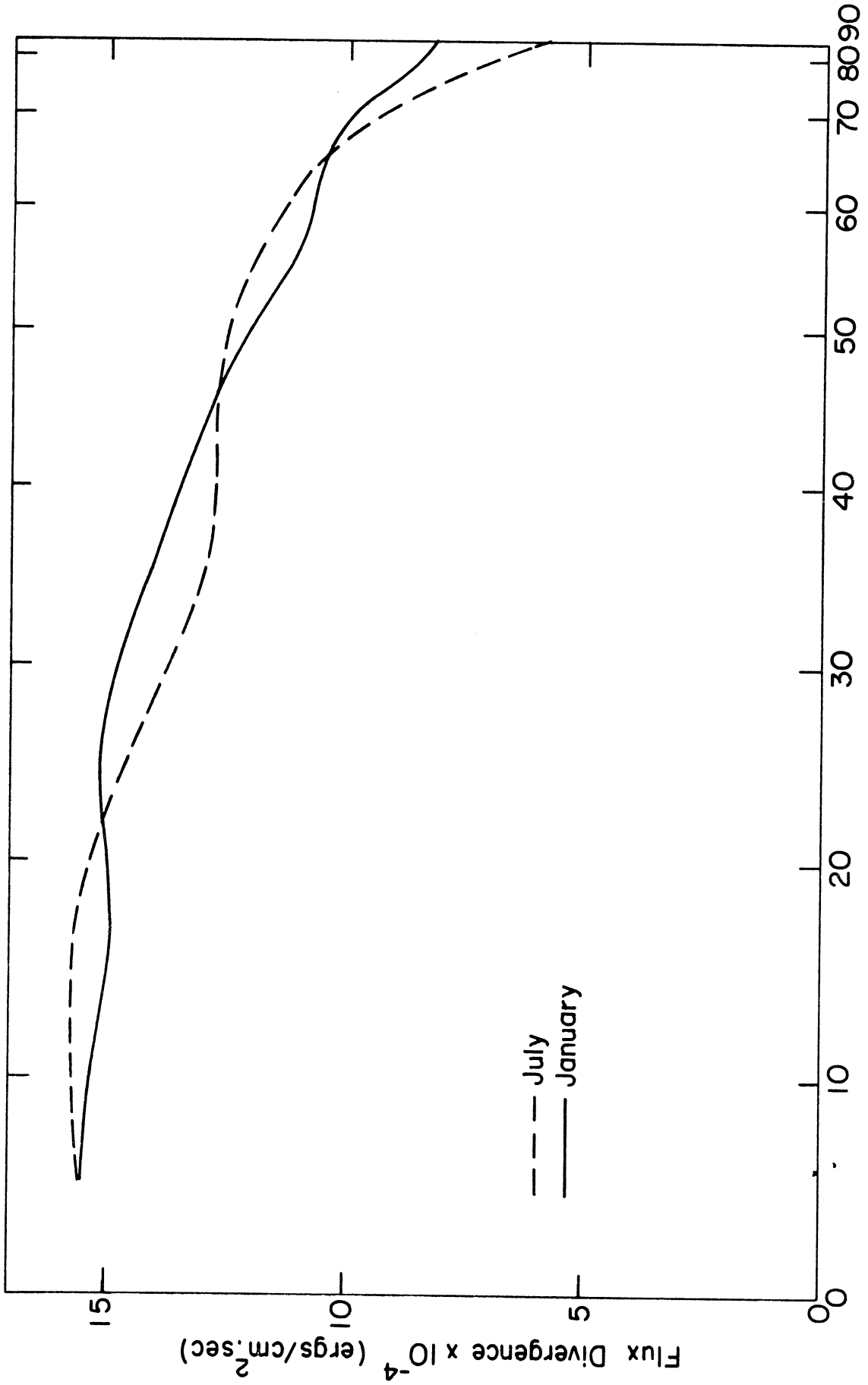

Figure IV-7 Zonally averaged meridional distributions of the net infrared flux divergence (ground to 137.5 mb)

flux divergence, will decrease. This is because as the cirrus cover increases the effective height at which the radiation exiting through the top of the column is emitted will rise to colder levels. Similarly the downward flux at the surface will have a lower effective emitting height as the cover increases. In this case the net flux divergence will increase. Clearly the net flux divergence increases when the high and /or low clouds are lower.

As regards temperature, if we assume that the surface temperature is the same for two atmospheric columns then the warmer column will experience a larger loss of infrared energy and have a larger net flux divergence. However if the surface temperatures differ, then the column over the warmer surface will have a larger upward flux at the surface and the net effect will depend on the actual temperature differences within the two columns.

Figure (IV-7) indicates that the net infrared flux over the atmospheric column is always divergent. The infrared radiation contributing to the downward flux at the lower boundary of the atmosphere originates mainly in the layers near the earth's surface and thus at temperatures not much lower than the surface temperature. This is because the lower layers of the atmosphere generally contain enough water vapor and carbon dioxide to be relatively opaque to infrared radiation. The spread between the effective emitting temperatures of the upward and downward fluxes passing through the bottom of the atmospheric column is therefore not large and the net flux will be small. However in the top layer of our model the upward flux is still substantial, having values approximately half as large as the values at the surface. The downward flux, on the other hand, is quite small. Thus the net infrared flux over the entire atmospheric column is negative, that is divergent, and primarily a function of the

outward flux at the top of the column.

The most obvious feature of the distributions in Figure (IV-7) is the general decrease of the net flux divergence with increasing latitude. This is primarily a result of the smaller water vapor amounts found nearer the pole. The same explanation suggests that there should be a greater net flux divergence in January than in July since there is considerably more water vapor present in the summer. This is true for a cloudless atmosphere as is illustrated in Table (IV-3) which gives the net flux divergences under clear sky conditions as calculated from zonally averaged atmospheric parameters for January and July.

TABLE (IV-3)

Meridional distributions of the total infrared flux divergence (x100 ergs $cm^{-2}sec^{-1}$) for a cloudless atmospheric column (ground to 137.5 mb) as calculated from zonally averaged atmospheric parameters for January and July.

	Latitude S								
Month	5^{o}	15^{o}	25^{o}	35^{o}	45^{o}	55^{o}	65^{o}	75^{o}	85^{o}
January	1778	1775	1744	1621	1435	1289	1172	900	845
July	1756	1750	1618	1446	1297	1148	960	708	610

If clouds are included, as is the case in Figure (IV-7), the net flux divergence in the summer is no longer greater than the winter divergence at all latitudes. Since the values in Figure (IV-7) and Table (IV-3) essentially differ only in that clouds are present in the former, it should be possible to explain the seasonal variation seen in the figure in terms

of the seasonal and latitudinal variations in cloud cover. As already noted the main variations in the net flux divergence are primarily the result of variations in the flux at the top of the atmospheric column. This suggests that the cirrus cover may be of major importance in these considerations.

For the zone centered around 15°S, the net flux divergence is greater in July. Referring to Table (IV-1) and Figure (II-3), the cirrus cover is greater and at a higher level in January which causes the net flux divergence to be smaller. This explanation for the seasonal distribution of the net flux divergence is supported by Figures (IV-9) and (IV-10). These figures, which are discussed more extensively in the next section, give the meridional profiles of the zonally averaged cooling rates. At 15°S the cooling rates are approximately the same up to about 250 mb. Above that July has larger cooling rates and it is therefore this upper region which contributes most substantially to the seasonal differences in the net flux divergence.

In the region between 25 and 45°S the net flux divergences in January are larger than in July. The cirrus cover in this region changes little nor do the temperatures vary substantially for a given latitude from summer to winter. In the absence of a differential effect due to cirrus clouds, the seasonal variations in moisture content exert the greatest influence and thus the net flux divergence is greater in January. From Figures (IV-9) and (IV-10) for the region from 25 to 45°S, the layer which contributes most to the larger net flux divergence in January is between approximately 400 and 550 mb. This layer is nearly free of clouds and it is the water vapor influence which predominates.

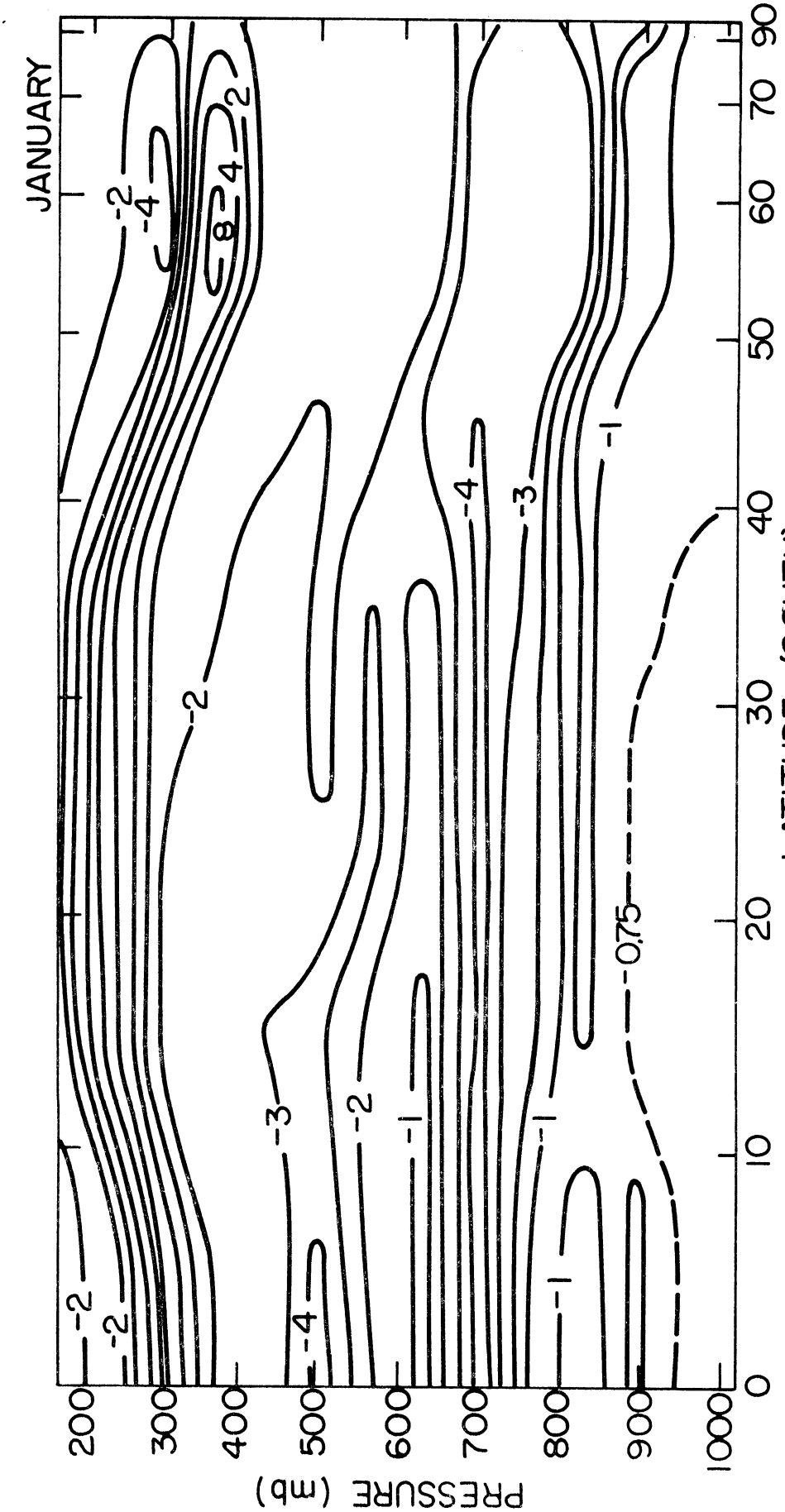

Figure IV-8 Zonally averaged infrared heating and cooling rates (^{o}C/day) for January with clouds present; no vertical smoothing

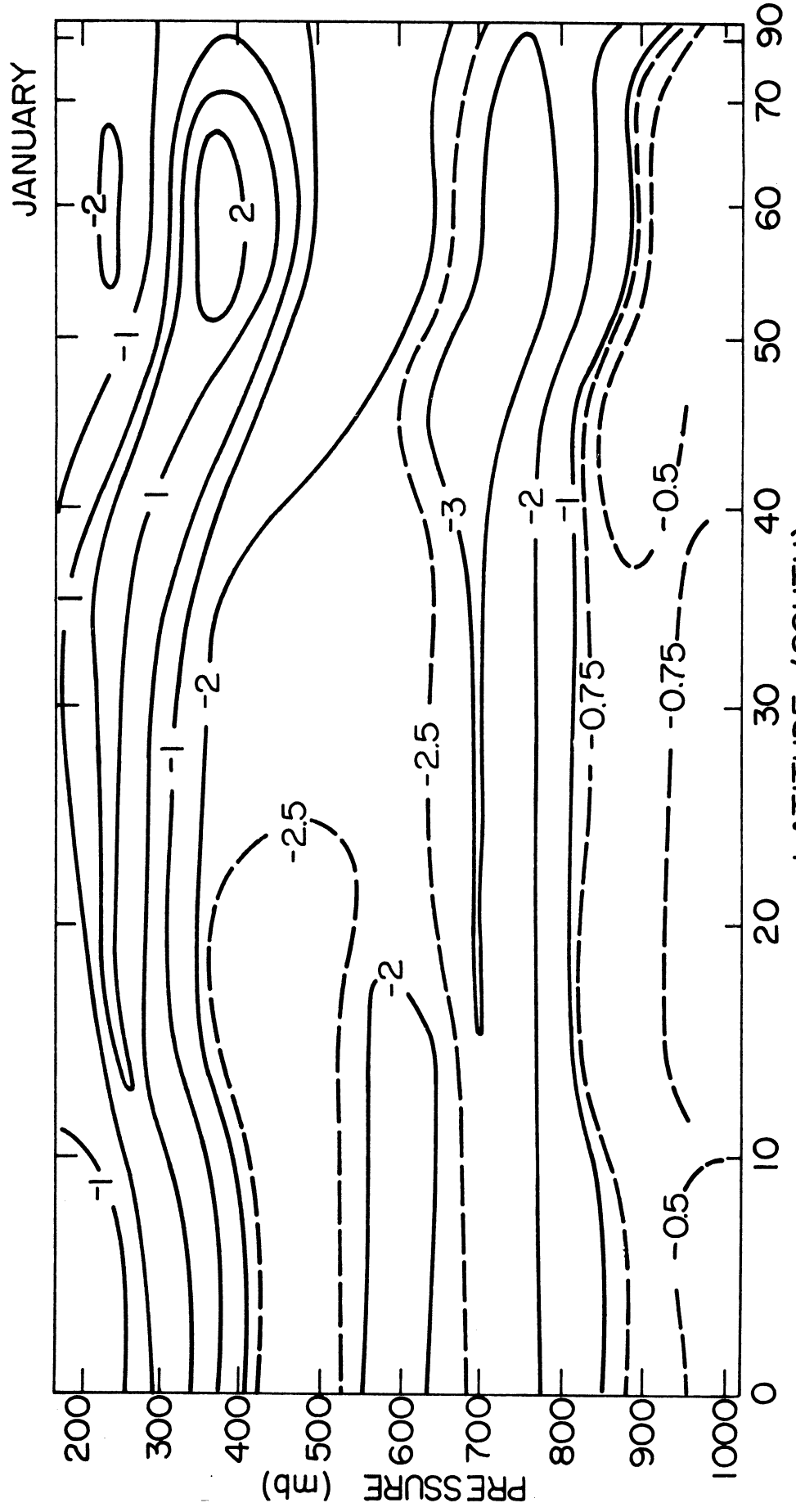

Figure IV-9 Zonally averaged infrared heating and cooling rates (^{o}C/day) for January with clouds present

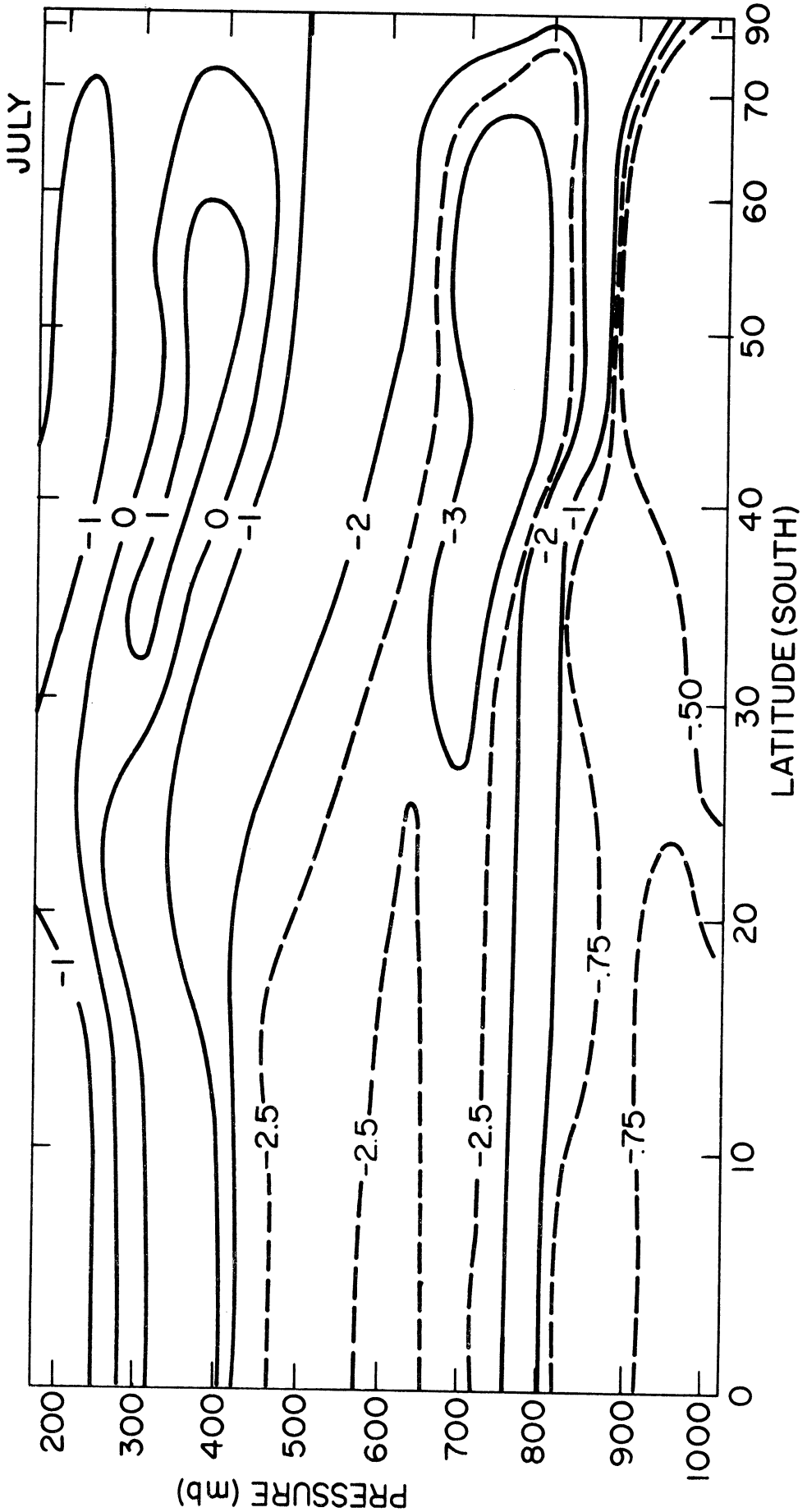

Figure IV-10 Zonally averaged infrared heating and cooling rates (^{o}C/day) for July with clouds present

In mid latitudes from about 45^{o} to 65^{o} the flux divergence is again larger during the winter season (July). From Table (IV-1) the cirrus cover is again greater in January. Figures (IV-9) and (IV-10) show that the cooling rates above 300 mb are greater in January than July. However in the layer directly beneath the cirrus there is considerably more heating in January. From this layer to the surface the rates are approximately the same. It can be concluded then that the cirrus cover still is the most important factor in producing the greater net flux divergences in July.

Poleward of 65^{o}S the cirrus amounts in both seasons become smaller and it is the greater moisture content found in January which yields the greater net flux divergence.

In order to explain why the net flux divergence decreases so rapidly in July at higher latitudes, consider Tables (IV-4) and (IV-5). The fluxes used in these tables are based on zonally averaged atmospheric parameters for cloudy skies.

TABLE (IV-4)

Meridional distribution of the difference between the upward and downward infrared fluxes (10^{2} ergs cm^{-2} sec^{-1}) at the surface

Month	Latitude S 5^{o}	15^{o}	25^{o}	35^{o}	45^{o}	55^{o}	65^{o}	75^{o}	85^{o}
January	726	786	849	818	664	465	451	649	764
July	832	859	876	786	615	484	420	542	543

TABLE(IV-5)

Meridional distribution of the difference between the downward and upward infrared fluxes (10^2 ergs cm^{-2} sec^{-1}) at the 137.5 mb level.

Month	Latitude S 5^o	15^o	25^o	35^o	45^o	55^o	65^o	75^o	85^o
January	-2276	-2286	-2351	-2183	-1918	-1556	-1513	-1621	-1557
July	-2395	-2475	-2334	-2081	-1865	-1561	-1461	-1280	-1163

It is clear that the steep decrease in net flux divergence in July occurs because of changes at the top of the atmospheric column. Water vapor and temperature both vary with latitude so as to yield a decrease in the divergence but it appears that the temperature is most crucial. In Table (A-3) the meridional variations of the temperature profiles with height are given. In January the meridional temperature gradients are small compared to those for January and it would appear that it is this seasonal difference which produces the larger decrease in net flux divergence in July.

Although the general shape of Sasamori et al.'s meridional distribution of the net infrared flux divergence averaged over the year for the atmospheric column is similar to that produced by these calculations, Sasamori et al.'s values are somewhat larger.

TABLE (IV-6)

Comparisons of the annual mean zonally averaged net infrared flux divergences (ly/day) for atmospheric columns.

Latitude S	5°	15°	25°	35°	45°	55°	65°	75°	85°
Sasamori et al. (stratosphere)	388	387	381	370	360	346	318	269	225
Present Study (137.5 mb)	321	316	306	277	263	238	217	175	146
Present Study (stratosphere)	346	346	334	319	323	301	304	266	238
London (stratosphere) (N. Hemisphere)	365	359	350	334	334	325	317	290	272

In Table (IV-6) the annual mean zonally averaged values for the net infrared flux divergence are given for the present calculations both with and without the contribution from stratospheric water vapor, as well as the results of Sasamori et al. (1971). Even with the stratospheric contributions, the present results are somewhat smaller than those of Sasamori et al. Table (IV-7) separates the zonally averaged net flux divergences, as calculated in this work and by Sasamori et al., into the components at the surface and top of the atmosphere for January at 45° S. [1]

---

[1] Results similar to those found in Table (IV-7) are obtained at the other latitudes and in July.

TABLE (IV-7)

Zonally averaged infrared radiation budget terms (ly day^{-1}) at the top and bottom of the atmospheric column for January at $45^{o}S$

Latitude	$45^{o}S$	
	Present Study	Sasamori et al.
Upward flux at surface	770	778
Downward flux at surface	634	680
Net upward flux at surface	136	98
Upward flux at atmospheric top	459	472
Net loss from atmosphere	323	374

The greater values of the net upward flux at the top of the atmosphere found by Sasamori et al. can be explained by noting that their cirrus and altrostratus covers are smaller than those used in this study. Most of the difference between the net losses arises because of the differences in the values of the downward fluxes at the surface. Since both studies used the same dew point temperatures in the lower atmosphere, it is unlikely that differences in the water vapor will account for the differences observed in Table (IV-7). Table (IV-8) compares the zonally averaged amounts of precipitable water vapor used in the two studies. It seems most reasonable to assume that the differences arise because of differences in the heights of the clouds. Unfortunately it is not possible to carry out any comparison of the heights because values are not given by Sasamori et al.

TABLE (IV-8)

Amount of precipitable water vapor

(gm cm^{-2}) zonally averaged

January									
Latitude S	5^o	15^o	25^o	35^o	45^o	55^o	65^o	75^o	85^o
Sasamori et al.	4.22	3.70	2.99	2.34	1.79	1.29	0.79	0.38	0.18
Present Study	4.25	3.79	2.91	2.31	1.66	1.16	0.74	0.21	0.09

July									
Latitude S	5^o	15^o	25^o	35^o	45^o	55^o	65^o	75^o	85^o
Sasamori et al.	3.56	2.82	2.08	1.52	1.10	0.74	0.41	0.17	0.06
Present Study	3.69	2.60	1.84	1.49	1.06	0.72	0.35	0.09	.0

Referring again to Table (IV-6), the meridional profiles of the various net infrared flux divergences can be compared for the Northern and Southern Hemispheres. Given the greater cloud cover in the Southern Hemisphere and the greater water vapor concentrations in the Northern Hemisphere (London's Northern Hemisphere values are larger than Sasamori et al.'s which are larger than those used in this study), a greater net flux divergence would be anticipated for the Northern Hemisphere. This is the case when London's northern hemisphere values are compared to the present results.

IV-3 ZONALLY AVERAGED INFRARED HEATING AND COOLING RATE CROSS SECTIONS

Ideally, climatic cooling rates should be formed from the averages of cooling rates calculated from many synoptic observations. This is obviously impractical and it is therefore necessary to characterize the

atmosphere in terms of various mean parameters and to calculate the climatic cooling rates from them. However, as mentioned in the introduction, the output from such a procedure should be examined carefully to see that erroneous results are not present as the result of neglecting the variations in the parameters which are expressed in terms of their averages. Such a problem does exist with respect to cloud heights. By requiring the clouds to assume fixed heights over a given season, unrealistically large heating and cooling rates (over 8^{o}C per day) may be obtained.

Since no quantitative information is available as to how cloud heights are distributed in time, the following vertical smoothing procedure, used by Katayama (1967b), has been adopted.

$$\left(\frac{\partial \bar{T}}{\partial t}\right)_i = \frac{\partial T/\partial t)_{i+1} + 2\,\partial T/\partial t)_i + \partial T/\partial t)_{i-1}}{4} \qquad \text{(IV-1)}$$

where i indicates the level for which the cooling rate $\partial T/\partial t$ is being smoothed and i-1 and i+1 the levels directly above and below level i. For the uppermost and lowest layers

$$\left(\frac{\partial \bar{T}}{\partial t}\right)_i = \frac{\partial T/\partial t)_{i-1}^{i+1} + 2\,\partial T/\partial t)_i}{3} \qquad \text{(IV-2)}$$

This technique has the effect of vertically spreading the calculated heating and cooling rates in such a way as to represent more realististically their distribution in time.

Figures (IV-8) and (IV-9) illustrate the effects of this smoothing for one meridional cross section of cooling rate profiles. It is seen

that the general features of the unsmoothed profiles are preserved in the smoothed versions, while the regions of strong heating and cooling in the layers below and above the clouds are smoothed. This is most evident in the region directly beneath the cirrus layer. In the unsmoothed profiles this region of heating is narrow with heating rates ranging from about 4 to over 8°C per day between the equator and 65°S. On the other hand, in the smoothed profiles, the strongest heating rate is only 2.8°C per day but the verticalextent of the heating is much greater. It is important to note that the net flux divergence for the atmospheric column has not been changed but only redistributed in height.

Individual cooling rate profiles[1] for January and July have been calculated for climatic conditions with clouds present at 10° intervals from 5° to 85°S and for every 40° of longitude. These values were also zonally averaged to form meridional cross sections as presented in Figures (IV-9) and (IV-10). In addition, zonally averaged values of the atmospheric parameters involved in the cooling rate calculations were computed for each latitude for January and July and these values were then also used to generate cooling rates. The two sets of meridional cross sections differ in general less than 0.1°C per day. Only near the pole do their differences excede 0.2°C per day and then in only six cases and never by more than 0.6°C per day. Thus the nonlinearity of the transfer equation with respect to temperature, pressure, and relative humidity does not interfere with calculating the zonal means for the cooling rates from zonally averaged atmospheric parameters.

---

[1] All cooling rates discussed hereafter have been smoothed by the above procedure.

Individual cooling rate profiles were also calculated for clear skies for January and July over the same grid as that used to calculate the cloudy sky profiles. Zonal averages were formed and the cross sections are presented in Figures (IV-11) and (IV-12). By examining these figures and comparing them with Figures (IV-9) and (IV-10) for which clouds are present, it is possible to isolate the influences of water vapor and temperature from those of clouds.

From the clear sky figures it can be seen that the cooling rates increase seasonally from July to January and latitudinally from pole to equator. Only near the surface north of 45^{O}S is the cooling somewhat greater in July. At 5^{O}S the level of maximum cooling is at 305 mb in January and 370 mb in July. At 65^{O}S these levels have dropped to 435 and 500 mb respectively and at the pole they are both at approximately 600 mb. In January and to a lesser extent in July, at the high latitudes, there is also a secondary cooling maximum with respect to meridional variations.

The vertical temperature structure is primarily responsible for the shape of the cooling rate profile. As shown by Brunt (1939) a temperature structure with a negative curvature i.e., $d^2T/dz^2 < 0$ produces a cooling, the maximum in cooling associated with the smallest curvature. In the polar latitudes the cooling rates are complicated somewhat by the presence of the polar inversion in the lower layers of the atmosphere. The inversion (see Appendix A) coincides with the level of maximum cooling, dropping from July to January and from 85 to 75^{O}S. At 75^{O}S this is not evident from Figures (IV-11) and (IV-12) but can only be seen from the actual cooling rates. Near the inversion, the atmosphere

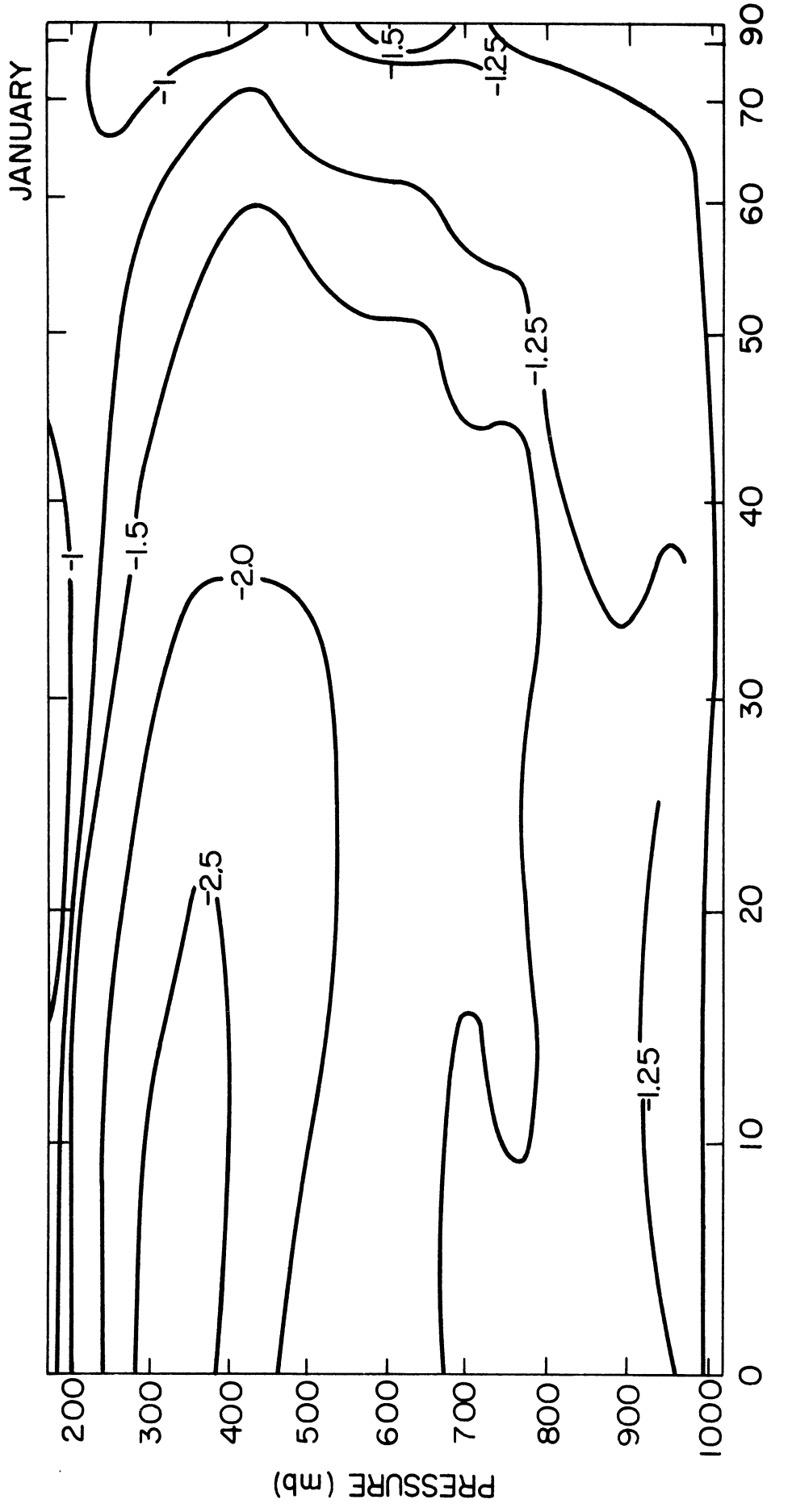

Figure IV-11 Zonally averaged infrared heating and cooling rates (^{o}C/day) for January without clouds

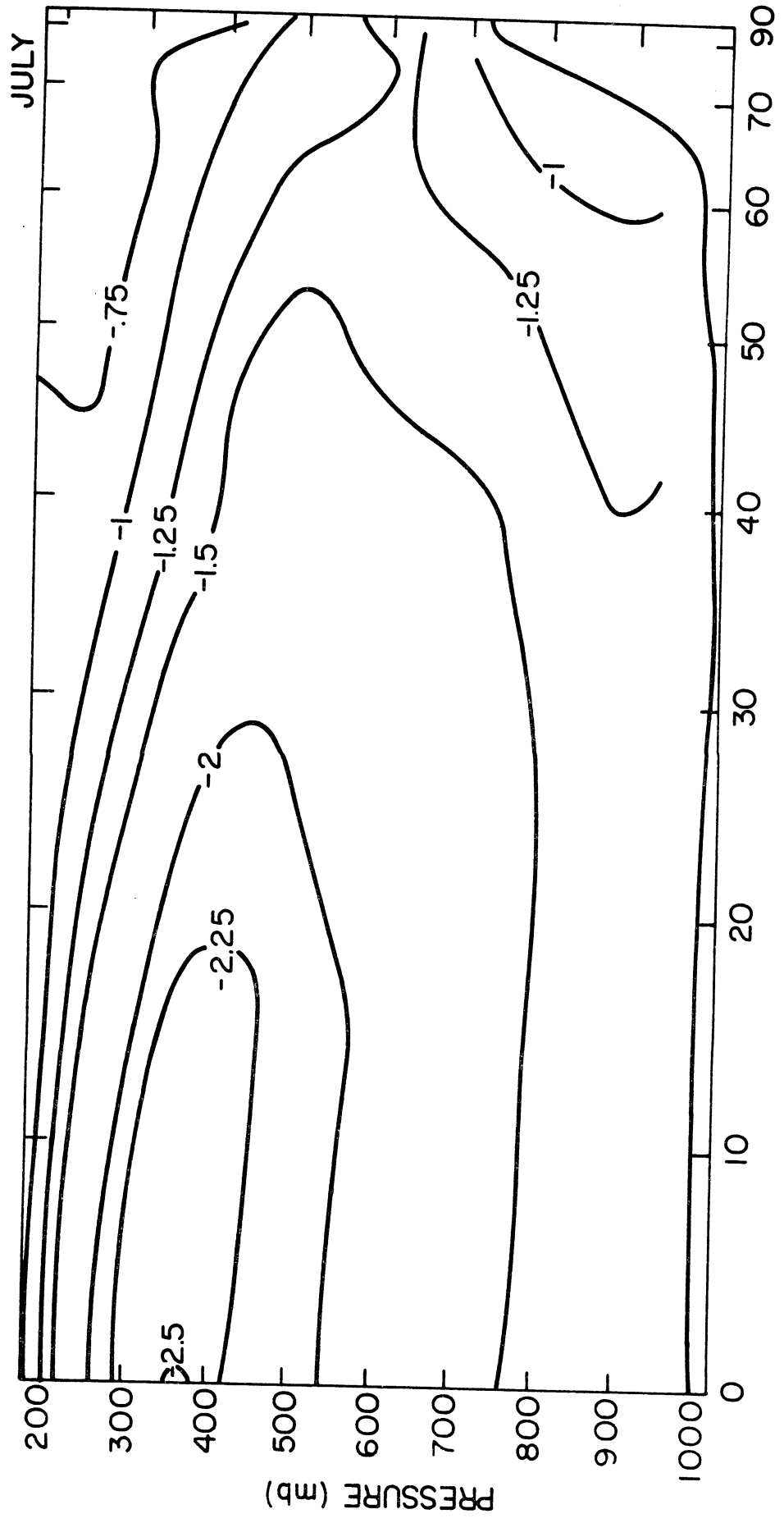

Figure IV-12 Zonally averaged infrared heating and cooling rates (^{o}C/day) for July without clouds

is radiating at a higher temperature than from those regions of the atmosphere from which it is absorbing energy, thus producing a local maximum in the cooling rate profile.

Figures (IV-9) and (IV-10)give the meridional cooling rate cross sections when clouds are present in the atmosphere. The rather simple variations observedfor clear skies have now disappeared and have been replaced by more complex patterns of cooling directly above the clouds and weak cooling or moderate heating beneath the clouds.

The warming levels aloft in January and July lie just beneath the bases of the cirrus clouds as can be seen by examining the cloud heights given in Figure (II-3). For instance in July the cirrus deck is highest between 20 and 30^{o}S and this is reflected in the increase in the height of the warming layer at the same latitudes. Also in July as compared to January the warming zone has somewhat smaller rates at all latitudes and is located at slightly lower levels between 15 and 45^{o}S. For both January and July the maximum heating occurs at about 55^{o}S while cooling occurs at 85^{o}S; these results reflect the cirrus cover which is maximum at 55^{o}S and minimum at 85^{o}.

It should be noted that the maximum cirrus cover is found at the latitudes at which the globe is entirely circled by ocean and it is for this reason that both total cloudiness and cirrus cover are greatest there. In the clear sky calculations there is no evidence of this hemispheric belt of ocean.

The structure of the cooling below the level of warming can also be analyzed in terms of the cloud cover. From the equator to about 25^{o}S in both January and July there is a layer of maximum cooling extending from

about 700 to 500 mb enclosing a layer of relatively smaller cooling rates around 600 mb. These variations can be explained if the clouds below the cirrus, excluding cumulonimbus, are divided into two groups, low (Cu, Ns, and St) and middle (As). This is, in fact, the sort of division scheme which many of the studies employ. Reference to Figure (II-3) shows that such a procedure is justified from the equator to about 25^{o}S. Beyond that latitude, low and middle clouds are not so easily separated since their combined vertical distribution is relatively continuous. From this simplified view of the vertical distribution of clouds, the layer of relatively small cooling is seen to result from the increased downward flux from the bases of the middle clouds. The larger cooling rates above and below this region result from the larger flux divergences at the tops of the middle clouds and cumulonimbus, and the tops of the low clouds respectively.

Beyond 35^{o}S in both January and July the region of relatively clear skies around 650 mb interrupted only by cumulonimbus clouds, closes. The cooling rate profiles for both months now show a single maximum occurring in the layer above the four lower cloud types. This maximum, whether in January or July, is greater than either of the double maxima found closer to the equator because the cloud cover is greater around 55^{o}S than it is nearer the equator. Also because of the decrease in the heights of the clouds from equator to pole this overall layer of cooling shows a parallel decrease in its height. Note that due to the influence of the varying cloud cover the general decrease in the magnitude of the cooling rates observed for clear skies from equator to pole has been reversed.

In the layers near the earth's surface the level of minimum cooling closely follows the shifting heights of the common base of the lowest three

cloud types. In January the common base of these clouds is found at 890 mb at 5°S, rises to 825 mb between 15 and 45°S, and returns to 890 mb between 55 and 85°S. At the latitudes where the clouds are closer to the surface the minimum cooling is found in the layer adjacent to the surface. In the region from 15 to 45°S where the clouds lift, the level of minimum cooling is at 900 mb with a slight increase in cooling nearer the surface. In July the common base occurs at 825 mb from 5 to 35°S and at 890 mb thereafter while the level of minimum cooling drops from approximately 900 mb to 965 mb between 35 and 45°S.

London (1957) and Davis (1961) have provided zonally averaged meridional cross sections of the cooling rates for the Northern Hemisphere, while Dopplick (1970) has done similarly for the entire globe. These cross sections were discussed and compared in Chapter I. In Figure (IV-13) Dopplick's cross sections for January and July are given up to 200 mb. These figures can be compared to Figures (IV-9) and (IV-10) of the present study. The cross sections in both cases do not show sufficient seasonal variations to necessitate distinguishing between seasons in the following discussion. The zone of maximum cooling above the lower and middle clouds is evident and of equal strength in both sets of figures north of 40°S. However south of 40°S, our values increase in magnitude and decrease in height, while Dopplick's results indicate just the reverse. Above this region of strong cooling both sets of cross sections show a

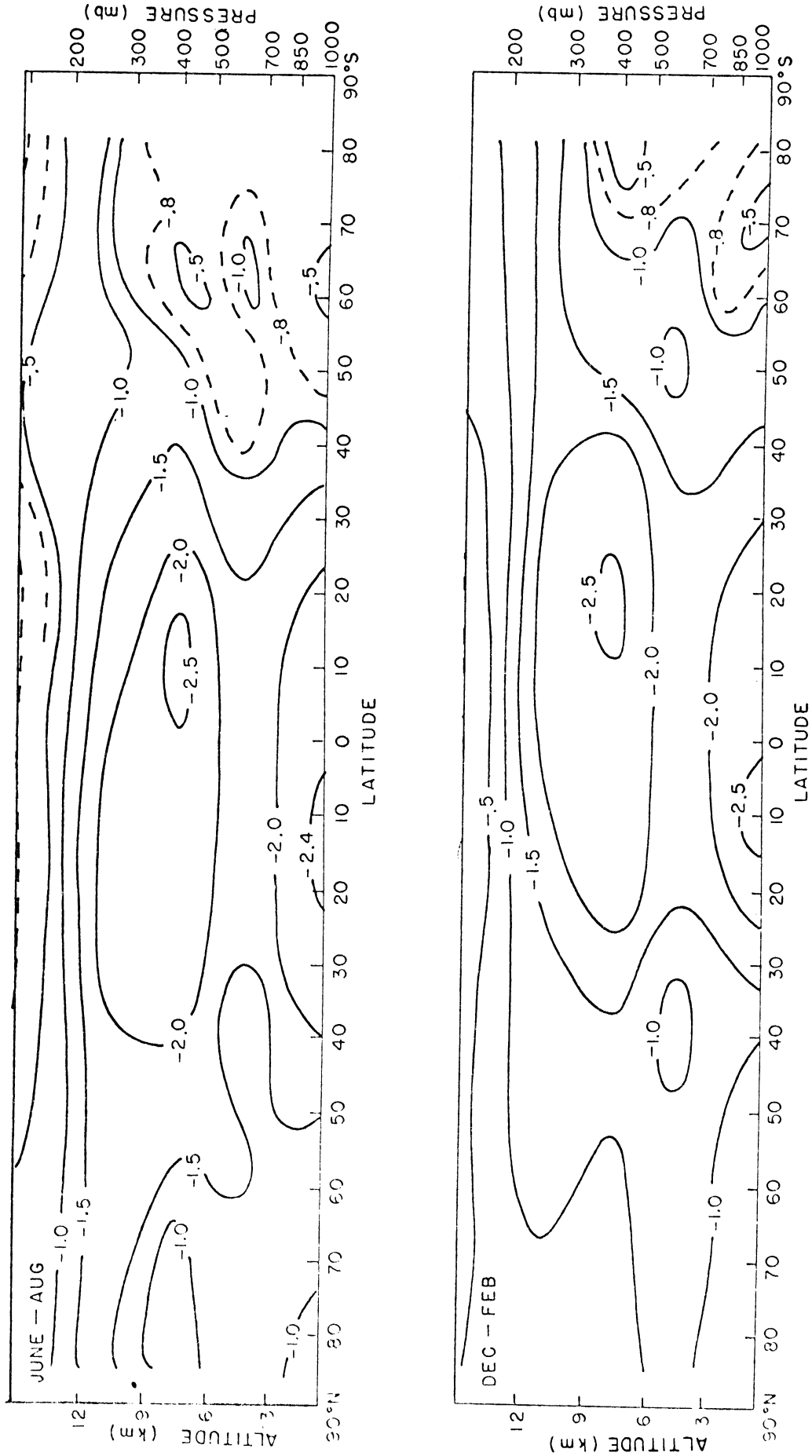

Figure IV-13 Meridional infrared cooling rate (^{o}C/day) cross sections for January and July (from Dopplick (1970))

decrease in cooling although only our values show any heating. Near the surface in the northern half of the hemisphere Dopplick's cooling rates are over twice as large as those of this work. In the southern half, below about 800 mb, the cross sections are quantitatively and qualitatively similar, but above 800 mb they are only qualitatively alike.

The reasons for the differences between these results would seem to arise because of differences in the cloud cover data. Unfortunately this is difficult to verify because relatively little information is given by Dopplick regarding his cloud data. However from the information that is given, it is evident that Dopplick's total cloud cover values are lower than those used in this study. Table (IV-9) gives London's total cloud cover for the Northern Hemisphere, Dopplick's for the entire globe and this study and Sasamori et al.'s for the Southern Hemisphere. Except possibly in the high latitudes of the Southern Hemisphere, Dopplick's values were derived from twelve months of satellite observations (thus each of the values in the table is based on, at most, three months of observations). Especially in the lower latitudes the differences between his values and either those of London in the Northern Hemisphere or ours and Sasamori et al.'s in the Southern Hemisphere are striking. This would, at least in a qualitative way, explain some, if not most, of the discrepancies between the two sets of cross sections. The same explanation accounts for the fact that no heating rates are found either by Dopplick or any of the Northern Hemisphere infrared studies while they are found in this work.

It is interesting to compare the present Southern Hemisphere cooling rate cross sections with those of London for the Northern Hemisphere (it has already been noted that Dopplick's Southern Hemisphere

cross sections resemble both his own and London's for the Northern Hemisphere). In addition to large scale similarities, some of the smaller features appear on both cross sections. The increase in the heights of the maximum heating and cooling layers from the equator to 25°, the double maxima of cooling near and over the equator, and the single layer of maximum cooling at higher latitudes (and thereby the increasing cooling rates from the mid-latitudes toward the pole) all appear in both cross sections. In the winter the double maxima of cooling does not appear in London's distribution but is present, although rather weak in our results.

TABLE (IV-9)

Total cloud cover (percent of total sky) zonally averaged

Winter									
Latitude S	5°	15°	25°	35°	45°	55°	65°	75°	85°
London	47	36	38	50	59	63	58	47	40
Dopplick(N)	20	16	23	34	48	62	59	55	-
Dopplick (S)	20	18	19	27	52	69	64	48	-
Present study	45	42	44	55	65	77	76	46	35
Sasamori et al.	46	43	46	54	65	76	70	51	38
Summer									
Latitude S	5°	15°	25°	35°	45°	55°	65°	75°	85°
London	54	49	42	41	55	63	66	69	64
Dopplick (N)	22	20	18	27	34	42	65	68	-
Dopplick (S)	22	25	27	29	35	46	65	68	-
Present study	52	51	48	52	65	82	84	61	52
Sasamori et al.	52	51	49	53	65	78	77	62	51

The single maximum of cooling near the pole is present in both cross sections. That these similarities should exist is not surprising since they are primarily a function of the cloud distributions which are alike in both hemispheres. In general, the rates are larger in our cross sections (heating rates appearing where London has only smaller cooling rates) which is also consistent with the relative cloud covers in the two hemispheres.

IV-4 MERIDIONAL COOLING RATE CROSS SECTIONS AT VARIOUS LONGITUDES

A major purpose of this study was to calculate the meridional cooling rate cross sections at a series of longitudes so that the variations from land to water might be examined. Also this allowed us to determine how well the zonally averaged mean cross sections represented the hemisphere. As mentioned earlier in this chapter cross sections were computed for each 40° of longitude, as well as for 20°E and 60°W for January and July with clouds present. These are presented in Figures (IV-14) through (IV-24). Of these, the cross sections for 60°W, 120°E, and 20°E cross South America, Australia, and Africa respectively, while near the pole they all traverse Antarctica.

It is helpful to review briefly how the longitudinal variations of the relevant atmospheric parameters were treated. Only for the ambient and dew point temperatures and total cloud cover and cover by type is there sufficient information available to do this. For ozone concentrations and cloud heights it has been necessary, because of the lack of data, to neglect all longitudinal variations. Carbon dioxide has been assumed to be constant throughout the troposphere and with time.

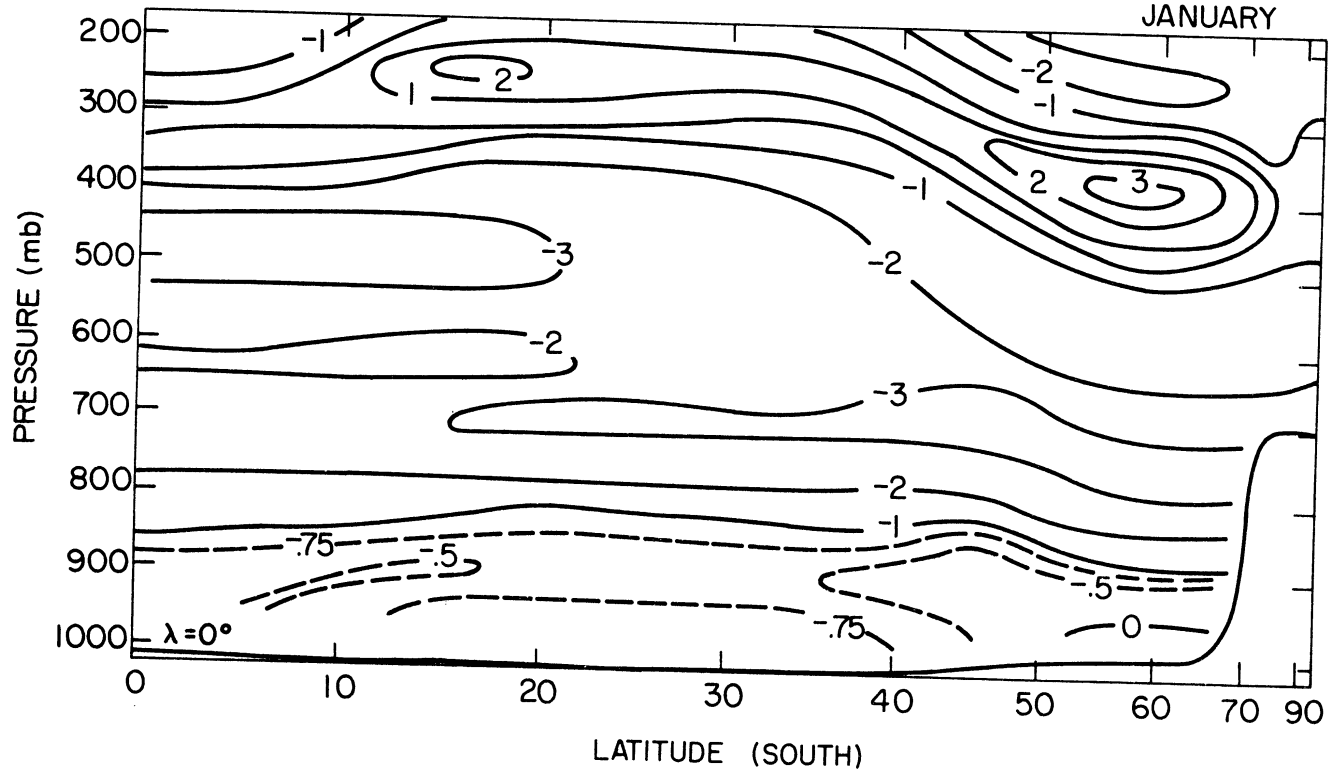

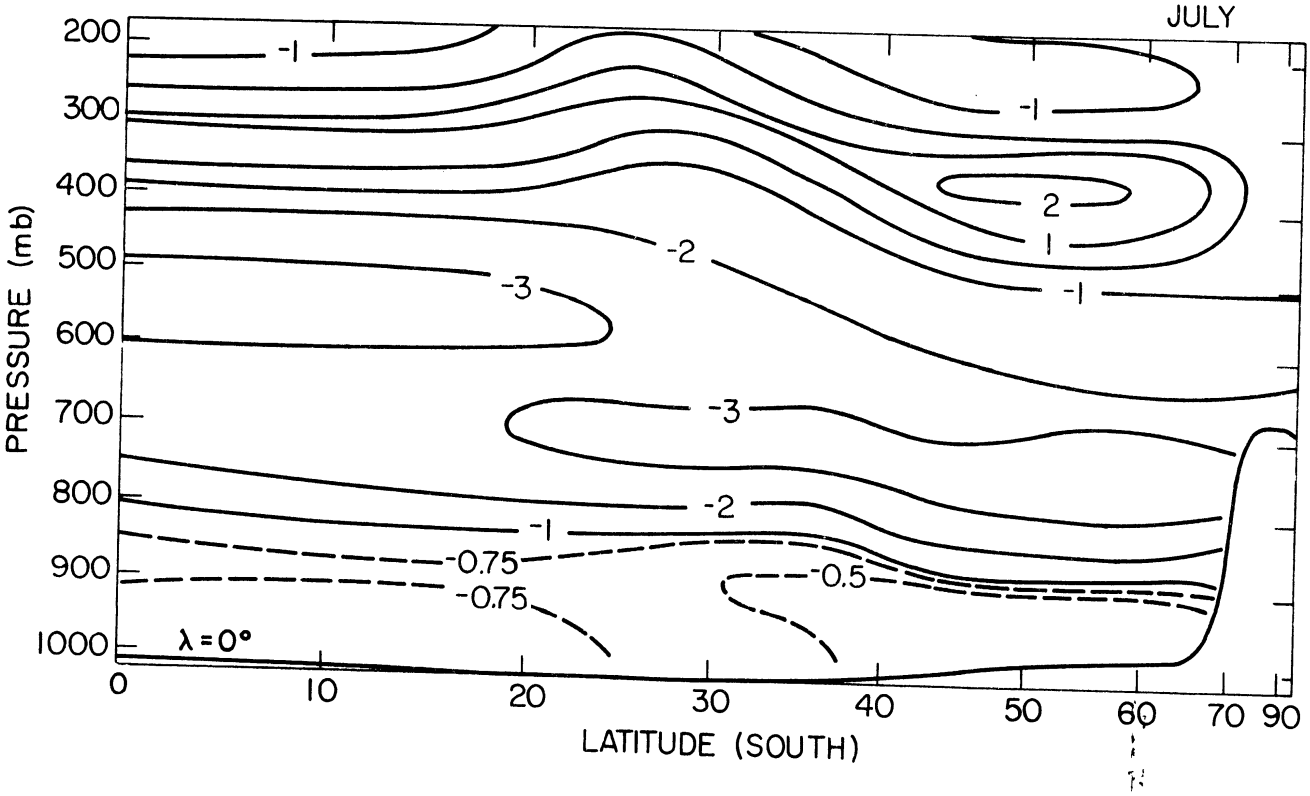

Figure IV-14 Meridional distributions of infrared heating and cooling rates for January and July for a longitude of 0^{0}

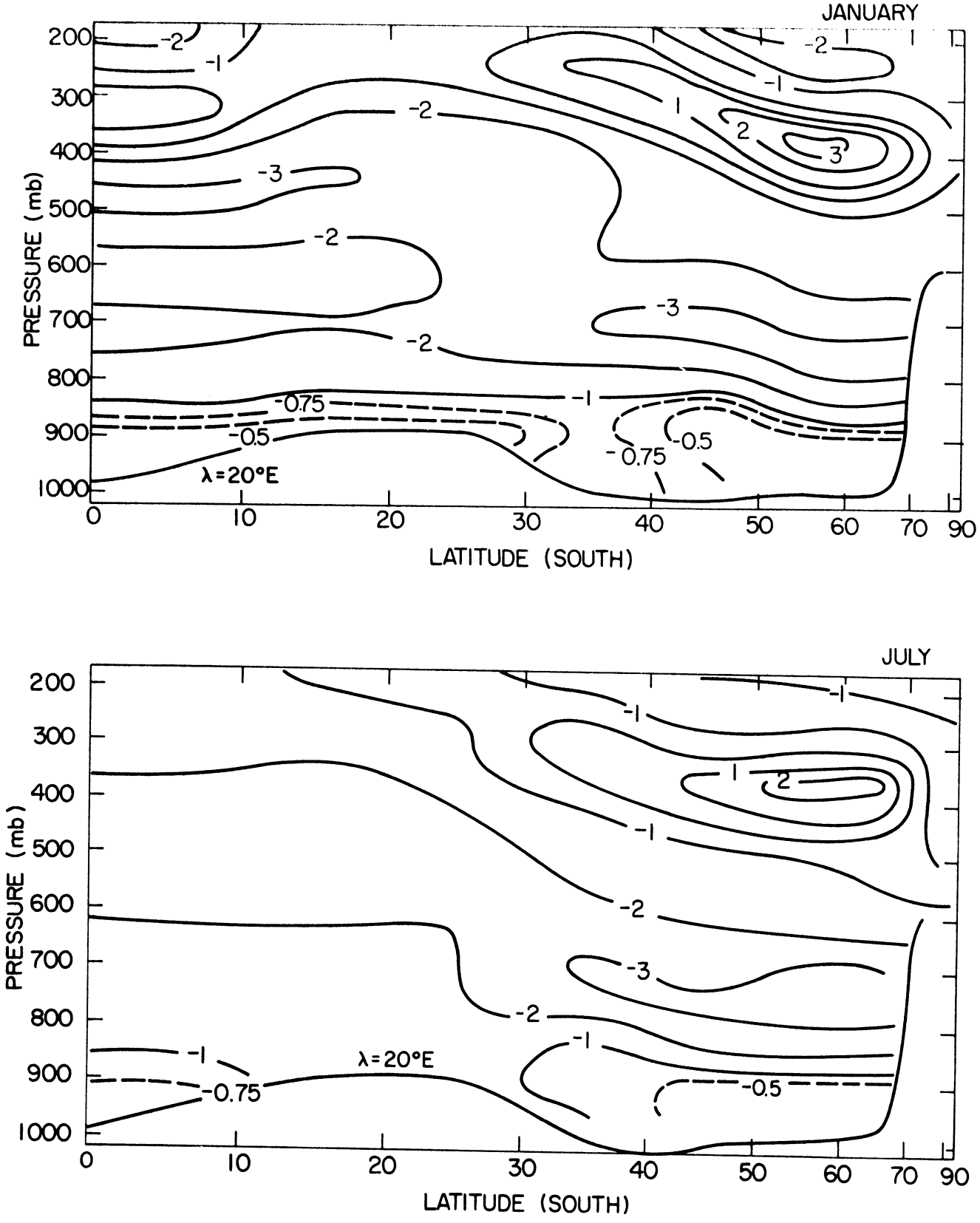

Figure IV-15 Meridional distributions of infrared heating and cooling rates for January and July for a longitude of 20°E

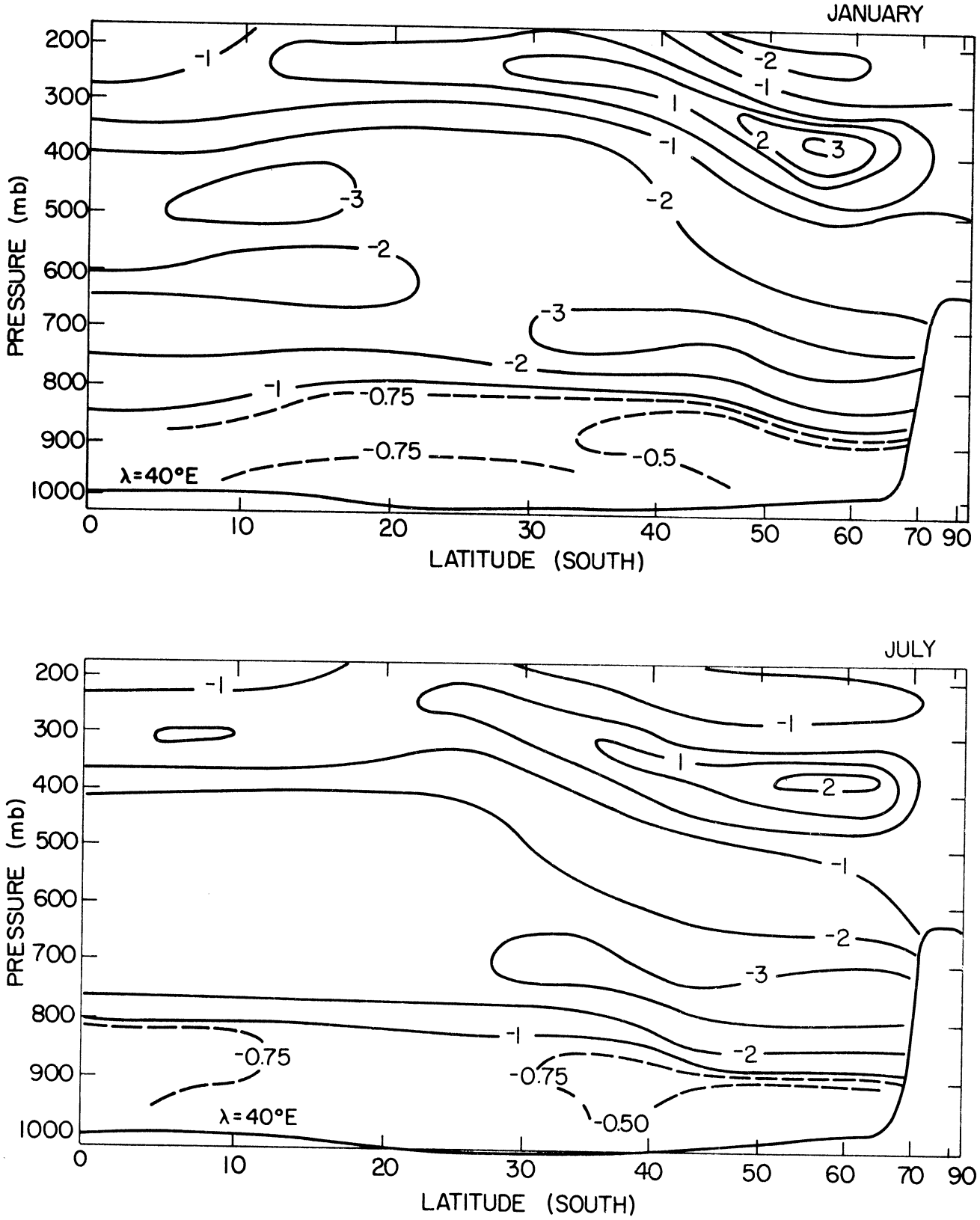

Figure IV-16 Meridional distributions of infrared heating and cooling rates for January and July for a longitude of 40^{o}E

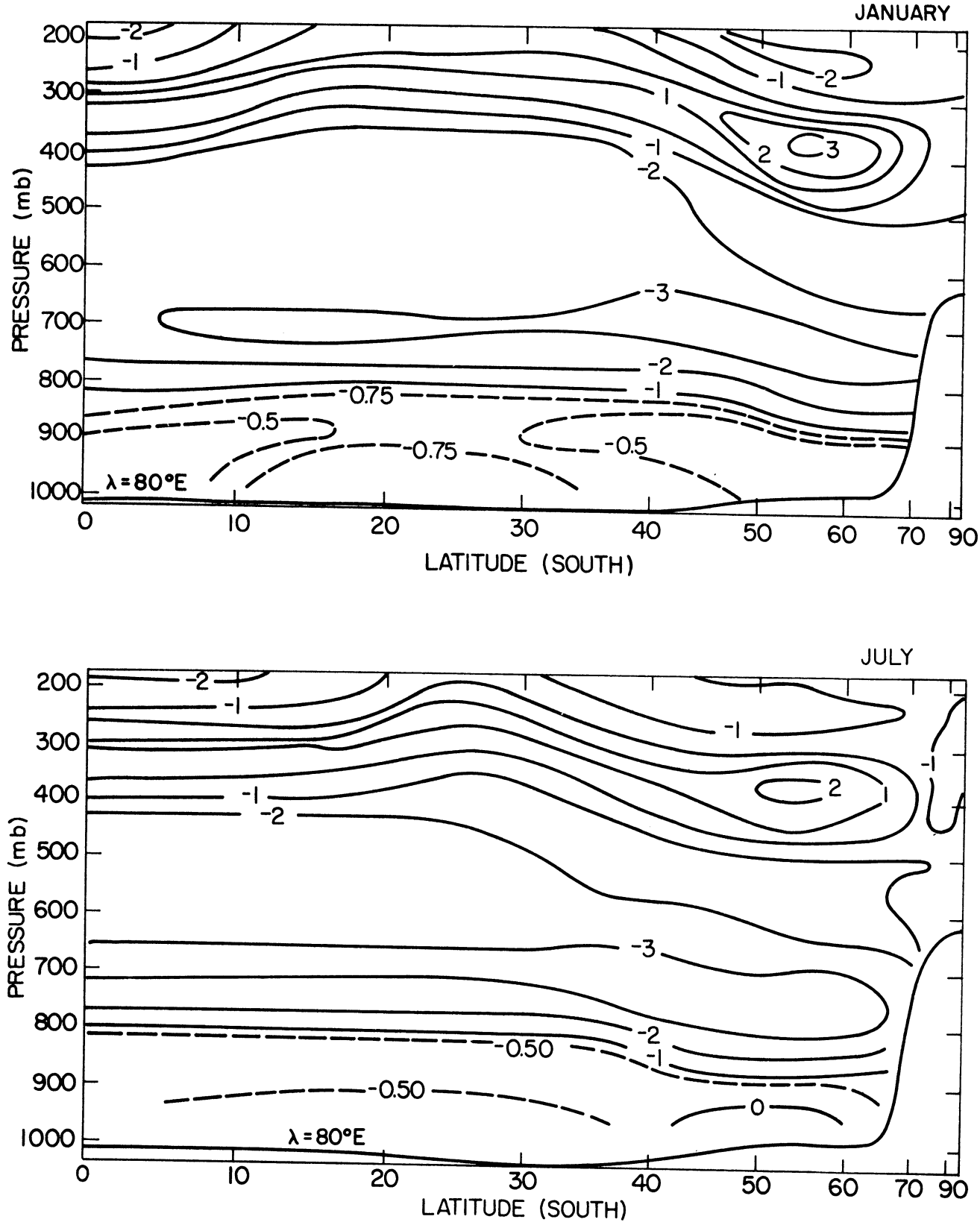

Figure IV-17 Meridional distributions of infrared heating and cooling rates for January and July for a longitude of 80°E

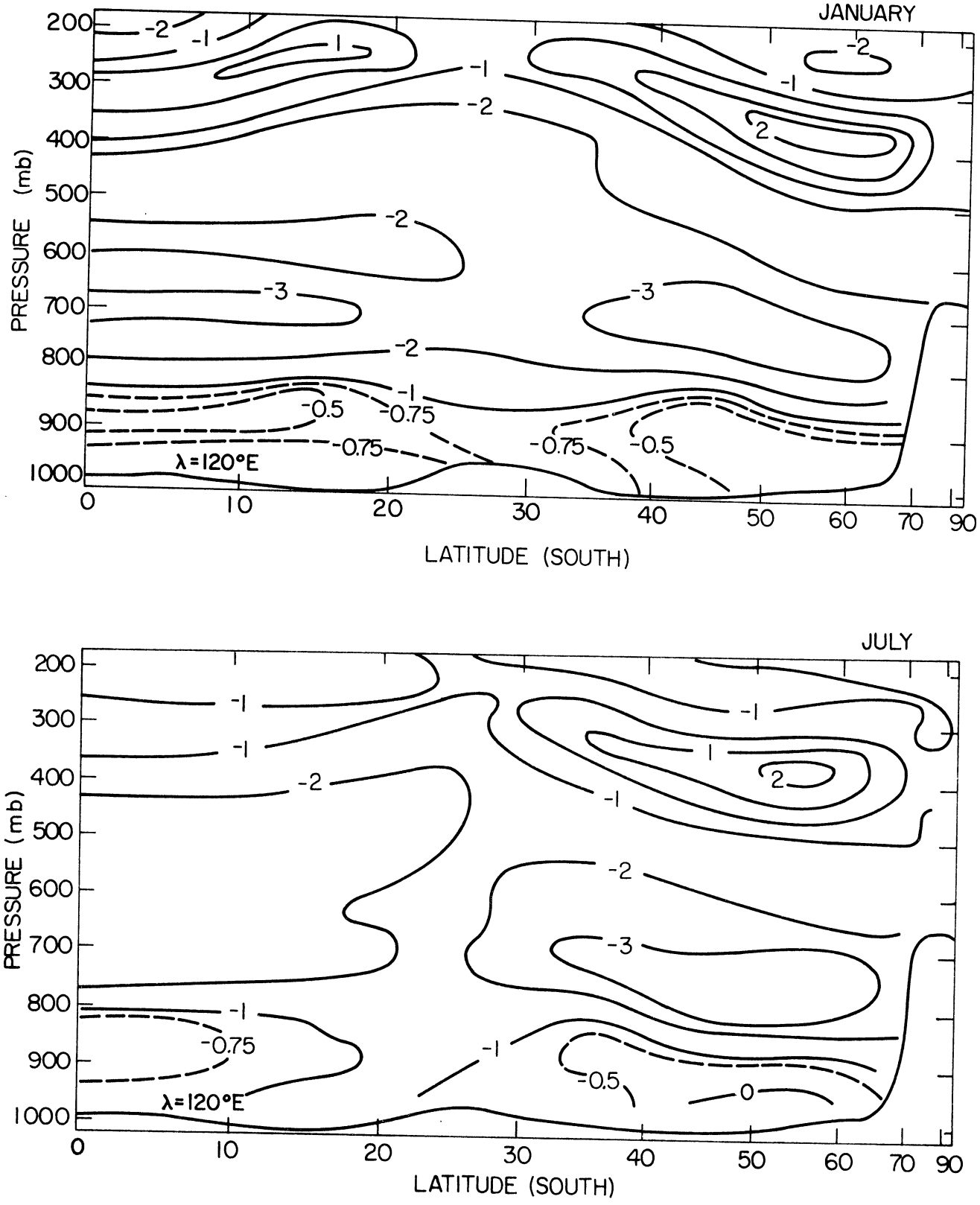

Figure IV-18 Meridional distributions of infrared heating and cooling rates for January and July for a longitude of 120°E

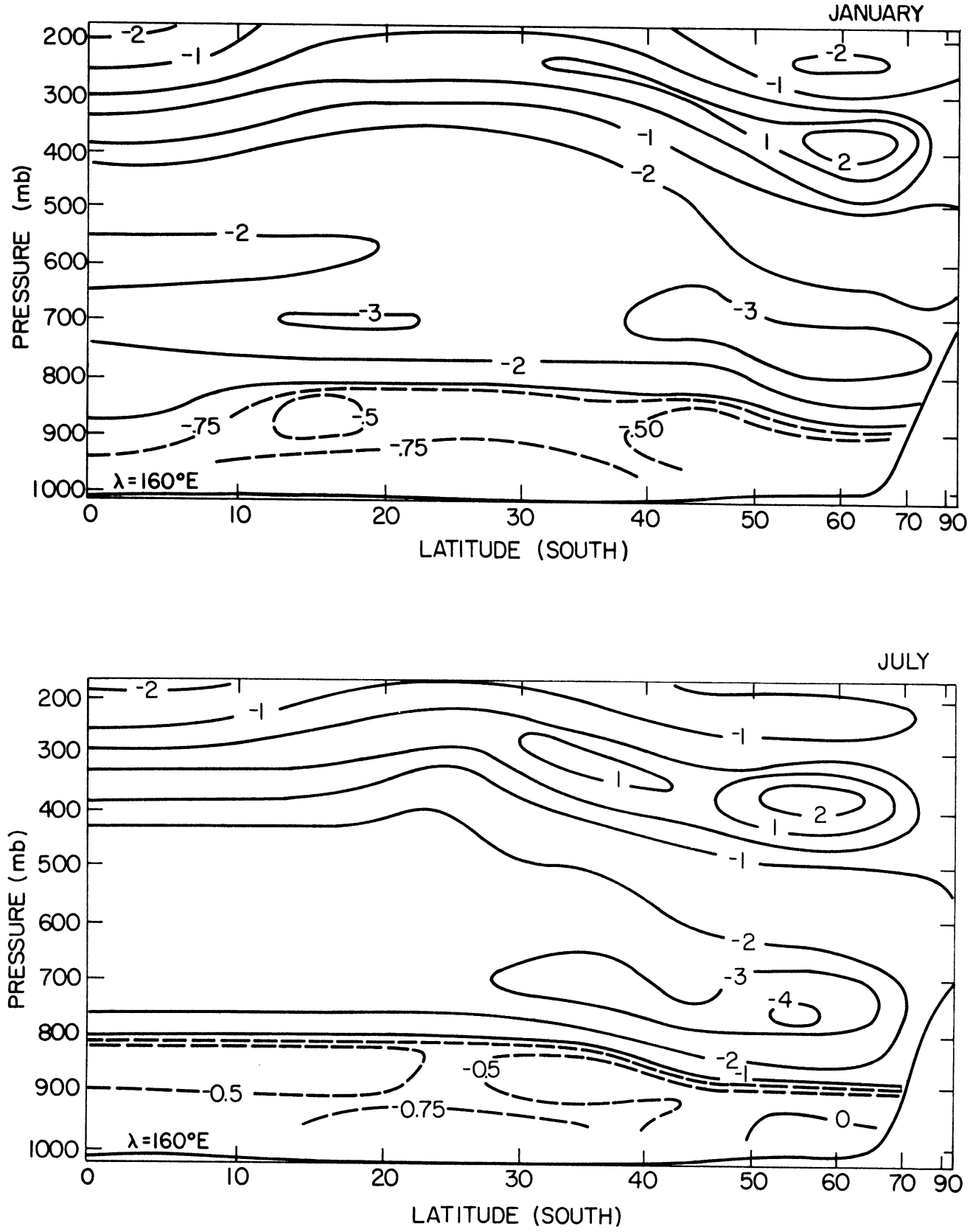

Figure IV-19 Meridional distributions of infrared heating and cooling rates for January and July for a longitude of 160°E

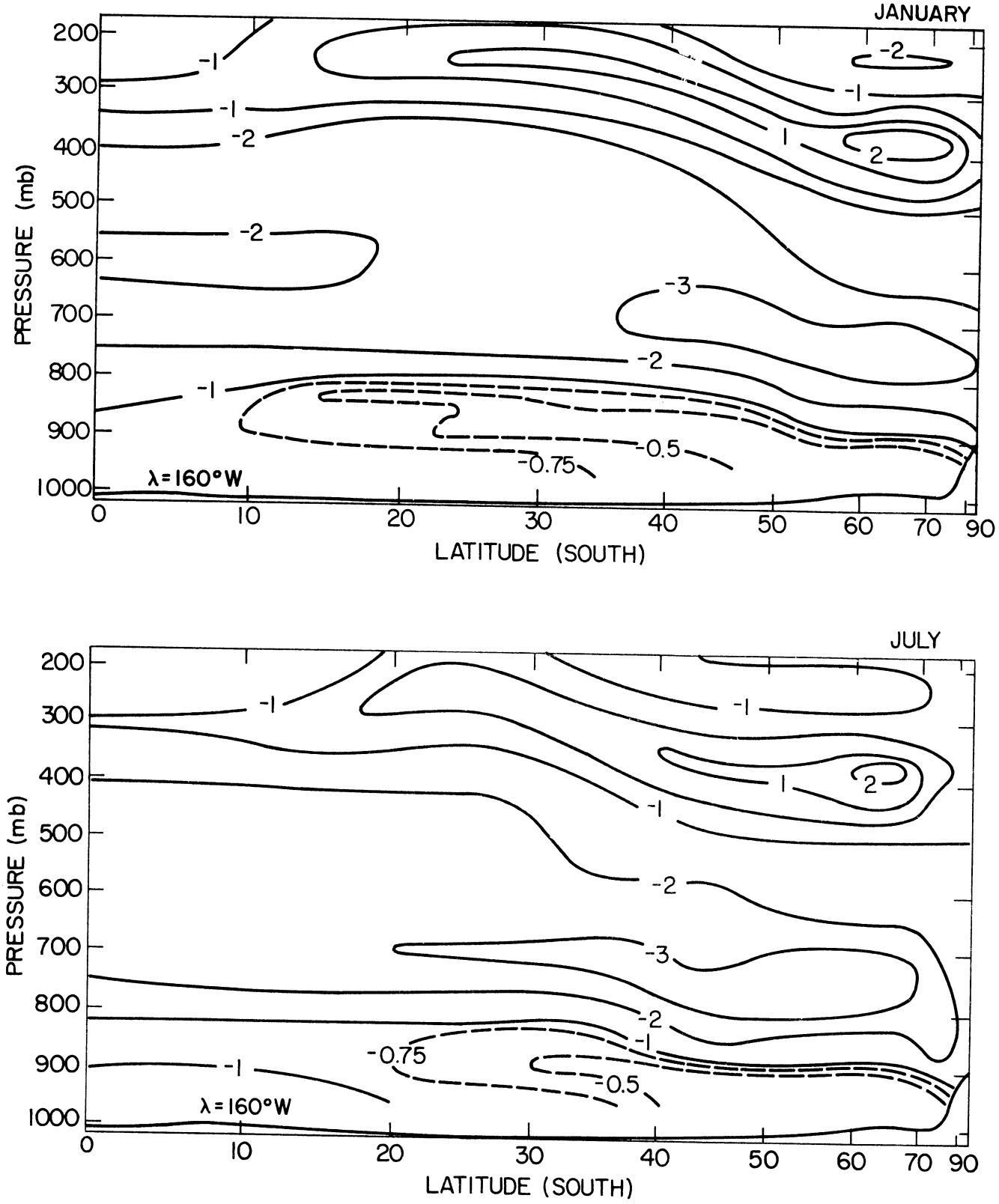

Figure IV-20 Meridional distributions of infrared heating and cooling rates for January and July for a longitude of 160°W

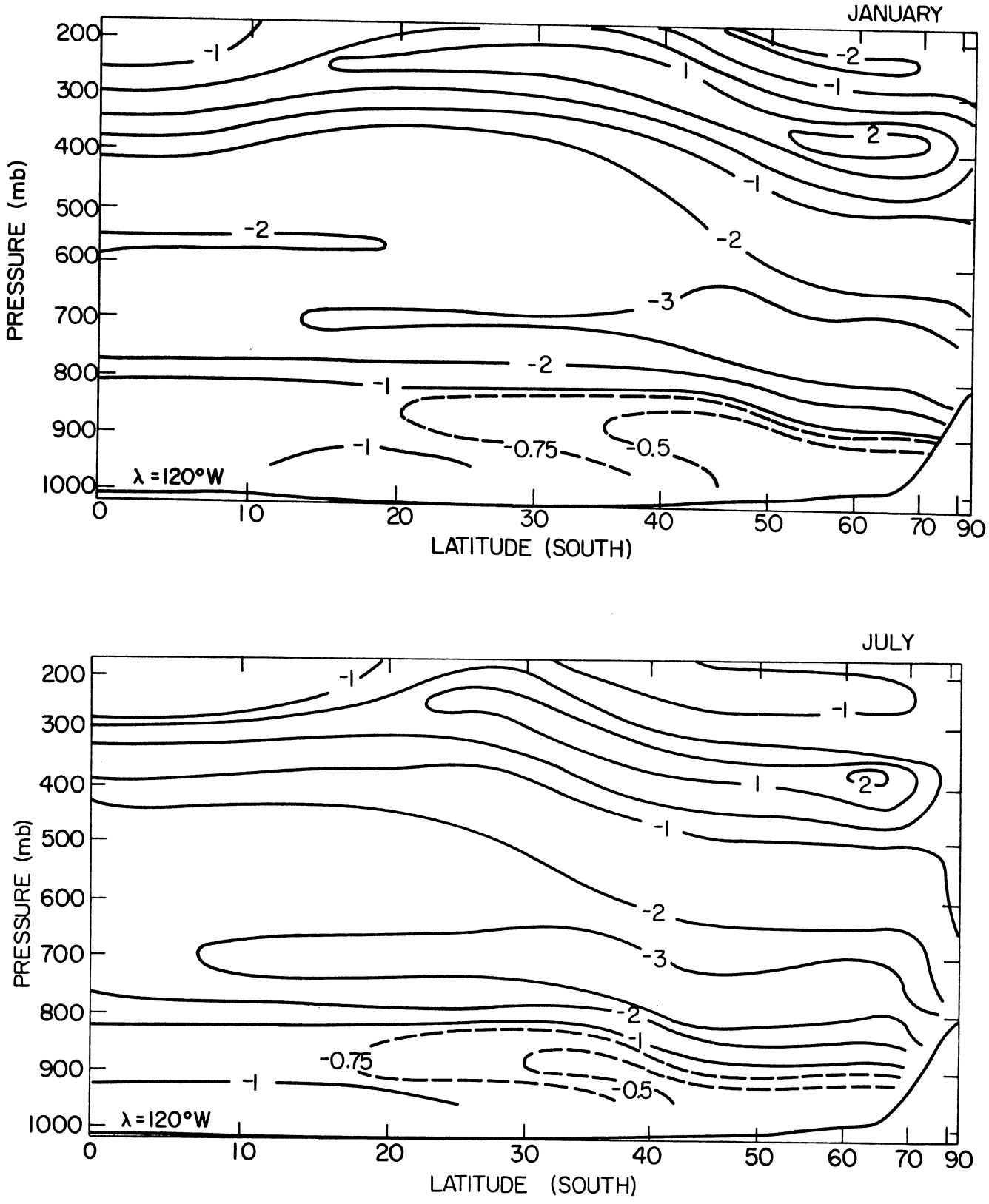

Figure IV-21 Meridional distributions of infrared heating and cooling rates for January and July for a longitude of 120°W

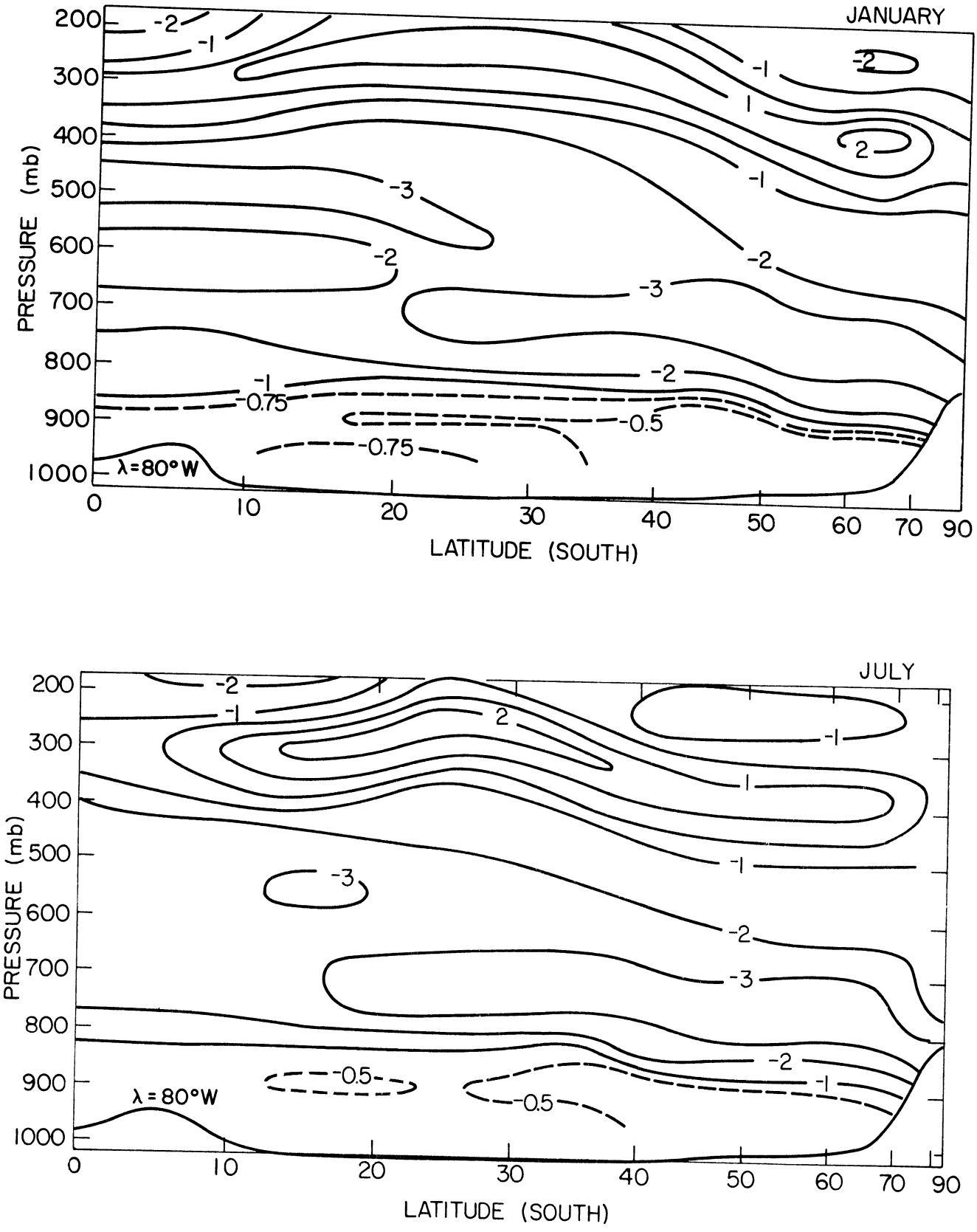

Figure IV-22 Meridional distributions of infrared heating and cooling rates for January and July for a longitude of 80°W

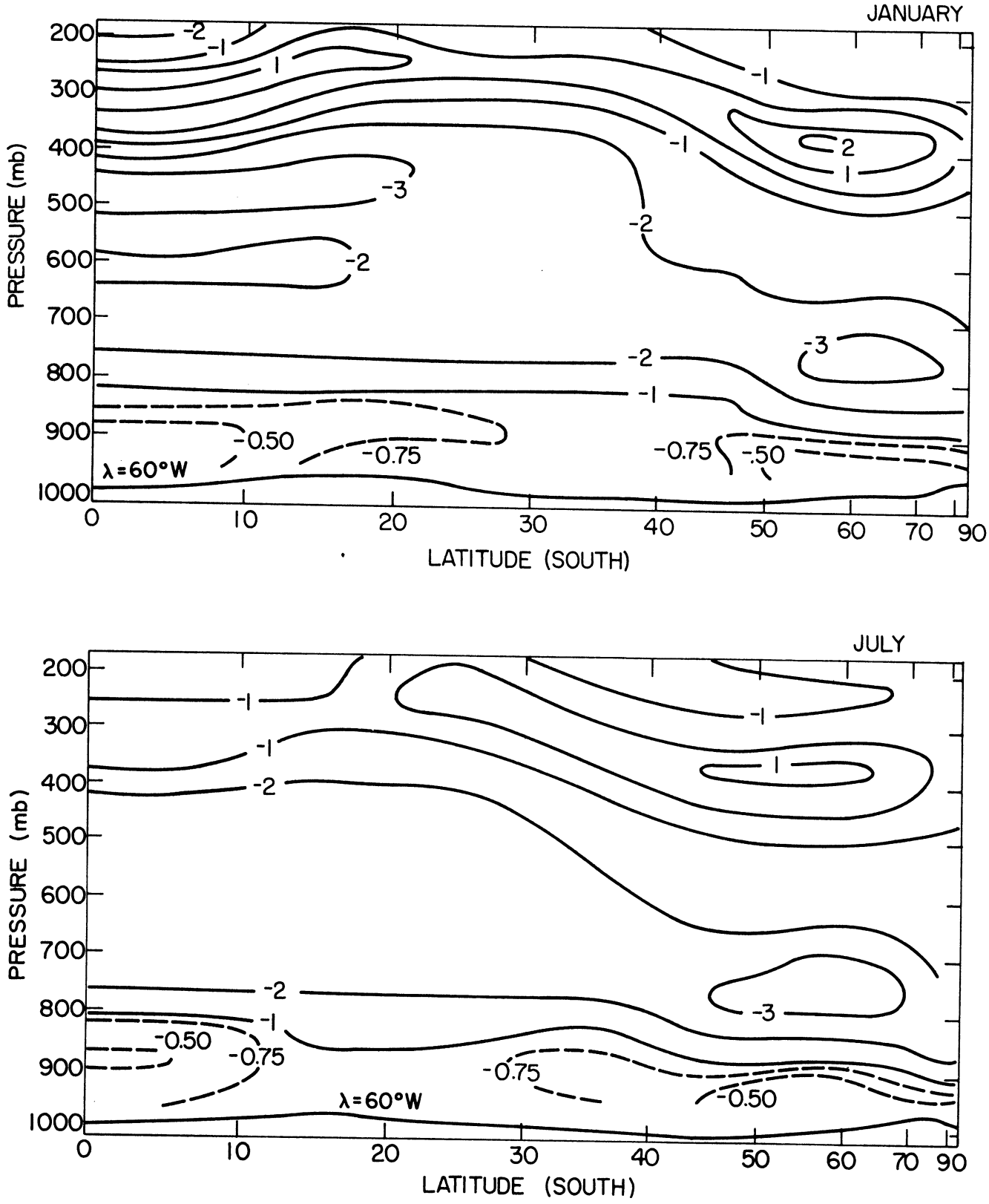

Figure IV-23 Meridional distributions of infrared heating and cooling rates for January and July for a longitude of 60°W

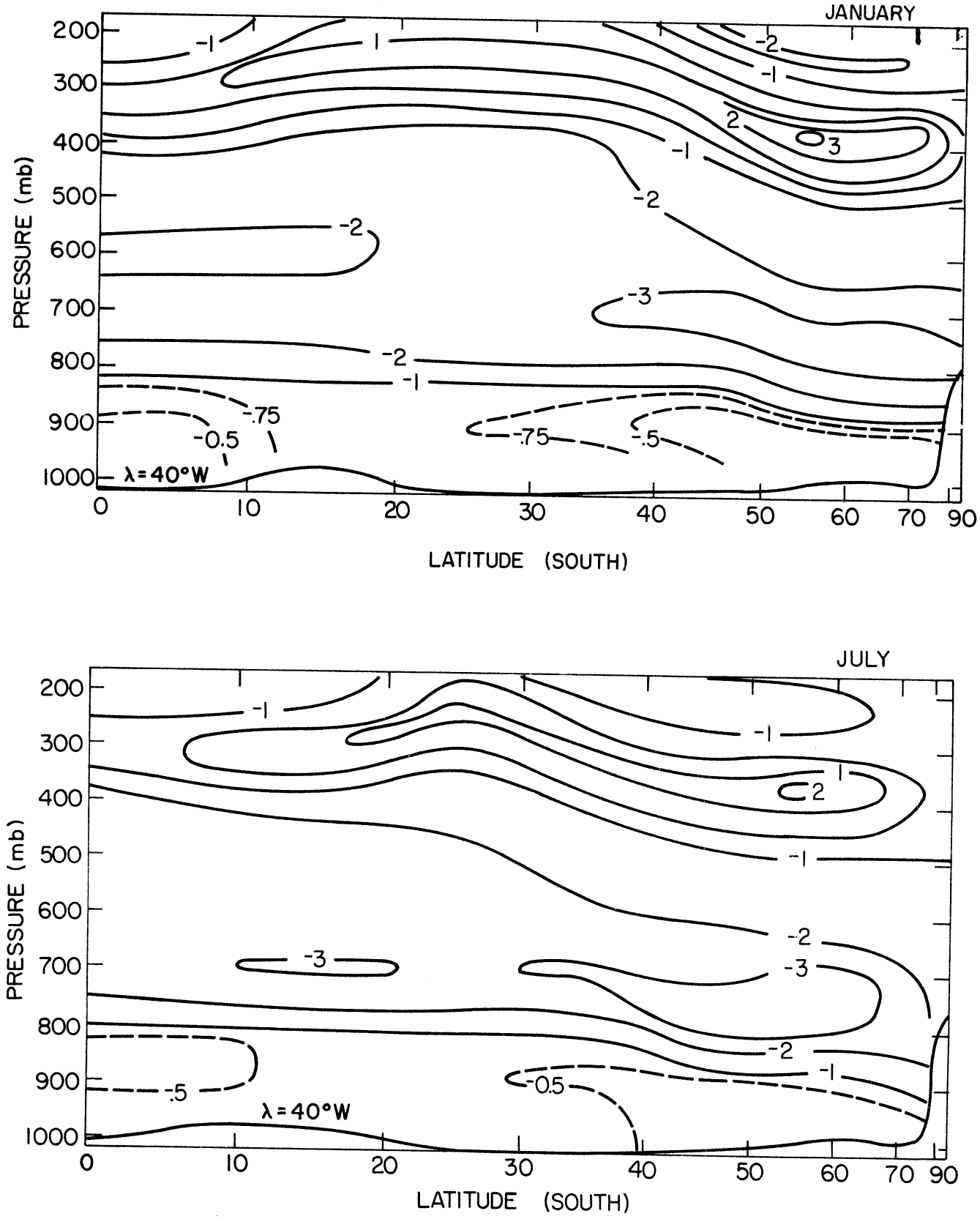

Figure IV-24 Meridional distributions of infrared heating and cooling rates for January and July for a longitude of 40°W

The most serious problems arise because of the lack of information as to the longitudinal variations of cloud heights. The sensitivity of the cooling and heating rates and the fluxes with respect to location and magnitude is already evident in the analyses carried out in the earlier sections of this chapter. It is reasonable to assume that the cloud heights will increase over the continents both because of the greater orographic effect and because of a decrease in the water vapor concentrations over land, but such effects, because of a lack of quantitative information, could not be included in the present results.

Seasonal and latitudinal variations in the cooling rates have already been discussed in terms of the variations found for the zonally averaged meridional cross sections (Section (IV-3)). Except where such variations in the meridional cross sections for the different longitudes reveal effects not evident in the averaged cross sections, no additional comments will be made regarding the latitudinal or seasonal variations.

The maximum heating in January for all longitudes occurs between 55 and 65^{o}S. This region has, because it is the location both of the polar front and the belt of continuous water coverage, the greatest cloud cover in the hemisphere and therefore produces the strong heating. More interesting, however, is the longitudinal variation of this heating. When zonally averaged, the maximum value is 2.8^{o}C per day and is found just below the cirrus deck at 55^{o}S. Table (IV-10) gives the variation in the magnitude of the maximum heating rate with longitude.

TABLE (IV-10)

Variation of the magnitude of the maximum heating (^{O}C per day) with longitude

Longitude	0	40^{O}W	60^{O}W	80^{O}W	120^{O}W	160^{O}W	160^{O}E	120^{O}E	80^{O}E	40^{O}E	20^{O}E
January	3.5	3.3	2.2	2.8	2.8	2.9	2.9	2.9	3.7	3.4	3.4
July	3.0	2.2	1.4	1.9	2.5	2.4	2.9	2.7	2.8	2.4	2.6

The sharp change which occurs between 40 and 60^{O}W lies directly above the narrow channel between Cape Horn and the northernmost extension of Antarctica. The total and cirrus cloud covers (Figure (IV-4)) both show relative minimums in this region, thereby explaining the decrease in warming. No similar explanation is available for the somewhat more gradual change between 120 and 40^{O}E. Above the cirrus layer at the same latitudes there is a region of relatively strong cooling as is to be expected. The variations in the strength of this cooling parallel the variations in the warming, although the changes are smaller.

In the zonally averaged cross sections for January the warming layer below the cirrus deck extends from equator to pole. However this meridional belt of warming does not extend all the way to the equator in the cross sections for 160^{O}W and 40^{O}E, and for the cross sections through 120 and 20^{O}E, warming is found both over the polar and equatorial regions but not around 25^{O}S and 15 to 25^{O}S respectively. In each case these areas coincide with regions of reduced cirrus cover. Also in each case, except at 160^{O}W, the areas are over land.

The variation in the height of the warming also reflects the effect of the cirrus cover. From 15 to 35^{O}S both the warming and the cirrus deck bulge upward. Beyond 35^{O}S and extending to 55^{O}S they both descend

and thereafter they level off. Since longitudinal variations are not present in the cloud height data the same effect is seen in the zonally averaged cross sections.

The structure of the cooling rate patterns in January in the layer between 800 and 500 mb is interesting to examine. Depending on latitude, the tops of As, Cb, St, and low clouds and the bottoms of the As and, to a lesser extent, Ci all influence the cooling which occurs in this layer. In the equatorial region the cooling rates reach local maxima at both 500 and 700 mb with a relative minimum occuring between these two levels. For most longitudes greater cooling is found around 500 mb and only at 80 and 120°E is it greater at 700 mb. The reason for this can be found by noting that the cooling at 500 mb is in great part a function of the As and Cb tops while the cooling at 700 mb is a function of the St and low cloud tops and the As bases. Between 160 and 40°E the cover provided by the St and low clouds nearly doubles and then returns to its original value while the cover due to As and Cb remains approximately constant. The reversal observed in the level of maximum cooling results from the variations in the cover of the two lowest cloud groups. Further toward the pole, this structure disappears and is replaced by a single level of maximum cooling around 700 mb. This change, as already discussed, occurs because the various cloud types, excluding the cirrus, cover a smaller vertical extent, thereby eliminating the finer structure of the double maxima.

In July the location of the region of maximum warming in the layer below the cirrus deck is found between 55 and 65°S as it was in January. It is however, now a little closer to the equator, yet still within the 10° belt. This can also be seen in the zonally averaged cross sections for

January and July. This movement coincides with the seasonal migration of the polar front. The same sharp drop in the strength of the maximum warming occurs around 60°W, as Table (IV-10) indicates and the cooling above the cirrus also follows the same pattern as was described in January.

The warming below the cirrus does differ from that in January at certain longitudes in that it is not as extensive, reaching not as far north toward the equator. This is because the cirrus cover which falls off toward the equator from mid-latitudes in both seasons is not as great in July. Both zonally averaged cooling rate cross sections show that heating occurs just below the cirrus from equator to pole.

The shift in the cirrus heights with latitude is slightly more pronounced in July than in January, rising at 25°S, falling immediately thereafter to 45°S and remaining constant from there to the pole. The warming below the cirrus in July follows this closely.

The cooling rate structure in the mid levels is not as well developed in July. The rather distinct structure of two relative cooling rate maxima surrounding a cooling rate minimum near the equator in January is not evident at 0°W and 20°E and barely evident elsewhere in July. This occurs because the clouds, excluding cirrus, have smaller vertical extent in July than January.

CHAPTER V

DISCUSSION AND SUMMARY

V-1 DISCUSSION

One of the primary reasons for calculating infrared fluxes and heating and cooling rates is to ascertain their contribution to the global heat budget. In this concluding section we shall consider how the infrared fluxes calculated here would alter the heat budgets as derived in various recent studies.

Satellite measurements of the outgoing infrared flux at the top of the atmosphere as analyzed by Rasool and Prabhakara (1966) have already been discussed. That analysis was part of a study of the heat budget of the Southern Hemisphere which also included satellite measurements of the incoming solar radiation and calculated distributions of the storage of heat by the oceans and the net latent heat of the atmosphere. The net heat available for transport by the atmosphere and oceans and the seasonal and annual meridional heat transports values were derived from those quantities.

To the extent that the values of the outgoing flux at the top of the atmosphere as calculated in this work differ from the satellite values used by Rasool and Prabhakara, they suggest different values for the meridional heat transport. However the differences are not large as can be seen from Table (V-1)

TABLE (V-1)

A comparison of zonally averaged outgoing fluxes (ly/day) derived from satellite measurements (Rasool and Prabharka) and as calculated for the stratosphere

January

Latitude S	5^{o}	15^{o}	25^{o}	35^{o}	45^{o}	55^{o}
Present Results	490	492	509	489	459	399
Satellite Results	495	500	510	490	460	425

July

Latitude S	5^{o}	15^{o}	25^{o}	35^{o}	45^{o}	55^{o}
Present Results	521	537	512	481	451	400
Satellite Results	515	524	500	465	440	410

In January the satellite results are negligibly larger except at 55^{o}S where the difference increases to about 6%. In July the differences at each latitude are slightly larger than those in January, varying from about 1 to 3.5% with the present results showing greater values. It should be noted that at 45 and 55^{o}S the satellite results are somewhat uncertain because of the crude extrapolation technique which had to be used to obtain these values from Rasool and Prabhakara's paper.

Only in July is it possible that our values for the outgoing flux might alter Rasool and Prabhakara's conclusions. Our results suggest that in July their values for the radiative balance (the difference between the incoming solar radiation and outgoing terrestrial radiation) should be slightly more negative. In terms of the meridional flux of heat from 60^{o}N to 60^{o}S this means that their transport which is southward south of about 15^{o}N and has a maximum value of about 20×10^{19}

cal day^{-1} at approximately 10^{o}S should be larger in the southern hemisphere.

Rasool and Prabhakara, Vonder Haar and Suomi (1971) and Sasamori et al. (1971) have all estimated the annual meridional heat transport in the southern hemisphere and their values are given in Table (V-2).

TABLE (V-2)

Mean annual heat transport (10^{18}cal day^{-1}) by the atmosphere and oceans in the southern hemisphere

Latitude S	10^{o}	20^{o}	30^{o}	40^{o}	50^{o}	60^{o}	70^{o}	80^{o}
Sasamori et al.	47	86	109	112	94	61	30	7
Vonder Haar & Suomi	47	88	107	107	90	60	30	8
Rasool & Prabhakara	90	120	120	110	90	70	45	25

As already noted the radiative terms in Rasool and Prabhakara's and Vonder Haar and Suomi's calculations are based on satellite observations. Those of Sasamori et al. are calculated from their atmospheric model. Rasool and Prabhakara's results cannot be compared directly to the other's because they include within their transport terms the latent heat and also assume that there is no net storage of heat by the atmosphere, earth, or oceans. Rasool and Prabhakara however treat the latent heat as a separate term in the heat budget and do not force the net storage to be zero.

In the previous chapter (Figure (IV-1)) the annual mean outgoing infrared fluxes used by Vonder Haar and Suomi and Sasamori et al. to calculate their meridional transport values were compared to the fluxes

of this study. Table (IV-3) gives the percentage differences for the annual means.

TABLE (V-3)

Percentage differences between the zonally averaged annual mean outgoing fluxes at the top of the atmosphere. Tabulated values are relative to Sasamori et al. and Vonder Haar and Suomi. Negative values indicate that the present results are smaller.

Latitude S	5^{o}	15^{o}	25^{o}	35^{o}	45^{o}	55^{o}	65^{o}	75^{o}	85^{o}
Present Results vs. Sasamori et al.	-1.7	-1.0	0	-0.8	-1.1	-6.6	0.5	7.8	9.4
Present Results vs. Vonder Haar and Suomi	-4.3	-6.5	-3.4	-4.0	-1.1	-3.9	3.9	16.1	26.4

From the equator to 55^{o}S our outgoing fluxes were found to be smallest. Further toward the pole our values were largest. The result of the smaller energy losses suggested by our results through 55^{o}S will be to increase the total radiation excess (solar minus terrestrial) and therefore to increase the mean annual southward heat transport to values greater than computed by Sasamori et al. and Vonder Haar and Suomi. The reduction however will not be great. For instance in the tropics and subtropics where Vonder Haar and Suomi and Sasamori et al. have fluxes which differ by up to 6%, their transport values show negligible differences. Actually a difference of 6% is probably less than the accuracy which either the observations or calculations can claim.

V-2 SUMMARY

Most global studies of the infrared cooling rates have based their calculations on zonally averaged atmospheric parameters. It is not

immediately clear however that such a procedure will yield the same cooling rates as are found when cooling rates are calculated as a function of longitudinally varying parameters and then zonally averaged. We have shown in these calculations that, even though the transfer equation is not linear in the various atmospheric parameters, the two forms of the zonally averaged cooling rates are effectively identical. This does not mean that there are not significant zonal variations in the cooling rates. A series of meridional cooling rate cross sections at different longitudes show that at a given latitude the same general qualitative cooling and heating rate pattern exists but that quantitative changes occur as the longitude varies. For instance, in the heating layer below the cirrus deck the rates show as much as a 33% decrease when going from water to land. Similar decreases can be seen in the cooling located between 400 and 700 mb although the drop is somewhat smaller, being between 15 and 25%. In terms of heat budget considerations such variations are certainly important.

It is obvious that both the magnitudes and spatial distributions of the heating and cooling rates are critically dependent on the cloud cover. Thus the absence of longitudinal variations in the cloud heights represents an important shortcoming in this analysis. In addition much of the cover for the individual cloud types of the southern hemisphere is taken from northern hemisphere data. Yet one of the major concerns in such a study as this is to compare the radiative budgets of the two hemispheres. This means we are left comparing them when one hemisphere is represented in part by the seasonally transposed data from the other hemisphere. This is clearly not a particularly desirable way to proceed. Unfortunately much the same criticism can be made about the

global calculations of the heat budget and the meridional transport of heat. Hopefully the attempts presently being made to deduce both the cloud heights and amounts from satellite observation will prove fruitful in the near future and provide much of the needed data. It would also be helpful to have additional information as to the degree of overlap between the different cloud types so that a more realistic distribution for the clouds can be adopted.

In addition to carrying out the radiative calculations with better and more extensive cloud data it would be interesting to examine the temporal variation in the radiation budget. Just as the zonally averaged cross sections masked certain variations, temporal averages can be assumed to do the same. Some measure of this can be deduced by comparing values of the outgoing infrared flux as observed by satellites and as calculated in this study. Since the calculated values are derived from climatological values averaged over extended periods of time while the satellites, given their brief existence, yield values which represent shorter time spans, differences in the fluxes represent a possible measure of the information lost in time averaging. In an earlier discussion in this chapter we saw that these differences are on the order of 5% for most latitudes.

Quite probably before any further work of the sort suggested above is done the problem of dealing adequately with the clouds should be considered. Until the various approximations associated with the clouds can either be shown to be legitimate or can be eliminated by improving the cloud model and its data, the uncertainties which arise from these sources may well nullify improvements made in other areas of the infrared radiative transfer problem.

APPENDIX A

Zonally Averaged Climatological Values for Total Cloud Cover, Surface Pressure, Temperature and Water Vapor

Table (A-1)

Zonally Averaged Total Cloud Cover (percent of total sky) for the Southern Hemisphere for January and July

Latitude	January	July
5^{o}	52	45
$15^{o}S$	51	42
$25^{o}S$	48	44
$35^{o}S$	52	55
$45^{o}S$	65	65
$55^{o}S$	82	77
$65^{o}S$	84	76
$75^{o}S$	61	46
$85^{o}S$	52	35

Table (A-2)

Zonally Averaged Surface Pressure (mb) for the Southern Hemisphere for January and July

Latitude	January	July
$5^{o}S$	995.2	997.2
$15^{o}S$	991.9	996.4
$25^{o}S$	997.3	1003.0
$35^{o}S$	1010.3	1012.9
$45^{o}S$	1007.0	1007.1
$55^{o}S$	994.0	995.4
$65^{o}S$	982.4	981.1
$75^{o}S$	811.6	805.0
$85^{o}S$	737.6	728.9

Table (A-3)

Zonally Averaged Temperature (^{o}K) for the Southern Hemisphere in January and July

	5°S		15°S		25°S		35°S		45°S		55°S		65°S		75°S		85°S	
Pressure (mb)	January	July	January	July	January	July	January	July	January	July	January	July	January	July	January	July	January	July
surface	299.5	298.5	298.8	295.8	297.6	291.1	292.7	286.3	285.1	280.7	278.1	274.0	273.0	261.5	254.9	230.7	246.1	222.9
(1)	298.2	296.9	297.6	294.33	296.1	289.5	290.6	284.6	283.1	278.6	276.9	272.6	272.3	261.1	255.9	235.2	249.9	229.1
922.5	295.0	293.4	294.6	291.1	292.8	286.3	287.2	280.9	279.9	275.1	274.2	269.7	270.1	260.0				
857.5	291.3	289.8	291.1	288.0	289.4	283.3	284.6	277.8	277.6	272.3	271.6	266.8	267.2	258.5				
792.5	287.7	286.7	287.7	285.2	286.2	280.5	282.3	274.9	275.7	269.6	269.1	264.0	264.3	256.3				
727.5	284.1	283.5	284.2	282.3	282.9	277.5	279.6	271.5	273.3	266.4	266.1	260.7	260.8	253.7	255.7	242.0		
662.5	280.3	280.0	280.4	278.9	279.2	273.9	276.1	267.3	270.0	262.2	262.2	256.5	256.6	250.0	252.5	243.9	253.3	239.6
597.5	275.9	275.7	276.0	274.7	274.7	269.4	271.5	262.1	265.3	256.9	257.4	251.3	251.6	245.2	247.3	241.3	249.2	241.0
532.5	270.8	270.3	270.8	269.4	269.3	263.9	265.5	255.8	259.2	250.3	251.5	244.9	246.1	239.3	241.1	235.4	240.8	234.4
467.5	264.5	263.7	264.5	262.8	262.6	257.3	258.2	248.6	251.2	242.8	244.8	237.8	240.2	232.7	234.8	228.2	232.0	224.6
402.5	256.9	255.7	256.7	254.7	254.6	249.6	249.6	240.7	243.5	234.8	237.9	230.1	234.4	225.6	229.4	220.7	225.4	215.3
337.5	247.5	246.0	247.3	245.1	245.2	240.9	240.2	232.7	234.9	227.0	231.3	222.7	229.3	218.5	225.6	213.5	222.4	208.3
272.5	236.0	234.6	235.8	234.0	234.3	231.4	230.2	225.1	226.9	220.3	226.0	216.3	225.6	211.9	223.9	207.3	223.4	203.9
207.5	221.9	221.4	222.0	221.3	221.9	221.3	220.5	218.9	220.6	216.0	222.9	211.9	224.4	206.7	224.9	202.1	227.4	200.9
137.5	203.3	205.2	204.1	206.2	206.7	210.3	211.0	214.8	217.1	215.4	223.7	210.8	227.1	203.5	229.5	197.4	232.6	196.1

(1) this pressure is not constant over latitude since it is the pressure in the middle of the atmospheric layer adjacent to the surface.

Table (A-4)

Zonally Averaged Water Vapor Mass Path (gm/cm^2) for the Southern Hemisphere in January and July

	5°S		15°S		25°S		35°S		45°S		55°S		65°S		75°S		85°S	
surface	January	July	January	July	January	July	January	July	January	July	January	July	January	July	January	July	January	July
(1)	.34	.32	.29	.25	.26	.20	.28	.20	.18	.12	.09	.06	.04	.02	.02	.00	.01	.00
955 mb	.31	.30	.27	.23	.24	.19	.25	.18	.16	.11	.08	.06	.04	.02	.02	.00	.01	.00
922.50	.46	.42	.43	.32	.34	.22	.26	.18	.18	.13	.13	.09	.09	.04				
890.0	.41	.37	.39	.28	.30	.20	.23	.15	.16	.11	.13	.09	.08	.04				
857.5	.37	.33	.34	.24	.27	.17	.20	.13	.14	.10	.12	.08	.07	.03				
825.0	.33	.29	.30	.21	.23	.15	.17	.11	.13	.08	.10	.07	.06	.03				
792.5	.30	.26	.27	.18	.21	.13	.15	.10	.11	.07	.08	.05	.06	.03				
760.0	.26	.23	.24	.16	.18	.11	.13	.08	.10	.16	.07	.05	.05	.02				
727.5	.24	.20	.21	.13	.16	.09	.11	.07	.09	.05	.07	.04	.04	.02	.03	.00		
695.0	.21	.17	.19	.11	.13	.08	.10	.06	.07	.05	.06	.03	.04	.02	.02	.01		
662.5	.18	.15	.16	.10	.11	.06	.08	.05	.06	.04	.05	.03	.03	.02	.02	.01	.01	.00
630.0	.16	.13	.14	.08	.10	.05	.07	.04	.06	.03	.04	.02	.03	.01	.02	.01	.01	.00
597.5	.14	.11	.12	.07	.08	.04	.06	.03	.05	.03	.04	.02	.02	.01	.02	.01	.01	.00
565.0	.12	.09	.10	.06	.07	.04	.05	.03	.04	.02	.03	.02	.02	.01	.01	.01	.01	.00
532.5	.10	.08	.08	.04	.06	.03	.04	.02	.03	.02	.03	.01	.02	.01	.01	.01	.01	.00
500.0	.08	.06	.07	.04	.04	.02	.03	.02	.03	.01	.02	.01	.01	.01	.01	.01	.01	.00
467.5	.07	.05	.06	.03	.03	.02	.03	.01	.02	.01	.02	.01	.01	.01	.01	.01	.01	.00
435.0	.05	.04	.04	.02	.03	.01	.02	.01	.02	.01	.01	.01	.01	.00	.01	.01	.00	.00
402.5	.04	.03	.03	.02	.02	.01	.02	.01	.01	.01	.01	.00	.01	.00	.01	.00	.00	.00
370.0	.03	.02	.02	.01	.02	.01	.01	.01	.01	.00	.01	.00	.01	.00	.00	.00	.00	.00
337.5	.02	.02	.02	.01	.01	.01	.01	.00	.01	.00	.01	.00	.00	.00	.00	.00	.00	.00
305.0	.01	.01	.01	.01	.01	.00	.01	.00	.01	.00	.00	.00	.00	.00	.00	.00	.00	.00
272.5	.01	.01	.01	.00	.01	.00	.00	.00	.00	.00	.00	.00	.00	.00	.00	.00	.00	.00
240.0	.01	.00	.00	.00	.00	.00	.00	.00	.00	.00	.00	.00	.00	.00	.00	.00	.00	.00
207.5	.00	.00	.00	.00	.00	.00	.00	.00	.00	.00	.00	.00	.00	.00	.00	.00	.00	.00
175.0	.00	.00	.00	.00	.00	.00	.00	.00	.00	.00	.00	.00	.00	.00	.00	.00	.00	.00
137.5	.00	.00	.00	.00	.00	.00	.00	.00	.00	.00	.00	.00	.00	.00	.00	.00	.00	.00
100.0																		

(1) This is the pressure in the middle of the layer adjacent to the surface

APPENDIX B

Regression Coefficients for Median Line Intensities and Numbers of Lines per Decade

The tables in this appendix give the regression coefficients for the median line intensities and number of lines per decade for each of the nine water vapor and five carbon dioxide subintervals. There are five decades per subinterval. The equations used for the water vapor are fifth order and those for carbon dioxide, fourth order.

The median line intensities are formed from the line intensities as given in the following expression

$$XO = \frac{S(T)}{\pi \alpha_O}$$

where S(T) is the line intensity (cm/gm) at temperature T and α_O the half width at standard temperature and pressure. The units of XO are cm^2/gm

XNO represents the number of lines per decade for a subinterval.

TABLE (B-1)

Water Vapor

0-220 cm^{-1}

Regression coeff. for XO

-0.1846691E 07	0.4202810E 05	-0.3657153E 03	0.1559053E 01	0.3264469E -02	0.2689640E -05
-0.1594461E 06	0.3529347E 04	-0.2965894E 02	0.1211852E 00	0.2411983E -03	0.1874379E -06
-0.2499924E 05	0.5583486E 03	-0.4799854E 01	0.2007645E -01	0.4091248E -04	0.3255466E -07
-0.8279087E 03	0.1855388E 02	-0.1585286E 00	0.6677827E -03	0.1388624E -05	0.1142482E -08
-0.1021565E 03	0.2425858E 01	-0.2163580E -01	0.9347097E -04	0.1957079E -06	0.1593764E -09

Regression coeff. for XNO

-0.5797260E 02	0.2067563E 01	-0.1860116E -01	0.8823308E -04	0.1972959E -06	0.1641025E -09
0.1065142E 04	-0.2456136E 02	0.2236084E 00	-0.9690719E -03	0.2013986E -05	-0.1608205E -08
0.8388960E 03	-0.1547926E 02	0.1164979E 00	-0.4245499E -03	0.7668064E -06	-0.5579486E -09
-0.3602044E 00	-0.2639742E 01	0.6475288E -01	-0.4612494E -03	0.1373240E -05	-0.1476923E -08
-0.4009399E 04	0.9719807E 02	-0.9131598E 00	0.4217554E -02	0.9538832E -05	0.8434871E -08

220-440 cm^{-1}

Regression coeff. for XO

0.6721882E 06	-0.1061326E 05	0.5282986E 02	-0.3526405E -01	0.3504297E -03	0.6495180E -06
0.6025988E 05	-0.1909938E 04	0.2228384E 02	-0.1197265E 00	0.3030414E -03	-0.2925292E -06
0.7852563E 04	-0.2054410E 03	0.2131079E 01	-0.1059815E -01	0.2427962E -04	-0.2331569E -07
0.2363981E 04	-0.5476201E 02	0.4973642E 00	-0.2190720E -02	0.4688774E -05	-0.3908266E -08
-0.1494545E 03	0.3664845E 01	-0.3470309E -01	0.1611098E -03	0.3655078E -06	0.3242664E -09

Regression coeff. for XNO

0.2327843E 04	-0.5356067E 02	0.4848890E 00	-0.2150172E -02	0.4682143E -05	-0.4004100E -08
-0.3039838E 04	0.7070882E 02	-0.6433594E 00	0.2874070E -02	0.6285127E -05	0.5382560E -08
-0.1954870E 04	0.4484329E 02	-0.4023601E 00	0.1785361E -02	0.3897808E -05	0.3347692E -08
0.1721088E 04	-0.4094357E 02	0.3884776E 00	-0.1802312E -02	0.4108158E -05	-0.3675897E -08
-0.4862124E 03	0.1172975E 02	-0.1114365E 00	0.5533798E -03	0.1369883E -05	0.1312820E -08

440-800 cm^{-1}

Regression coeff. for XO

0.1859552E 06	-0.4232234E 04	0.3736835E 02	-0.1600581E 00	0.3342486E -03	-0.2730929E -06
0.3913419E 05	-0.8646577E 03	0.7405406E 01	-0.3079661E -01	0.6260052E -04	-0.5000172E -07
0.4603246E 04	-0.1015180E 03	0.8687552E 00	-0.3614160E -02	0.7355241E -05	-0.4884667E -08
0.6793374E 03	-0.1503973E 02	0.1294320E 00	-0.5420276E -03	0.1109145E -05	-0.8899050E -09
0.1031792E 03	-0.2309516E 01	0.2017178E -01	-0.8605434E -04	0.1798770E -06	-0.1476696E -09

Regression coeff. for XNO

-0.5225152E 04	0.1172092E 03	-0.1023982E 01	0.4368689E -02	0.9123728E -05	0.7483074E -08
-0.1185031E 04	0.2536520E 02	-0.2088487E 00	0.8428344E -03	0.1670489E -05	0.1312820E -08
-0.1037080E 05	0.2341372E 03	-0.2065768E 01	0.8980739E -02	0.1892586E -04	0.1575384E -07
-0.7550355E 04	0.1646627E 03	-0.1392464E 01	0.5746003E -02	0.1156438E -04	0.9091281E -08
0.4522734E 04	-0.9796188E 02	0.8283311E 00	-0.3386125E -02	0.6735289E -05	-0.5251280E -08

800-1250 cm^{-1}

Regression coeff. for XO

0.8095054E 03	-0.1746053E 02	0.1467199E 00	-0.6075958E -03	0.1269435E -05	-0.1081009E -08
0.1373843E 04	-0.3189207E 02	0.2892601E 00	-0.1281884E -02	0.2780691E -05	-0.2365866E -08
0.1077897E 03	-0.2430799E 01	0.2142401E -01	-0.9235382E -04	0.1952331E -06	-0.1622360E -09
0.8190247E 01	-0.1838939E 00	0.1610609E -02	-0.6886916E -05	0.1442312E -07	-0.1186190E -10
0.7767925E 00	-0.1745440E -01	0.1527461E -03	-0.6515547E -06	0.1359501E -08	-0.1112600E -11

Regression coeff. for XNO

-0.3658528E 04	0.8306059E 02	-0.7389325E 00	0.3227981E -02	0.6935196E -05	0.5874870E -08
-0.1642484E 05	0.3770791E 03	-0.3206856E 01	0.1371758E -01	0.2877240E -04	0.2372923E -07
-0.1390764E 05	0.3085901E 03	-0.2669709E 01	0.1129657E -01	0.2338797E -04	0.1900307E -07
-0.7852109E 04	0.1754142E 03	-0.1508238E 01	0.6305508E -02	0.1279440E -04	0.1010872E -07
-0.2018557E 05	0.4564768E 03	-0.4033004E 01	0.1748997E -01	0.3715989E -04	0.3091692E -07

1250-1420 cm^{-1}

Regression coeff. for XO

0.9074219E 05	-0.2003149E 02	-0.1765219E 02	0.1484069E 00	0.4423410E -03	0.4508553E -06
-0.1080449E 06	0.2862568E 04	-0.2891946E 02	0.1395050E 00	0.3214148E -03	0.2844783E -06
-0.3326627E 05	0.8245725E 03	-0.7960985E 01	0.3735383E -01	0.8504197E -04	0.7526825E -07
0.2933057E 03	0.6664667E 00	-0.7252419E -01	0.5975608E -03	0.1821932E -05	0.1927778E -08
0.8622537E 02	-0.1533993E 01	0.9784602E -02	-0.2604074E -04	0.2268072E -07	0.6015999E -11

Regression coeff. for XNO

0.1084339E 04	-0.2715511E 02	0.2636508E 00	-0.1235496E -02	0.2799439E -05	-0.2461538E -08
0.5237095E 03	-0.1687054E 02	0.1950172E 00	-0.1033268E -02	0.2568951E -05	-0.2428718E -08
-0.1193680E 04	0.2379321E 02	-0.1795750E 00	0.6529510E -03	0.1136410E -05	0.7548715E -09
-0.4443832E 04	0.8218513E 02	-0.5475097E 00	0.1618443E -02	0.1956922E -05	0.5251277E -09
0.2450144E 04	-0.8972357E 02	0.1123966E 01	-0.6246150E -02	0.1600037E -04	-0.1542564E -07

1420-1590 cm^{-1}

Regression coeff. for XO

0.1129935E 07	-0.2588045E 05	0.2356907E 03	-0.1047381E 01	0.2269900E -02	-0.1921640E -05
0.1950850E 06	-0.3725587E 04	0.2820357E 02	-0.1039981E 00	0.1867144E -03	-0.1304286E -06
-0.6950150E 05	0.1568924E 04	-0.1381014E 02	0.5957452E -01	0.2160989E -03	0.1049108E -06
0.1097310E 02	0.4213526E 01	-0.7159799E -01	0.4524838E -03	0.1246201E -05	0.1262277E -08
0.2703264E 02	-0.5422599E 00	0.4848208E -02	-0.2177589E -04	0.4852811E -07	-0.4260099E -10

Regression coeff. for XNO

-0.5574556E 03	0.1310321E 02	-0.1175700E 00	0.5152447E -03	0.1100979E -05	0.9189740E -09
0.1326707E 04	-0.3043631E 02	0.2773251E 00	-0.1228186E -02	0.2662564E -05	-0.2264615E -08
-0.1635644E 04	0.3691202E 02	-0.3248212E 00	0.1413333E -02	0.3030303E -05	0.2560000E -08
0.2507004E 03	-0.9025195E 01	0.1158923E 00	-0.6348251E -03	0.2847180E -05	-0.1476923E -08
-0.8967456E 03	0.2750409E 02	-0.2762437E 00	0.1303189E -02	0.2847180E -05	0.2330256E -08

1590-1845 cm^{-1}

Regression coeff. for XO

0.5572864E 06	-0.1135813E 05	0.9324341E 02	-0.3713173E 00	0.7166730E -03	-0.5366153E -06
0.3282787E 06	-0.7425137E 04	0.6608109E 02	-0.2860236E 00	0.6028109E -03	-0.4960163E -06
-0.1637282E 05	0.3329387E 03	-0.2607360E 01	0.1005631E -01	0.1916739E -04	0.1448697E -07
0.1510807E 04	-0.3545833E 02	0.3309505E 00	-0.1506194E -02	0.3343044E -05	-0.2899692E -08
0.1968402E 02	-0.4035146E 00	0.3857298E -02	-0.1796722E -04	0.4033827E -07	-0.3478970E -10

Regression coeff. for XNO

-0.4675984E 03	0.1044930E 02	-0.8550602E -01	0.3334545E -03	0.6157575E -06	0.4266665E -09
-0.2124726E 03	0.5538230E 01	-0.5246782E -01	0.2575663E -03	0.6239626E -06	0.5907690E -09
-0.1782428E 04	0.4353809E 02	-0.4079713E 00	0.1870144E -02	0.4178274E -05	0.3643076E -08
0.2080376E 04	-0.4852982E 02	0.4520717E 00	-0.2029995E -02	0.4411375E -05	-0.3708717E -08
-0.2390966E 04	0.5558661E 02	-0.4788046E 00	0.1975356E -02	0.3834031E -05	0.2789743E -08

1845-2100 cm^{-1}

Regression coeff. for XO

0.3601468E 05	-0.8103362E 03	0.7204515E 01	-0.3019533E -01	0.6000558E -04	-0.4535794E -07
0.1592755E 05	-0.3820271E 03	0.3564268E 01	-0.1600960E -01	0.3483442E -04	-0.2952533E -07
-0.9847842E 03	0.2997733E 02	-0.3254181E 00	0.1650132E -02	0.3961529E -05	0.3639794E -08
-0.1945272E 03	0.4548924E 01	-0.4066433E -01	0.1769147E -03	0.3759727E -06	0.3130747E -09
0.2842686E 02	-0.6562307E 00	0.5959366E -02	-0.2631660E -04	0.5658852E -07	-0.4751749E -10

Regression coeff. for XNO

-0.6760867E 03	0.1535226E 02	-0.1363135E 00	0.5932492E -03	0.1261725E -05	0.1050256E -08
0.8188779E 03	-0.1960823E 02	0.1856360E 00	-0.8544985E -03	0.1917389E -05	-0.1673846E -08
0.2258036E 04	-0.5031354E 02	0.4344752E 00	-0.1810452E -02	0.3674778E -05	-0.2921025E -08
-0.7291968E 03	0.1754291E 02	-0.1584727E 00	0.7019392E -03	0.1512726E -05	0.1280000E -08
-0.4421285E 04	0.9611700E 02	-0.8065158E 00	0.3304624E -02	-0.6611467E -05	0.5218460E -08

2100-2450 cm^{-1}

Regression coeff. for XO

-0.8834988E 04	0.2030949E 03	-0.1826583E 01	0.8032840E -02	0.1727704E -04	0.1455695E -07
-0.5355388E 03	0.1225305E 02	-0.1091492E 00	0.4729694E -03	0.9968480E -06	0.8190257E -09
-0.5138023E 02	0.1190042E 01	-0.1076263E -01	0.4750361E -04	0.1023442E -06	0.8626440E -10
-0.7996741E 01	0.1847219E 00	-0.1667752E -02	0.7353366E -05	0.1583342E -07	0.1333990E -10
-0.9728098E 00	0.2250925E -01	-0.2036675E -03	0.9005553E -03	0.1946279E -08	0.1647600E -11

Regression coeff. for XNO

0.8050918E 04	-0.1836171E 03	0.1635864E 01	-0.7115595E -02	0.1513100E -04	-0.1260307E -07
0.8858110E 03	-0.2112990E 02	0.1921123E 00	-0.8246524E -03	0.1685034E -05	-0.1312820E -08
0.3637418E 05	-0.8244546E 03	0.7307886E 01	-0.3167022E -01	0.6720744E -04	-0.5592615E -07
0.2627978E 05	-0.6142185E 03	0.5592192E 01	-0.2478514E -01	0.5367196E -04	-0.4552205E -07
-0.1494003E 05	0.3301641E 03	-0.2853599E 01	0.1211675E -01	0.2516810E -04	0.2041436E -07

TABLE (B-2)

Carbon Dioxide

500-555 cm^{-1}

Regression coeff. for XO

-0.1506991E 02	0.2818727E 00	-0.1953035E -02	0.5925949E -05	-0.6613217E -08
-0.1947492E 01	0.4085107E -01	-0.3134226E -03	0.1039970E -05	-0.1253006E -08
0.3296369E 00	-0.5616188E -02	0.3530119E -04	-0.9736931E -07	0.1002441E -09
-0.4985421E -01	0.9571086E -03	-0.6777965E -05	0.2090272E -07	-0.2354220E -10
0.3945875E 01	-0.7313114E -01	0.5040579E -03	-0.1531719E -05	0.1732048E -08

Regression coeff. for XNO

0.9409883E 04	-0.1657420E 03	0.1086589E 01	-0.3135704E -02	0.3360000E -05
-0.7725844E 04	0.1349940E 03	-0.8727000E 00	0.2480889E -02	-0.2613333E -05
-0.4484126E 02	0.2721164E 01	-0.3204444E -01	0.1434074E -03	-0.2133333E -06
0.1817611E 04	-0.3195517E 02	0.2107555E 00	-0.6068146E -03	0.6400000E -06
-0.3552639E 04	0.6329814E 02	-0.4126778E 00	0.1171852E -02	-0.1226666E -05

555-610 cm^{-1}

Regression coeff. for XO

-0.1129124E 04	0.2704254E 02	-0.2265410E 00	0.7999563E -03	-0.9909227E -06
0.1341698E 04	-0.1652357E 02	0.5820078E -01	-0.1970430E -04	-0.1301264E -06
0.7611508E 01	-0.2188816E -02	-0.8637372E -03	0.4870819E -05	-0.7183466E -08
-0.3979716E 01	0.1182440E 00	-0.1100835E -02	0.4116325E -05	-0.5342354E -08
-0.2511078E 01	0.4890425E -01	-0.3496772E -03	0.1084913E -05	-0.1225544E -08

Regression coeff. for XNO

-0.6554563E 03	0.9402487E 01	-0.4625555E -01	0.9037036E -04	-0.5333333E -07
0.5321904E 03	-0.8364602E 01	0.4820000E -01	-0.1191111E -03	0.1066667E -06
-0.1772340E 05	0.2693269E 03	-0.1480088E 01	0.3497481E -02	-0.2986667E -05
0.1705003E 05	-0.2742629E 03	0.1640455E 01	-0.4309036E -02	0.4213332E -05
-0.7201422E 04	0.1271300E 03	-0.8369443E 00	0.2462518E -02	-0.2719999E -05

610-667 cm^{-1}

Regression coeff. for XO

0.5761926E 06	-0.8795391E 04	0.5042094E 02	-0.1274464E 00	0.1198213E -03
0.9604632E 06	-0.1561146E 05	0.9445090E 02	-0.2521081E 00	0.2505567E -03
0.2308947E 05	-0.3746431E 03	0.2267640E 01	-0.6060790E -02	0.6035589E -05
0.4808426E 04	-0.7822469E 02	0.4737273E 00	-0.1265226E -02	0.1257741E -05
0.5793274E 03	-0.9401036E 01	0.5683779E -01	-0.1516732E -03	0.1507641E -06

Regression coeff. for XNO

-0.2254246E 04	0.3594719E 02	-0.2117110E 00	0.5505183E -03	-0.5333333E -06
-0.1665492E 04	0.2928105E 02	-0.1940889E 00	0.5783702E -03	-0.6400000E -06
-0.2611140E 05	0.3262559E 03	-0.1958266E 01	0.5191110E -02	-0.5120000E -05
0.1159671E 04	-0.2050058E 02	0.1392556E 00	-0.3837035E -03	0.3733333E -06
-0.7705930E 04	0.1263590E 03	-0.7557222E 00	0.1996148E -02	-0.1973332E -05

668-723 cm^{-1}

Regression coeff. for XO

0.9449488E 05	-0.1462800E 04	0.1003999E 02	-0.3111828E -01	0.3597866E -04
-0.1460547E 06	0.2578918E 04	-0.1642490E 02	0.4611710E -01	-0.4809012E -04
0.7108000E 05	-0.1176975E 04	0.7251526E 01	-0.1967339E -01	0.1985152E -04
0.9704700E 03	-0.1884222E 02	0.1380765E 00	-0.4391156E -03	0.5104000E -06
0.5483257E 03	-0.8448473E 01	0.4746444E -01	-0.1142330E -03	0.9903891E -07

Regression coeff. for XNO

0.5038293E 03	-0.8612750E 01	0.5521111E -01	-0.1549630E -03	0.1600000E -06
-0.4948293E 03	0.8692751E 01	-0.5521111E -01	0.1549630E -03	-0.1600000E -06
-0.3855635E 03	0.6981533E 01	-0.5075555E -01	0.1730370E -03	-0.2133333E -06
-0.1098043E 05	0.1944262E 03	-0.1261666E 01	0.3578667E -02	-0.3733333E -05
0.1831502E 05	-0.3314302E 03	0.2203933E 01	-0.6355554E -02	0.6720000E -05

720-775 cm^{-1}

Regression coeff. for XO

0.5109281E 04	-0.1108857E 03	0.8444526E 00	-0.2695892E -02	0.3105130E -05
-0.8462297E 04	0.1376888E 03	-0.8304880E 00	0.2216207E -02	-0.2210524E -05
-0.8258344E 02	0.1139791E 01	-0.5475320E -02	0.1067979E -04	-0.6504266E -08
0.5441324E 02	-0.9953007E 00	0.6678551E -02	-0.1945505E -04	0.2082759E -07
-0.9373209E 01	0.1579922E 00	-0.9857006E -03	0.2703809E -05	-0.2747410E -08

Regression coeff. for XNO

0.5605168E 04	-0.9127724E 02	0.5509889E 00	-0.1461037E -02	0.1439999E -05
-0.3794536E 04	0.6118523E 02	-0.3624333E 00	0.9413331E -03	-0.9066667E -06
-0.5115043E 04	0.1014275E 03	-0.7277443E 00	0.2245630E -02	-0.2506667E -05
0.1469878E 05	-0.2498124E 03	0.1574677E 01	-0.4339851E -02	0.4426666E -05
0.1626541E 05	-0.2842654E 03	0.1832321E 01	-0.5133923E -02	0.5280000E -05

775-862 cm^{-1}

Regression coeff. for XO

-0.2092608E 03	0.3714197E 01	-0.2436700E -01	0.6995641E -04	-0.7399592E -07
-0.1379464E 03	0.2446343E 01	-0.1603974E -01	0.4605853E -04	-0.4882614E -07
-0.9351793E 01	0.1665130E 00	-0.1096972E -02	0.3167883E -05	-0.3381179E -08
-0.6127449E 00	0.1077600E -01	-0.6988550E -04	0.1977467E -06	-0.2053857E -09
-0.1045421E 00	0.1924329E -02	-0.1310525E -04	0.3904915E -07	-0.4279799E -10

Regression coeff. for XNO

0.2654070E 05	-0.4615200E 03	0.2969911E 01	-0.8378074E -02	0.8746667E -05
-0.1379625E 05	0.2398700E 03	-0.1540967E 01	0.4343998E -02	-0.4533333E -05
0.4033391E 05	-0.7075481E 03	0.4584844E 01	-0.1300741E -01	0.1365333E -04
-0.1928206E 05	0.3452952E 03	-0.2279900E 01	0.6608889E -02	-0.7093333E -05
-0.2695617E 05	0.4662571E 03	-0.2964989E 01	0.8245036E -02	-0.8479999E -05

APPENDIX C

Procedures Used in the Flux Calculation

In order to indicate what procedures were used to calculate the infrared fluxes, the equations for a three layer model are developed.

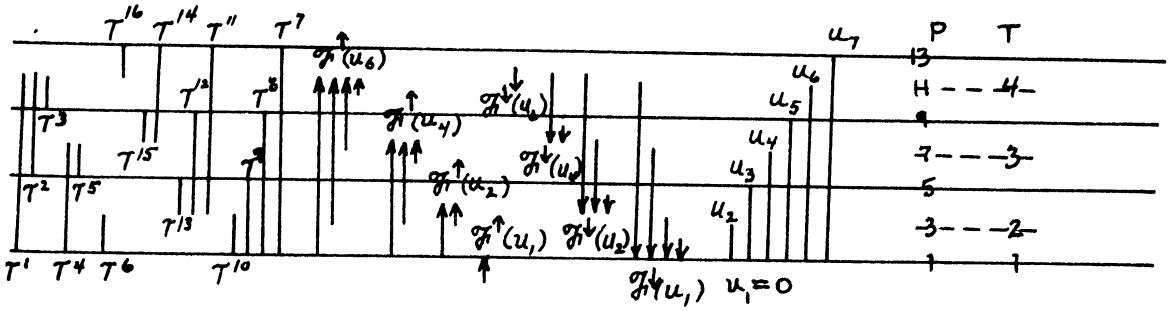

Figure (C-1) Flux calculation for a three layer atmosphere

The numbered lines on the left (τ^1 through τ^{16}) refer to the transmission functions $\tau_\delta(u_o, u)$ over the indicated mass paths. $\mathcal{F}^{\uparrow}(u_i)$ and $\mathcal{F}^{\downarrow}(u_i)$ are the total upward and downward fluxes, the arrows representing the individual contributions to the fluxes from the various atmospheric layers. u_i is the mass path indicating the level at which the flux is to be calculated. On the right the indexing schemes for the pressure (P), temperature (T), and mass path (u) are given.

The integrals in the flux equations (III-24) and (III-25) are evaluated as finite differences over half layers. The total upward flux for one subinterval of width δ at the middle of the top layer is,

$$\mathcal{F}^{\uparrow}(u_6) = \delta\pi\left\{B_{\omega_o}(0)\,\tau_\delta(u_6, u_1) + \int_{u_1}^{u_6} S_{\omega_o}(u)\,d\,\tau_\delta(u_6, u)\right\}$$

$$= \delta\pi\left\{B_{\omega_o}(T_1)\,\tau^1 + \int_{u_1}^{u_3} \quad + \int_{u_3}^{u_5} \quad + \int_{u_5}^{u_6}\right\}$$

$$\delta\pi\left\{B_{\omega_o}(T_1)\quad \tau^1 + S_{\omega_o}(T_2)\quad [\tau_\delta(u_6, u_3) \quad \tau_\delta(u_6 u_1)]\right.$$

$$+S_{\omega_o}(T_3)\left[\tau_\delta(u_6,u_5)-\tau_\delta(u_6,u_3)\right]+S_{\omega_o}(T_4)\left[\tau_\delta(u_6,u_6)-\tau_\delta(u_6,u_5)\right]\Big\}$$
$$=\delta\pi\Big\{B_{\omega_o}(T_1)\,\tau^1+S_{\omega_o}(T_2)\left[\tau^2-\tau^1\right]+S_{\omega_o}(T_3)\left[\tau^3-\tau^2\right]$$
$$+S_{\omega_o}(T_4)\left[1-\tau^3\right]\Big\}$$

(III-26) has been used to replace $\tau_{f\delta_i}$ with τ_{δ_i} in the flux equations. The equations for $\mathcal{F}^{\uparrow}(u_4)$ and $\mathcal{F}^{\uparrow}(u_2)$ are identical in form and

$$\mathcal{F}^{\uparrow}(u_1)=\delta\pi\,B_{\omega o}(T_1)\,\tau_\delta(u_1,u_1)$$

where,

$$\tau_\delta(u_1,u_1)=1$$

The downward fluxes follow similarly. For instance,

$$\mathcal{F}^{\downarrow}(u_4)=\delta\pi\int_{u_\infty=u_7}^{u_4}S_{\omega_o}(u)\,d\,\tau_\delta(u_4,u)$$
$$=\delta\pi\left\{\int_{u_7}^{u_5}S_{\omega_o}(u)\,d\,\tau_\delta(u_4,u)+\int_{u_5}^{u_4}S_{\omega_o}(u)\,d\,\tau_\delta(u_4,u)\right\}$$
$$=\delta\pi\Big\{S_{\omega_o}(T_4)\left[\tau_\delta(u_4,u_5)-\tau_\delta(u_4,u_7)\right]$$
$$+S_{\omega_o}(T_3)\left[\tau_\delta(u_4,u_4)-\tau_\delta(u_4,u_5)\right]\Big\}$$
$$=\delta\pi\left\{S_{\omega_o}(T_4)\left[\tau^{15}-\tau^{14}\right]+S_{\omega_o}(T_3)\left[1-\tau^{15}\right]\right\}$$

and

$$\mathcal{F}^{\downarrow}(u_6)=\delta\pi\int_{u_\infty=u_7}^{u_6}S_{\omega_o}(u)\,d\,\tau_\delta(u_o,u)$$
$$=\delta\pi\,S_{\omega_o}(T_4)\left[\tau_\delta(u_6,u_6)-\tau_\delta(u_6,u_7)\right]$$
$$=\delta\pi\,S_{\omega_o}(T_4)\left[1-\tau^{16}\right]$$

B_{ω_o} and S_{ω_o} are source functions and are evaluated as Planck functions at the indicated temperatures.

Rather than expressing the Planck function in terms of the mean wave number over the subinterval being considered, the following expression was used,

$$\frac{1}{\delta} \int_{\delta} S(\omega)\, d\omega$$

and evaluated using six point Gaussian quadrature.

APPENDIX D

Subintervals Used for the Individual Treatment of Water Vapor, Carbon Dioxide, and Ozone and for the Entire Infrared Spectrum. Subintervals are in Terms of Wave Number (cm^{-1})

Water Vapor	Carbon Dioxide	Ozone	Infrared
0-220			0-220
220-440			220-440
440-800			440-500
	500-555		500-555
	555-610		555-610
	610-667		610-667*
	668-723		668-723
	720-775		720-775
	775-862		775-800
800-1250			800-862
			862-971
		971-1109	971-1109
			1109-1250
1250-1420			1250-1420
1420-1590			1420-1590
1590-1845			1590-1845
1845-2100			1845-2100
2100-2450			2100-2450

*Q branch of carbon dioxide

APPENDIX E

Determination of the Number of Layers to be Used

Several factors must be considered in determining the number of layers to be used in calculating the cooling rate profiles. If too few are used, the calculated profiles will not accurately represent the true profiles. If too many are used the computer costs will become excessive. In addition, as more layers are intorudced, the data grid will become finer eventually requiring an accuracy in the data greater than that which is available.

Considering the truncation errors which were generated in his numerical solutions for an atmosphere which is divided into slabs approximately 33 mb thick, Katayama (1966) attained "sufficient accuracy" for the cooling rates when they were calculated at intervals of 100 mb. It would appear that "sufficient accuracy" represents a balance between computer costs and absolute accuracy but Katayama provides no explicit information as to what levels of accuracy were achieved.

Manabe and Möller (1961) and Manabe and Strickler (1964) used a somewhat different vertical coordinate system originally proposed by Smagorinsky to study the general circulation of the atmosphere. This system provides high resolution in the surface boundary layer and stratosphere where temperature varies rapidly with respect to pressure; the atmosphere was divided into nine layers or eighteen half layers.

To determine how many layers should be used in this model, cooling rates were calculated for the 6.3 micron band of water vapor from 1250 to 2100 cm^{-1}. London's (1957) atmospheric parameters for April at $35^{o}N$ from the surface to 12 km were considered and a cloudless atmosphere was assumed. To simplify the calculation somewhat, the median

line strengths per decade and the number of lines per decade were determined for a constant temperature of 300^{o}K. Also the Planck functions were evaluated at the centers of each subinterval rather than averaged.

Models of 8, 12, 16, 20, 24, and 32 layers were run having thicknesses of 100, 67, 50, 40, 33, and 25 mb per layer. Initially, unsmoothed temperature and water vapor data were used. The eight layer model produces a smooth profile but the values are physically unrealistic, showing a continuous decrease in the cooling rate from the surface to the tropopause. A more realistic profile should have a peak value well below the tropopause. The other profiles show rapid oscillations with height, the amplitudes of the oscillations increasing as the number of layers increases. This suggests that the oscillations are mathematically induced rather than real since the implicit and climatologically realistic smoothing produced by the coarse grid is lost as the vertical grid becomes finer and the errors inherent in the abstracting of the data and its necessarily discontinuous nature become evident.

The models were rerun with smoothed temperature distributions, the temperatures having been fitted to quadratic functions of pressure. Three profiles of 8, 12, and 16 layers are presented in Figure (E-1). Although the oscillations have not disappeared entirely, they are substantially reduced. The profiles also look somewhat more reasonable and show a degree of stability as the number of layers is increased, the differences between the 20 and 24 layer models being small. This suggests then that 20 and perhaps fewer layers will be sufficient for the calculations.

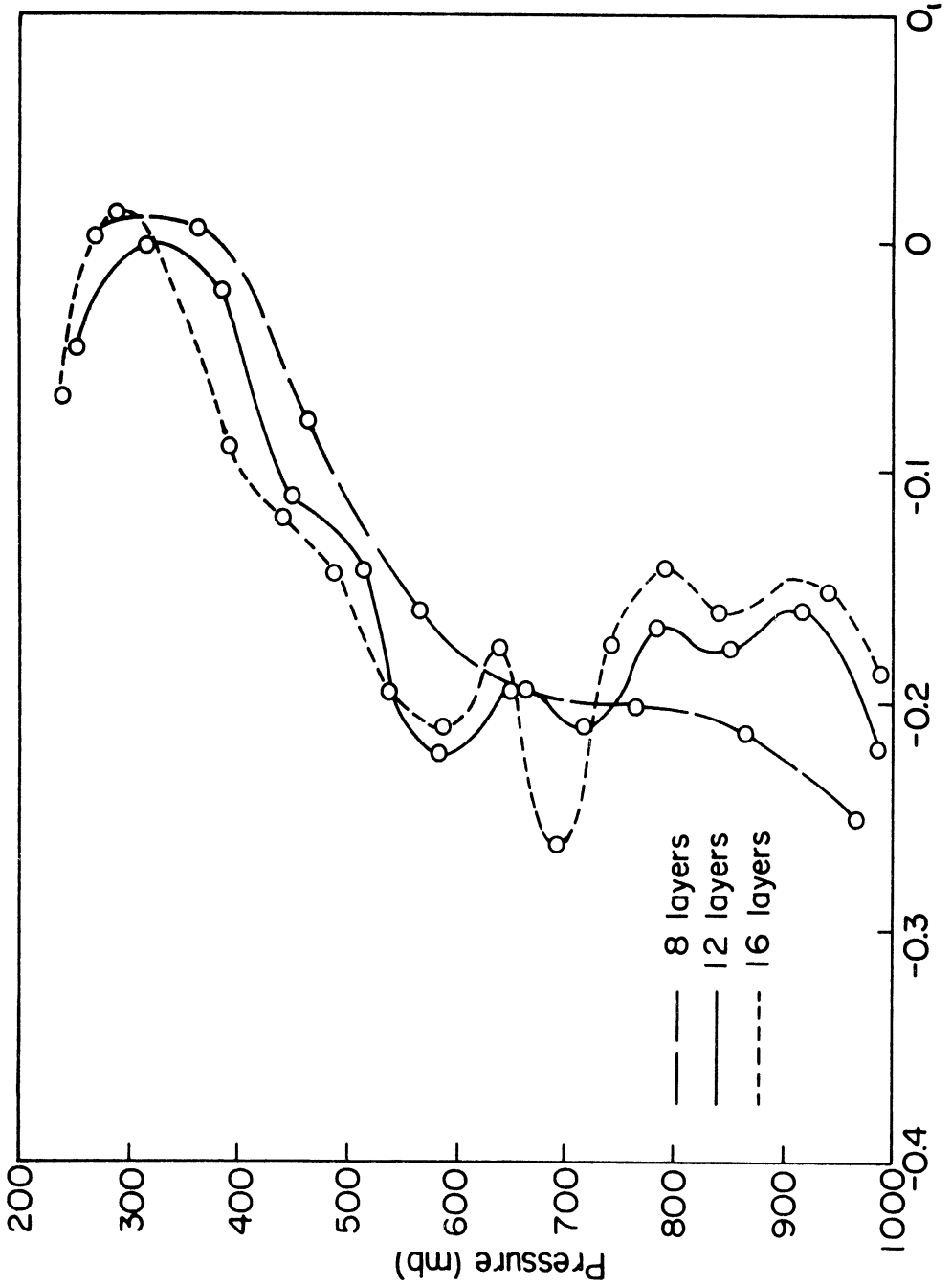

Figure E-1 Cooling rate profiles for the troposphere divided into 8, 12, and 16 layers using smoothed temperature distributions and fluxes determined at interfaces between layers

The increase of the cooling rate with height observed around 300 mb (9.25 km) is not a real characteristic of the cooling rate profile. Since the atmosphere is assumed to end at twelve km, the downward flux into the higher layers is underestimated. This produces the apparent increase of the cooling rate with height.

It is desirable to eliminate the oscillations in a more efficient way if possible. In the calculation scheme used to generate the profiles in Figure (E-1) the upward and downward fluxes are taken at the boundaries of the layer for which the cooling rate is being calculated, each atmospheric layer being represented by a single temperature equal to the temperature at the middle of that layer. Major contributions to these upward and downward fluxes come from the atmospheric layers immediately above and below the boundaries. The contributions from more distant layers are much smaller since they suffer considerably greater depletion. These upward and downward contributions to the fluxes at the interface of the two adjacent layers differ in magnitude because of the differences in the transmission properties of their respective mass paths and because of ; the differences in the temperatures of the two layers. However, since the temperature distribution is discontinuous and resembles something of a step function the inequality induced by the temperature difference will be exaggerated and produce profiles of the sort pictured in Figure (E-1).

If this unrealistic difference can be reduced the oscillations will be damped considerably. Ideally the fluxes should be functions of a continuous temperature profile, but such a representation would create mathematical problems. Instead the fluxes used to calculate the cooling rate, rather than being taken at the upper and lower boundaries of a layer, are taken at the midpoints of two adjacent layers. By doing this the

upward and downward flux contirubtions from the nearest atmospheric layers will differ only as a result of their differing transmission properties, their emitting temperatures now being equal. This technique is not in fact substantially different from that of the first approach used to eliminate the oscillations. It neither suggests a different cause for the oscillations nor a different solution. The temperature distribution is again being smoothed, in this instance however more directly with reference to the flux calculations.

The calculation scheme was adapted to this procedure for models of six, twelve, and eighteen layers. Each model was run using both unsmoothed and quadratically smoothed temperatures. No appreciable differences could be detected between the two types of profiles. Figure (E-2) presents the profiles for the unsmoothed cases. If the twelve layer profiles in Figures (E-1) and (E-2) are compared the oscillations are seen to be less pronounced when the fluxes are calculated at the midpoints of the layers. It can be concluded then that the discontinuous nature of the temperature distributions does contribute substantially to the oscillations.

Since the second approach eliminates the oscillations more efficiently, it has been used for the calculations of the cooling rate profiles. Referring to Figure (E-2) it appears that the profiles can best be represented by an atmosphere divided into layers approximately 65 mb thick. If thinner layers are used the oscillations become a problem while if thicker layers are used the calculated profiles do not adequately represent the true profiles. It also happens that such a layer size is convenient for the introduction of clouds.

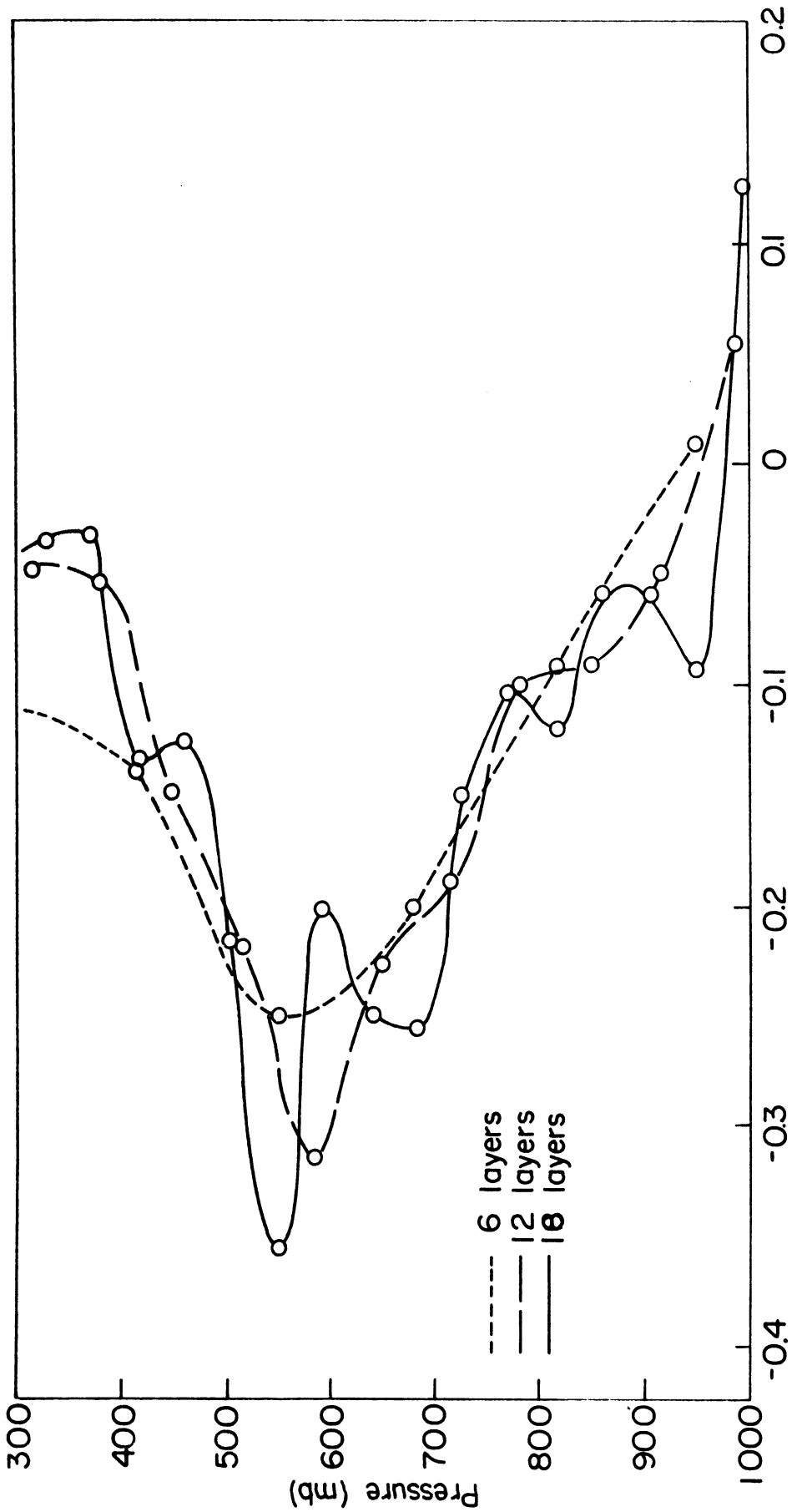

Figure E-2 Cooling rate profiles for the troposphere divided into 6, 12, and 18 layers with fluxes determined at centers of layers

Rodgers and Walshaw (1966) have investigated the cooling rate errors resulting from taking vertical steps of .1 and .2 scale heights. Assuming a homogeneous atmosphere of 8 km thickness these height increments are .8 and 1.6 km or approximately 85 and 170 mb near sea level and 55 and 110 mb at 5 km. They found that the .2 scale heights step produces errors of less than $0.03^{o}C\ day^{-1}$ and the .1 scale heights step, errors of less than $0.01^{o}C\ day^{-1}$. Thus using a vertical step of 65 mb should not produce errors in the cooling rates of more than a few hundredths of a degree per day.

APPENDIX F

Comparisons of the Annual Mean Zonally Averaged Infrared Fluxes (ly day^{-1}) at the Top of the Atmosphere

Latitude S	5^{o}	15^{o}	25^{o}	35^{o}	45^{o}	55^{o}	65^{o}	75^{o}	85^{o}
Sasamori et al. (top)	516	519	512	489	460	427	393	361	341
London (stratospheric contributions, Northern Hemisphere)	3.6	3.6	5.8	15.9	33.1	48.9	63.5	61.3	64.8
Present Study 137.5 mb	503	510	506	463	417	350	332	323	306
Present Study (stratosphere)	507	514	512	485	455	399	395	389	373
Katayama (net flux at 200 mb, Northern Hemisphere)	477	489	478	438	395	360	337	320	---
Vonder Haar and Suomi (1971)	530	550	530	460	415	380	335	295	---

BIBLIOGRAPHY

Allison, L. J., E. R. Kreins, F. A. Godshall, and G. Warnecke 1969: Monthly Global Circulation as Reflected in Tiros VII Radiometric Measurements, Part I: Example of the usefulness of satellite data in general circulation research. NASA Technical Note (in preparation), Goddard Space Flight Center.

Allison, L. J., and Warnecke, G., 1967: A Synoptic World Weather Analysis of TIROS VII Radiation Data. NASA TN D-3787.

Barnes, J. C., 1966: Note on the Use of Satellite Observations to Determine Average Cloudiness Over a Region. J. Geophys. Res., 71, 6137-6140.

Barnes, J. C., and Chang, D., 1968: Accurate Cloud Cover Determination and Its Effects on Albedo Computations. Goddard Space Flight Center, Final Report NAS 5-10478.

Benedict, W. S., and Calfee, R. F., 1967: Line Parameters for the 1.9 and 6.3 Micron Water Vapor Bands. ESSA Professional Paper 2.

Bristor, C. L., W. M. Callicott, and R. E. Bradford, 1966: Operational Processing of Satellite Cloud Pictures by Computer. Mon. Wea. Rev., 94, 515-527.

Brooks, C. E. P., 1927: The Mean Cloudiness Over the Earth. Memoirs Roy. Meteor. Soc., 1, 127-138.

Brunt, D., 1939: Physical and Dynamical Meteorology. London, Cambridge University Press.

Burch, D. E., D. A. Gryvnak, and D. Williams, 1962: Infrared Absorption by Carbon Dioxide, Water Vapor, and Minor Atmospheric Constituents. Ohio State University, Research Report, Contract AF19(604)-2633.

Calfee, R. F., and Gates, D. M., 1966: Calculated Slant-Path Absorption and Distribution of Atmospheric Water Vapor. Appl. Optics, 5 287-292.

Changnon, S. A., Jr., and Huff, F. A., 1957: Cloud Distribution and Correlation with Precipitation in Illinois. State Water Survey Div., State of Illinois, Report of Investigation 33.

Clapp, P. F., 1964: Global Cloud Cover for Seasons Using TIROS Nephanalyses. Mon. Wea. Rev., 92, 495-507.

Clapp, P. F., 1968: Northern Hemisphere Cloud Cover for Selected Late Fall Seasons Using TIROS Nephanalyses. ESSA Technical Memo. WBTM NMC 44.

Clodman, J., 1957: Some Statistical Aspects of Cirrus Cloud. Mon. Wea. Rev., 85, 37-41.

Curtis, A. R., 1952: Discussion of a Paper by Goody. Quart. J. Roy. Meteor. Soc., 78, 638-640.

Davis, P. A., 1961: A Re-examination of the Heat Budget of the Troposphere and Lower Stratosphere. Scientific Report No. 3, Contract No. AF19(604)-6146, Research Div., College of Engr., New York University.

Davis, A., 1963: An Analysis of the Atmospheric Heat Budget. J. Atmos. Sci., 20, 5-22.

de Bary, E., and F. Moller, 1963: The Vertical Distribution of Clouds. J. Appl. Meteor. 2, 806-808.

Dopplick, T. G., 1970: Global Radiative Heating of the Earth's Atmosphere, Report No. 24, Dept. of Meteorology, Massachusetts Institute of Technology, Cambridge, Mass.

Drayson, S. R., 1970: Private communication, University of Michigan, Ann Arbor.

Elliott, F. E., 1960: Mean Monthly Cloud Cover Over the U. S. S. R., Technical Information Series, No. R60ELC31, Advanced Electronics Center, Cornell University.

Elsasser, W. M., 1942: Heat Transfer by Infrared Radiation in the Atmosphere. Harvard Meteor. Studies, No. 6, Harvard University Press, Cambridge.

Elsasser, W. M., 1960: Atmospheric Radiation Tables. Meteor. Monographs, 4, No. 23.

Fritz, S., and Rao, P. K., 1967: On the Infrared Transmission Through Cirrus Clouds and the Estimation of Relative Humidity from Satellites. J. Appl. Meteor., 6, 1088-1096.

Fritz, F., and Winston, J. S., 19 2: Synoptic Use of Radiation Measurement from Satellite Tiros II. Mon. Wea. Rev., 90, 1-9.

Glaser, A. H., James C. Barnes, and Donald W. Beran, 1968: Apollo Landmark Sighting: An Application of Computer Simulation to a Problem in Applied Meteorology. J. Appl. Meteor., 7, 768-779.

Godshall, F. A., 1968: Intertropical Convergence Zone and Mean Cloud Amount in the Tropical Pacific Ocean. Mon. Wea. Rev., 96, 172-175.

Godshall, F. A., et al., 1969: An Atlas of Average Cloud Cover Over the Tropical Pacific Ocean, Part II. Examples of the usefulness of satellite data in general circulation research. NASA Technical Note (in preparation), Goddard Space Flight Center, Greenbelt, Md.

Godson, W. L., 1955: The Computation of Infrared Transmission by Atmospheric Water Vapor. J. Meteor. 12, 272-284.

Goody, R. M., 1952: A Statistical Model for Water Vapor Absorption. Quart. J. Roy. Meteor. Soc., 78, 165-169.

Goody, R. M., 1964: Atmospheric Radiation. Oxford University Press, Cambridge, Mass., 436 pp.

Greaves, J. R., David D. Spiegler, and James H. Willand, 1971: Development of a Global Cloud Model for Simulating Earth-Viewing Space Missions. Final Report, Contract No. NAS 8-25812, Allied Research Assoc., Inc.

Hann, J., 1906: Lehrbuch der Meteorologie. Leipzig, Chr. Herm. Tauchnitz.

Haurwitz, B., and J. M. Austin, 1944: Climatology, New York, Mc-Graw Hill, 410 pp.

Harvard, J. B., 1960: On the Radiational Characteristics of Water Clouds at Infrared Wave Lengths, Ph. D. Thesis, University of Washington, Seattle.

Hitschfeld, W., and Houghton, J. T., 1961: Radiative Transfer in the Lower Stratosphere Due to 9.6 Micron Band of Ozone. Quart. J. Roy. Meteor. Soc., 87, 562-576.

Ishimaru, Y., 1952: Nephology (Kumo No Kishogaku). Hokuryu-Kan (in Japanese).

James, D. G., 1959: Observations from Aircraft of Temperatures and Humidities Near Stratocumulus Clouds. Quart. J. Roy. Meteor. Soc., 85, 120-130.

Katayama, A., 1966: On the Radiation Budget of the Troposphere over the Northern Hemisphere (I). J. Meteor. Soc. Japan, 44, 381-401.

Katayama, A., 1967a: On the Radiation Budget of the Troposphere over the Northern Hemisphere (II). J. Meteor. Soc. Japan, 45, 1-25.

Katayama, A., 1967(b): On the Radiation Budget of the Troposphere over the Northern Hemisphere (III). J. Meteor. Soc. Japan, 45, 26-38.

Kornfield, J., and Hasler, A. F., 1970: A Photographic Summary of the Earth's Cloud Cover for the Year 1967. J. Appl. Meteor., 8, 687-700.

Kourganoff, V., 1962: Basic Methods in Transfer Problems. New York, Dover Publishing Co., 281 pp.

Kuhn, P. M. and Weickmann, H. K., 1969: High Altitude Radiometric Measurements of Cirrus. J. Appl. Meteor., 8, 147-154.

Kuhn, W. R., 1966: Infrared Radiative Transfer in the upper Stratosphere and Mesosphere. Scientific report prepared for National Science Foundation, Atmospheric Science Section under Grant NSF GP-3196.

Landsberg, H., 1945: Handbook of Meteorology, ed. by F. A. Berry, Jr., E. Bollay, and N. R. Beers. New York, McGraw-Hill Book Co., Inc., 927-998.

London, J., 1957: A Study of the Atmospheric Heat Balance. Final report, Contract AF19(122)-165, Research Div., College of Engr., New York University.

Lorenz, E. N., 1967: The Nature and Theory of the General Circulation of the Atmosphere. World Meteorological Organization.

McCabe, J. T., 1965: Estimating Mean Cloud and Climatological Probability of Cloud-Free Line-of-Sight. Technical Report 186, Environmental Technical Application Center, U. S. Air Force.

McDonald, J. E., 1960: Absorption of Atmospheric Radiation by Water Films and Water Clouds. J. Meteor., 17, 232-238.

McDonald, W. F., 1938: Atlas of Climatic Charts of the Oceans. Washington, D.C., U. S. Government Printing Office, WB No. 1247.

Malkmus, W., 1967: Random Lorentz Band Model with Exponential-Tailed S^{-1} Line Intensity Distribution Function. J. Optical Soc. Am., 57, 323-329.

Manabe, S., and Moller, F. 1961: On the Radiative Equilibrium and Heat Balance of the Atmosphere. Mon. Wea. Rev., 89, 503-532.

Manabe, S., and Strickler, R., 1964: Thermal Equilibrium of the Atmosphere with a Convective Adjustment. J. Atmos. Sci., 21, 361-385.

Mastenbrook, H. J., 1968: Water Vapor Distribution in the Stratosphere and High Troposphere. J. Atmos. Sci., 25, 299-311.

Newell, R. E., and Doppleck, T. G., 1970: The Effect of Changing CO_2 Concentration on Radiative Heating Rates. J. Appl. Meteor., 9, 958-959.

Palmer, C. H., Jr., 1960: Experimental Transmission Functions for the Pure Rotation Band of Water Vapor. J. Optical Soc. Am., 50, 1232-1242.

Plass, G. N., 1956a: The Influence of the 9.6 Micron Ozone Band on the Atmospheric Infra-Red Cooling Rate. Quart. J. Roy. Meteor. Soc., 82, 30-44.

Plass, G. N., 1958: Models for Spectral Band Absorption. J. Optical Soc. Am., 48, 609-703.

Portman, D. J., and Ryznar, E., 1971: An Investigation of Heat Exchange. International Indian Ocean Expedition, Meteorological Monograph, No. 5, East West Press, Honolulu, 78 pp.

Ramage, C. S., et al., 1969: Atlas of the International Indian Ocean Expedition. Honolulu, East-West Center Press.

Rao, P. K., and Winston, J. S., 1963: An Investigation of Some Synoptic Capabilities of Atmospheric "Window" Measurements from Satellite TIROS II. J. Appl. Meteor., 2, 12-23.

Raschke, E., 1968: The Radiation Balance of the Earth-Atmosphere System from Radiation Measurements of the Nimbus II Meteorological Satellite. NASA TN D-4589.

Rasool, S. I., and Prabhakara, C., 1966: Heat Budget of the Southern Hemisphere: Problems in Atmospheric Circulation. Washington, D. C., Spartan Books, 76-92.

Rodgers, C. D., 1968: Some Extensions and Applications of the Random Model for Molecular Band Transmission. Quart. J. Roy. Meteor. Soc., 94, 99-102.

Rodgers, C. D., and Walshaw, C. D., 1966: The Computation of Infra-Red Cooling Rate in Planetary Atmospheres. Quart. J. Roy. Meteor. Soc., 92, 67-92.

Sadler, J. C., 1968: Average Cloudiness in the Tropics from Satellite Observations. Honolulu, East-West Center Press.

Sadler, J. C., 1969: Private communication.

Salomonson, V. V., 1969: Cloud Statistics in Earth Resources Technology Satellite (ERTS) Mission Planning. Preprint X-622-69-386, Goddard Space Flight Center.

Sasamori, T., 1968: The Radiation Cooling Calculation for Application to General Circulation Experiments. J. Appl. Meteor., 7, 721-729.

Sasamori, T., Julius London, and Douglas V. Hoyt, 1971: Radiation Budget of the Southern Hemisphere. National Center for Atmospheric Research, Ms. No. 71-100, Boulder, Colorado.

Schloss, M., 1962: Cloud Cover of the Soviet Union. Geographical Rev., 52, 389-399.

Seide, R. N., 1954: The Distribution of Cloudiness by Type and Height in the Northern Hemisphere for the Spring and Fall, M.S. Thesis. New York University.

Sellers, W. D., 1958: The Annual and Diurnal Variations of Cloud Amounts and Cloud Types at Six Arizona Cities. Scientific Report No. 8, Institute of Atmospheric Physics, University of Arizona.

Sellers, W. D., 1966: Physical Climatology. Chicago, University of Chicago Press.

Shaw, N., 1936: Manual of Meteorology, v. 2, Comparative Meteorology. London, Cambridge University Press.

Sherr, P., A. H. Glaser, J. C. Barnes, and J. H. Willand, 1968: World-Wide Cloud Cover Distributions for Use in Computer Simulations. Final Report, Contract NAS 8-21040, Allied Research Associates, Inc.

Stull, V. R., P. J. Wyatt, and G. N. Plass, 1963: The Infrared Absorption of Carbon Dioxide, Infrared transmission studies, Final Report SSD-TDR-62-127, Vol. III, Aeronutronic Div., Ford Motor Company.

Taljaard, J. J., H. Van Loon, H. L. Crutcher, and R. L. Jenne, 1969: Climate of the Upper Air, Part I, Southern Hemisphere, 1: Temperatures, Dew Points, and Heights at Selected Pressure Levels. NAVAIR 50-1C-55, Washington, D. C.

Telegadas, K., and London, J., 1954: A Physical Model of the Northern Hemisphere Troposphere for Winter and Summer. Scientific Report No. 1, Contract AF19(122)-165, Research Div., College of Engr., New York University.

Tetens, O., 1930: Uber einige Meteorologische Begriffe. Z. Geophys., 6, 297-309.

Tverskoi, P. N., 1965: Physics of the Atmosphere (Translated from Russion by A. Sen and R. N. Sen, Israel Program for Scientific Translations). Available from National Technical Information Service, U. S. Department of Commerce, Springfield, Virginia, 22151.

Van Loon, H., 1971: Cloudiness and Precipitation. Meteorology of the Southern Hemisphere, AMS Monograph, Chap. 6.

Vonder Haar, T. H. and Suomi, V. E., 1971: Measurements of the Earth's Radiation Budget from Satellites During a Five-Year Period, Part I: Extended Time and Space Means., J. Atmos. Sci., 28, 305-314.

Walshaw, C. D., 1957: Integrated Absorbtion by the 9.6μ Band of Ozone. Quart. J. Roy. Meteor. Soc., 83, 315-321.

Walshaw, C. D., 1966: Remarks on the Computation of Radiative Heating Rates. Publications de C. N. E. S. Presses, Universitaires de France, Paris.

Walshaw, D. D., and Rodgers, C. D., 1963: The Effect of the Curtis-Godson Approximation on the Accuracy of Radiative Heating Rate Calculations. Quart. J. Roy. Meteor. Soc., 89, 122-130.

Widger, W. K., Jr., J. C. Barnes, E. S. Merritt, and R. B. Smith, 1966: Meteorological Interpretation of Nimbus High Resolution Infrared (HRIR) Data. NASA Contractor Report CR-352.

Williamson, E. J., and Houghton, 1965: Radiometric Measurements of Emission from Stratospheric Water Vapour. Quart. J. Roy. Meteor. Soc., 91, 330-338.

Winston, J. S., 1966: Global Distribution of Cloudiness and Radiation for Seasons as Measured from Weather Satellites. Climate of the Free Atmosphere of the World, Survey of Climatology, Vol. 3, Chap. 7, Amsterdam, Elsevier Publishing Company.

Wyatt, P. J., V. Robert Stull, and Gilbert N. Plass, 1962a: Quasi-Random Model of Band Absrotpion. J. Optical Soc. Am., 52, 1209-1217.

Wyatt, P. J., V. R. Stull, and G. N. Plass, 1962b: The Infrared Absorption of Water Vapor. Infrared transmission studies, Final Report SSD-TDR-62-127, Vol. II, Aeronautronic Div., Ford Motor Company.

Yamamoto, G., 1952: On a Radiation Chart. Scientific Report, Tohoku University, Ser. 5, Geophysics, 4, 9-23.